ECN
Energy research Centre of the Netherlands

Aero-elastic simulation of offshore wind turbines in the frequency domain

TURBU@Sea

F.J. Savenije
J.M. Peeringa

ECN-E–09-060

Abstract

The design and analysis of offshore wind turbines is a difficult task compared to onshore, due to the numerous load cases that have to be considered and the calculation work involved. Not only the amount of sea states to deal with at a specific site, but also the differences between sites and even between locations within a wind park should be taken into account for offshore wind energy. To ease this process, the use of the linearized frequency domain tool ECN TURBU, which is very fast compared to the commonly used nonlinear time domain tools, is investigated.

TURBU is a fast fully integrated wind turbine design and analysis tool, which deals with aerodynamics, hydrodynamics, structural dynamics and control of modern three bladed wind turbines. The linearized wind turbine model is derived from geometric and material properties and site conditions. The system is then transformed to the frequency domain, useful for load calculation, stability analysis and control design. The wind, gravity, wave and water current loading are applied as input spectra to the wind turbine model. The results from load calculations can be analyzed both in the frequency domain (output spectra) and the time domain (simulations).

Although frequency domain methods are common practice in offshore industry, the use of a fully integrated wind turbine design and analysis tool in the frequency domain is new to the wind energy sector. It requires a different design approach than conventional time domain tools, but creates opportunities as well due to quick feedback on the results during the design process.

In this report it is shown how TURBU can aid the design of (offshore) wind turbines. A footprint of the wind turbine visualizing the effect of important design choices is constructed from output load spectra obtained with TURBU. Optimization using parameter variation can assist the designer in finding optimal settings for critical design parameters. Also the analysis of an offshore wind turbine with TURBU is addressed. It is used to identify the sea states contributing to fatigue, which reduces the number of sea states to analyse with nonlinear time domain tools. The results are compared to those obtained with a nonlinear time domain analysis tool (ECN PHATAS). Special attention is paid to the influence of the (linearized) hydrodynamics and the calculation method on the results.

Acknowledgement

The work in this project was carried out within the Dutch offshore wind programme "We@Sea". The We@Sea/Bsik foundation is acknowledged for the financial support of the We@Sea-project 2004-025 "Aero-elastic simulation of offshore wind turbines in the frequency domain". The ECN project number is 7.9426.

Contents

Notations

V_{wind},V_w	wind speed	$[m/s]$
ϕ_{wind}	wind direction	$[deg]$
H_m	mean wave height	$[m]$
T_m	mean wave period	$[s]$
H_s	significant wave height	$[m]$
T_p	spectral wave peak period	$[s]$
γ_{js}	JONSWAP wave peak shape factor	$[-]$
V_{wave}	wave speed	$[m/s]$
ϕ_{wave}	wave direction	$[deg]$
$\phi_{w\&w}$	angle between wind and wave direction	$[deg]$
k_{wave}	wave number	$[-]$
λ_{wave}	wave length	$[m]$
d_{water}	water depth	$[m]$
C_m	mass coefficient	$[-]$
C_D	drag coefficient	$[-]$
R_i	load of the i^{th} bin of the fatigue load spectrum	
n_i	number of cycles in the i^{th} bin	
R_{eq}	equivalent fatigue load	
n_{eq}	number of equivalent cycles	
m	SN curve slope for the relevant material	
K	SN curve constant for the relevant material	
S_i	stress level of the i^{th} bin of the fatigue load spectrum	
D_i	damage in the i^{th} bin of the fatigue load spectrum	
F	force	$[N]$
M	moment	$[Nm]$
x	displacement	$[m]$
ϕ	rotation	$[rad]$
k	stiffness	$[N/m]$
d	damping	$[Ns/m]$
m	mass	$[kg]$
δ	deformation	$[m]$,$[rad]$
Ω_r	rotor speed	$[rad/s]$
P_r	rotor power	$[W]$
θ	blade pitch angle	$[deg]$
d_{hub}	hub height	$[m]$
d_r	rotor diameter	$[m]$
ϕ_{yaw}	yaw angle	$[deg]$
η	efficiency	$[-]$
H	frequency transfer function	
f	frequency	$[Hz]$
ω	frequency	$[rad/s]$
ω_n	eigenfrequency	$[rad/s]$
ζ	damping ratio	$[-]$
d_{cr}	critical damping	$[Ns/m]$
δ_{LD}	logarithmic damping decrement	$[\%]$

$\bullet_r$	rotor
$\bullet_g$	generator
$\bullet_s$	support structure
$\bullet_P$	from PHATAS
$\bullet_T$	from TURBU
$\bullet_{fa}$	fore aft (x)
$\bullet_{sts}$	side to side (y)
DOF	degree of freedom
wkp	working point
BEM	blade element momentum
MSL	mean sea level
eq1Hz	load at 1Hz cycles equivalent to real load
SUT	system under test
FFT	fast fourier transform
DFT	discrete fourier transform
CFD	computational fluid dynamics
RFC	rainflow count
D6MW	6MW Dowec (Dutch offshore wind energy converter)
CDT	Control Design Tool
SWIFT	Simulation of WInd Fields in Time
ROWS	Random Ocean Wave Simulator

1 Introduction

1.1 Wind energy

Energy is a very important resource in today's modern world. As the security of supply and the pollution of fossil fuels are under debate, the use of renewable wind energy is a clean and relatively cheap (in euro/kWh) solution. Most state of the art wind turbines extract power from wind by converting the air flow through a three bladed rotor to mechanical energy, which is converted into electric power by a generator. This complex structure involves aerodynamics, structural dynamics and control. Modelling of a wind turbine is essential, both for design and certification. Even during its operation a detailed up-to-date model can be useful for condition monitoring and control.

Although the models of wind turbines have greatly improved the last decades, there are still a lot of challenges in this field. With increased detail, the models have grown in size, which can result in slow computation. As wind energy is moving offshore, hydrodynamics and support structures come into play.

We@Sea program
The current target of 30% reduction of green house gases (mainly CO_2) in 2020 as stated by the Dutch government in the program 'Schoon en zuinig'. Furthermore, 20% of the energy consumption should be from renewable sources. With only a few hundred MW wind energy installed offshore at present, there is still a long way to go.

One of the initiatives to reach this target is the We@Sea R&D program (see Westra and Beurskens (2009)), started in 2004 and partly funded by the Dutch government. It focuses on offshore wind energy in the Netherlands, gathering knowledge to enable the large scale implementation of wind energy in the North Sea. This research project TURBU@Sea is performed within the framework of the We@Sea program.

1.2 Linearized frequency domain tool TURBU

Due to the complexity and nonlinearity of a wind turbine, most wind turbine design and analysis tools use nonlinear time domain models. Some examples are Garrad Hassans BLADED, Risoe-DTU HAWC, FLEX and ECN PHATAS. The downside of this approach is mainly the long computation time involved. A typical 10min simulation also takes 10 minutes computation time on a modern computer.

Both in the design process and for the preliminary analysis (load set calculation) of offshore wind turbines a short computation time is required. This led to the development of the linearized frequency domain tool TURBU.

ECN TURBU is a fast fully integrated wind turbine design and analysis tool, which deals with aerodynamics, hydrodynamics, structural dynamics and control of modern three bladed wind turbines. The linearized wind turbine model is derived from geometric and material properties and site conditions. The system is then transformed to the frequency domain, useful for load calculation, stability analysis and control design. The wind, gravity, wave and water current loading are applied as input spectra to the wind turbine model. The results from load calculations can be analyzed both in the frequency domain (output spectra) and the time domain (simulations).

1.3 TURBU@Sea

1.3.1 Background

modelling/design offshore wind turbine support structure

Several studies have reported on modelling offshore wind turbine support structures and hydrodynamic loading. The approach of van der Tempel (2006) and Kuhn (2001) is to separate wind turbine and support structure, but model the interaction between the two with a frequency transfer function (mainly fore aft aerodynamic damping). This method is adopted from the offshore industry, where it is successfully used for design. Wind turbines however, differ quite a bit from offshore structures: wind and wave loading, rotational excitation and low support structure eigenfrequency for instance.

The proposed method is a practical approach, as the wind turbine and support structure are usually still separately developed nowadays. It does however not offer the benefit of an integral design of support structure and wind turbine.

hydrodynamic loading

In the OWTES project, Henderson (2003) et al. conducted an extensive study on the hydrodynamic loading of offshore wind turbines. Most important conclusion is that only CFD will give accurate results for shallow water. Modelling results were compared to measurements on the Blyth wind farm and even the best available wave model (stream function) underestimates both fatigue as well as extreme loads, mainly due to structural dynamic response.

In Henderson and Zaaijer (2008), the importance of using an integral approach to assess hydrodynamic loading on offshore wind turbines is acknowledged. Especially for slender support structures, the dynamics of the structure should be taken into account. In shallow water, the effect of the nonlinear waves become more pronounced, but for deeper seas, the stochastic linear wave model is a good compromise approach.

optimization

Ever since the development of wind turbine design codes, effort has been put in finding the optimal wind turbine design (for a given site and specification). The common route has been to simplify the models for optimization, as for instance in Zaaijer (2001). Lack of computer power (and increasing detail in the models) has been the main driver for this strategy.

fatigue

Fatigue, the damage that occurs under cyclic loading (see chapter 4), is one of the design criteria for wind turbines. Fatigue can be calculated from time series (as currently implemented in both PHATAS and TURBU), but also directly from the frequency domain. This method, developed by Dirlik et al. (see Sherratt et al. (2005)), has speed as its main advantage. As TURBU works in the frequency domain, it could be an interesting approach to use. In Ragan and Manuel (2007) however, both methods are compared and time domain calculation seems to be the best solution for wind turbine fatigue analysis. This is mainly due to the periodic components in the load. Fortunately, TURBU also allows for very fast time domain load calculations that are obtained with the transformed frequency domain model.

Sutherland (2000) gives an extensive overview on the fatigue properties of wind turbines, pointing at several component and material issues. The properties of glass fiber composite, which is a commonly used wind turbine blade material, differ from other materials due to its non homogeneous character. The fatigue properties of glass fiber composite, as discussed in Mandell et al. (1992) and Kensche (2004), are used in the chapter 4 on fatigue.

load case reduction

In Kuhn (2001), so called 'lumped' load cases are derived from the three dimensional sea state scatter diagram to reduce the amount of computational work. The lumping is done with wind speed as main parameter (steps of 1m/s). The sea states (wave height and period) in these bins are then lumped by weighing their quasi-static damage. A refinement step is suggested, after the first calculation of lumped load cases. This approach shows good results compared to the full analysis (error within a few percent). However, the danger of missing critical cases remains, where the quasi-static solution is not representative. Directional effects are also not considered.

1.3.2 Project goal

The goal of this project is to investigate the use of TURBU for integrated design and analysis and consists of four parts.

Requirement for application of TURBU is that it produces accurate and reliable results. Because the model (linear), excitation (frequency spectra) and solution methods (state space and Laplace domain) are of completely different nature than used in time domain codes, this is not trivial. The first step therefore is a thorough comparison of TURBU results to results from the validated nonlinear time domain tool PHATAS.

The Morison equation describes the hydrodynamic force on the submerged structure. For use in TURBU, this relation must be linearized. Although for slender support structures the inertia term dominates the nonlinear water drag, the latter can still have impact, especially when water current is present, for ultimate load cases or with high frontal area (lattice) supports. A literature survey on this topic shows different paths that can be followed.

Essential in the design phase is a characterization of the wind turbine dynamics and loading. What are the support structure eigenfrequencies? Are they excited by the rotor speed or blade passing frequency and how do they change with tower height, foundation stiffness or water depth? What happens when the coupled edgewise and torsion blade modes are excited? These kind of problems can be identified from the proposed characterization method. A second topic of integral design methods is optimization of the integral wind turbine design, which comes within reach with the fast TURBU code. The linear frequency domain approach of TURBU means short computation time, but without simplifying model structure. However, TURBU has other downsides due to linearization around the working point equilibrium, as described in section 2.3.

A large number of load cases have to be evaluated during design and certification of a wind turbine. Offshore, wave and water current loading require an even bigger set of load cases. Reduction of load cases for offshore wind turbine (fatigue) analysis by a preselection of critical cases with TURBU will decrease the calculation time considerably.

The following boundaries and assumptions were used throughout the project:

1 focus on fatigue loads
  Fatigue is one of the design drivers for wind turbines, due to the very high number of load cycles during its lifetime: up to a factor thousand higher compared to airplanes of the same size. Ultimate loads (an extreme wind gust or emergency shutdown for instance) are also of great importance, but they often have a nonlinear behaviour and occur across a wide operation range. Such conditions can (currently) not be described with TURBU, although some progress is made into that direction.

2 simulations on the 6MW Dowec wind turbine at the IJmuiden offshore site
  The Dutch offshore wind energy converter (Dowec) design and the measurement data of the

sea states at IJmuiden during the last twenty year are publicly available. The 6MW Dowec design (see chapter 2) is representative for large offshore wind turbines that are currently being developed. On the other hand, the results cannot be compared to measurements as the 6MW Dowec turbine has never been built.

3 only production cases (no idling, emergency shutdown etc.)
Most of the fatigue occurs during normal production, which should account for more than 90% of the life time of a wind turbine. Some remarks on this assumption in chapter 5.

4 water current loading is not taken into account
Water current loading is not considered, mostly because water current is not modelled in PHATAS/ROWS. Moreover, water current is not measured at the IJmuiden offshore site. It is however shown to be of importance in Peters and Boonstra (1988), and an improved strategy for linearization of the hydrodynamics with water current in TURBU has been developed (see appendix A).

1.4 Report overview

This report consists of three chapters. The first chapter starts with a brief description of the Dowec 6MW wind turbine, the object of this study. Then the modelling in PHATAS (nonlinear time domain) and TURBU (linear frequency domain) is addressed. The last part of this chapter compares the results obtained with the PHATAS and TURBU models. The second chapter presents several integral design and analysis methods, that came available with the development of TURBU. For instance, a characterization of the wind turbine at a specific offshore site is derived with TURBU. The last chapter deals with offshore wind turbine fatigue. After some background on fatigue and the used calculation method, the influence of wave loading on fatigue is analysed. A load case reduction strategy is proposed using TURBU to determine the critical cases for fatigue.

2 Modelling the Dowec 6MW

In this chapter the modelling of the Dowec 6MW (D6MW) in PHATAS and TURBU is compared. First the D6MW design (see webdatabase Dowec (2003)) is briefly addressed, as this wind turbine is the main object of this study. In the following two sections the modelling of this turbine in both PHATAS and TURBU is discussed. The last section presents the results on comparing both models in time and frequency domain.

2.1 Dowec 6MW predesign

The Dutch offshore wind energy converter project was initiated by six main players in the Dutch wind energy and offshore field and ran from 2000 to 2003. It's main objective was to explore the possibilities for designing a large offshore wind turbine. The project has been funded by NOVEM and the Economy, Ecology and Technology programme of the Dutch Ministry of Economic Affairs to boost the Dutch wind energy sector and take a step toward the Kyoto and European Climate Change Protocols. As discussed in 1.1, there is still a lot of work to do in this field. In the Dowec project, both a 6MW wind turbine and a 3MW variant were designed. Only the last one made it into a (2.75MW) prototype. An complete overview of the Dowec project can be found at Dowec (2003).

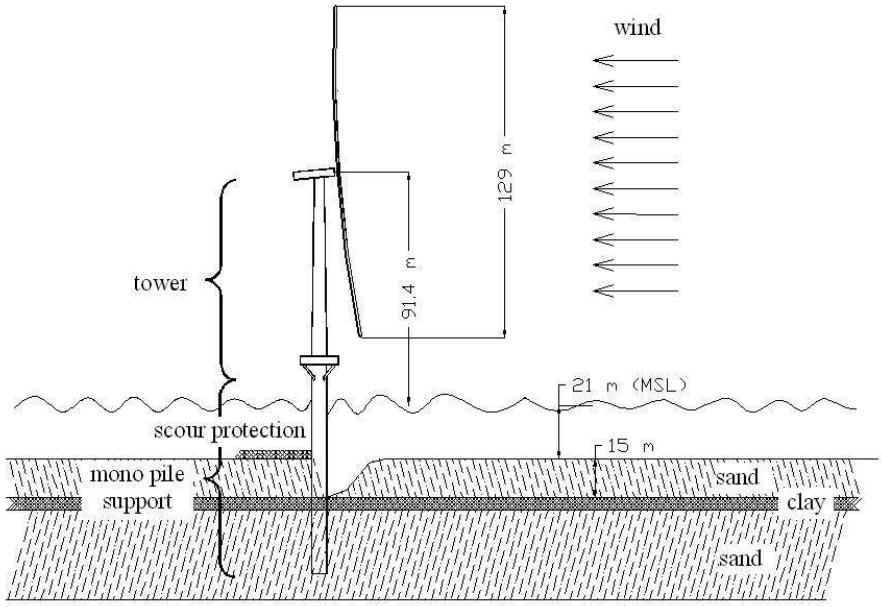

Figure 1: Overview of the D6MW wind turbine

An overview of the D6MW is shown in figure 1. The following list summarizes the D6MW predesign as used in this study.

- pitch regulated, variable speed turbine
- rated power of 6MW, rated speed of 11.84rpm
- rotor diameter 129m, at 91.4m hub height
- LM64.5 blade, high torsion stiffness variant
- monopile support structure (6m diameter), tubular tower

Figure 2 shows the power curve and the pitch action of the D6MW predesign. Figure 3 shows its generator curve. An extensive analysis of the LM 64.5 blade design and model can be found in Lindenburg (2002).

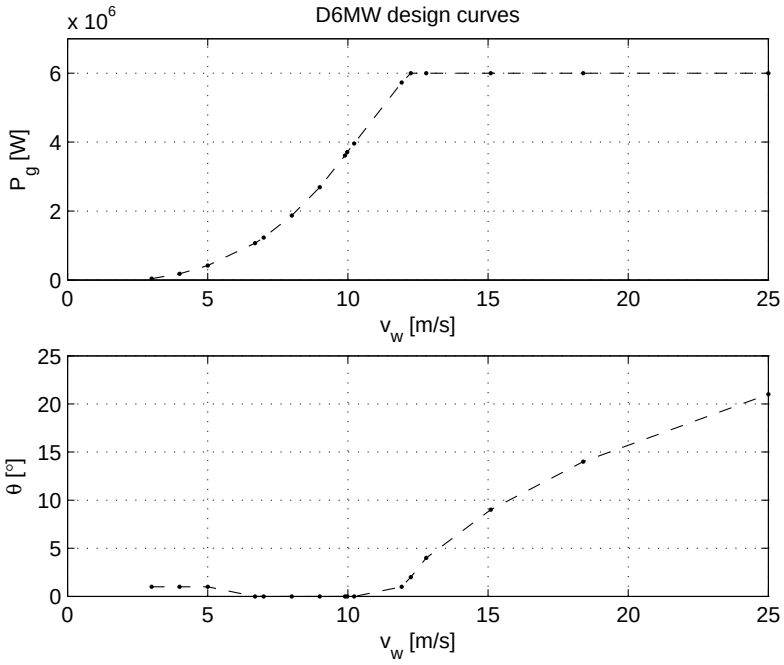

Figure 2: Power and pitch angle curves of the D6MW wind turbine

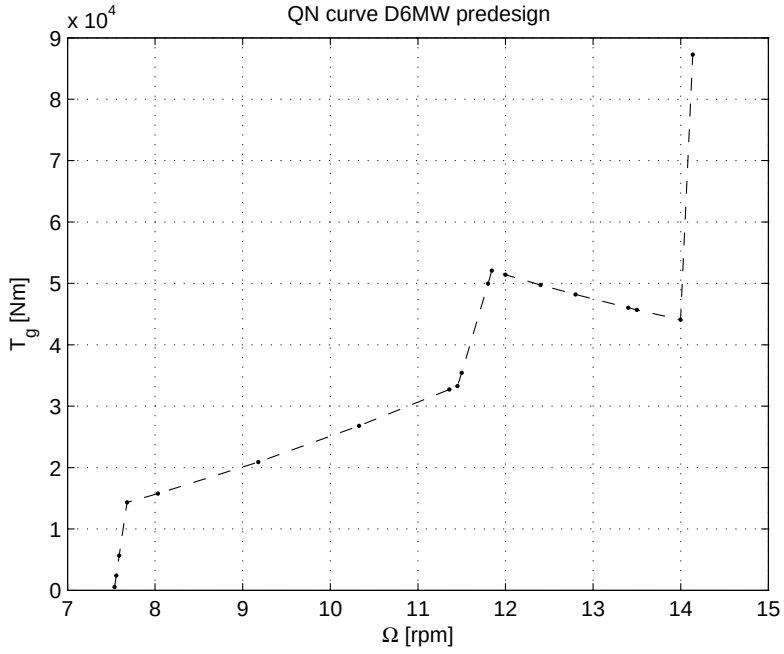

Figure 3: Generator curve of the D6MW wind turbine

2.2 PHATAS model D6MW

This section is a brief summary of the D6MW modelling in PHATAS. For more information on the PHATAS modelling approach, see Lindenburg (2005). A detailed description of this PHATAS model can be found in Kooijman et al. (2003).

PHATAS is a nonlinear time domain wind turbine analysis tool, both used for design/evaluation and certification purposes. The result of the simulations are time series of the wind turbine model (mainly loads and deformations). The strength of PHATAS is nonlinear interaction of the structural model with the aerodynamics, hydrodynamics and control. The most important model properties/assumptions are summarized in the following list.

- nonlinear beam approach for blade deformation, all axis defined on blade chord
- linearized support structure, Craig-Bampton model reduction
- drive train model consists of gear ratio, shaft torsion and flexible mounting
- different power loss models (proportional loss, loss curve)
- nonlinear feedback control (from CDT, see Wouters and van Engelen (2008))
- full 3D turbulent wind field (from SWIFT, see Winkelaar (1992))
- linear stochastic waves (from ROWS, see Eecen (2003))

See table 2 for a comparison of the model definition in PHATAS and TURBU.

2.3 TURBU model D6MW

In this section the modelling of the D6MW wind turbine with the ECN code TURBU is described. The first part gives an overview of the modelling approach in TURBU. Then the model choices for the D6MW specific are presented.

2.3.1 Linear frequency domain tool TURBU

TURBU derives a detailed linearized model, using aerodynamic, geometric and material properties. The following list summarizes the properties/assumptions of a TURBU wind turbine model.

- modular modelling approach
- equilibrium in working point solved with full nonlinear model
- linearized time invariant model defined in working point
- multibody approach for flexible components
- modal reduction for blades and support structure
- drive train model by 3DOF shaft torsion & bending, rigid gears, flexible gearbox support and variable speed generator
- pitch actuator model
- linearized control
- linear stochastic wind (Kaimal spectrum)

- linear stochastic waves (Pierson-Moskovitz or JONSWAP spectrum)

modelling approach and setup
This paragraph provides a short description of the TURBU modelling approach. More detailed information can be found in van Engelen (2007) and van Engelen and Braam (2004).

The models from TURBU have a modular set up, defining the wind turbine as an assembly of substructures or components. This allows for changing or in(ex)cluding certain systems (for example a specific pitch drive) and adding control loops. Input and output selection minimizes the required data processing.

structural
For structural modelling of the wind turbine (blades, drive train and support structure), a multibody approach is followed. The input properties at each cross section like specific mass, Young's modulus and second moment of inertia, are used to derive a beam model (connected simple beam elements). This is transformed to a multibody mass, spring, damper system for blades, tower and main shaft. The model order increases with number of elements in each flexible part. The resulting model can be reduced in order with the method developed by Hurty and Craig-Bampton. This approach works for both the tower and the blades of the wind turbine. The nacelle and gearbox are represented by rigid bodies connected with spring damper combinations. The foundation is modelled as a stiffness matrix for all directions, including coupling terms (see 2.4.1).

aerodynamic
The aerodynamics in TURBU are based on the following:
- BEM theory
- Prantl correction for wake influence
- dynamic inflow wake effect
- turbulent wake state
- dynamic stall unsteady aerodynamic effect

The wind field in TURBU is based on Kaimal's wind spectrum and derived from helices in the downwind moving turbulence frame that coincides with the elements of the rotating blades. This method is very computationally efficient.

hydrodynamic
The hydrodynamic modelling is based on linear Airy wave theory and the JONSWAP wave spectrum to derive water particle velocity and acceleration, and Morison's equation (3) to obtain the force on the underwater structure. Water current is also accounted for. The hydrodynamic loads are calculated for each support structure element, as they depend on the water motion (waves and current) and the motion of the structure itself. The equation shows nonlinear relation between force and speed, which is linearized as in the below listed equation (5) according to Borgman (1967a). More on the linearization of the hydrodynamic damping can be found in appendix A.

The JONSWAP (JOint North Sea WAve Project) spectrum (figure 18) used to calculate water surface elevation in TURBU is a modified Pierson-Moskowitz spectrum, with the main difference being the shape of the peak. It requires three parameters: the significant wave height H_s, the wave peak period T_p and the peak shape factor γ_{js}.

The wave speed fading with water depth is obtained by solving the dispersion relation for intermediate water depth (1) according to Airy. Figure 4 shows this is a good trade off for wave periods between one and ten seconds and a water depth of 21 meter. The dispersion relation is solved for the wave length λ_{wave} at each frequency in the spectrum with the wavenumber defined as $k_{wave} = \frac{2\pi}{\lambda_{wave}}$. With this wave number the horizontal wave velocity (figure 5) as function of

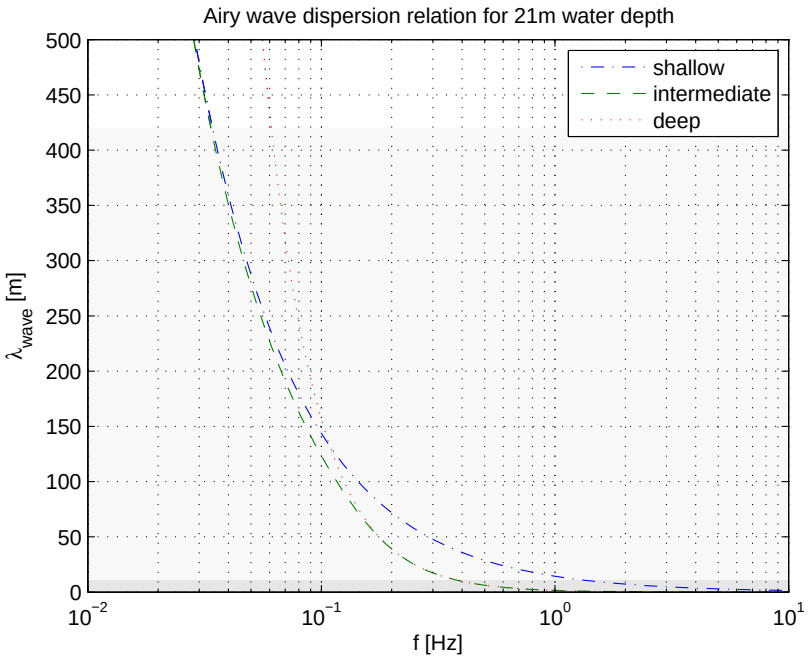

Figure 4: Airy dispersion relation

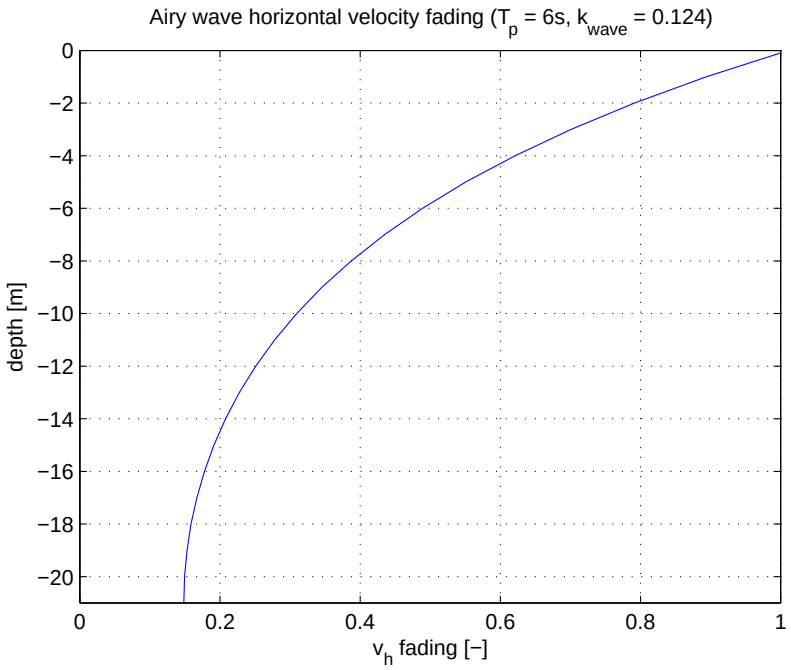

Figure 5: Horizontal wave speed fading according to Airy

water depth is then found with equation 2.

$$\omega_{wave}(k_{wave}) = \sqrt{k_{wave} \cdot g \cdot \tanh(k_{wave} \cdot d_{water})} \tag{1}$$

$$\dot{x}_{wave}(z) = A \cdot \frac{\cosh(k_{wave} \cdot (z + d_{water}))}{\sinh(k_{wave} \cdot d_{water})} \tag{2}$$

Morison's equation finally describes the relation between water motion and the force on the structure, taking into account the drag force (first term) and inertia effects (second and third terms). The force depends both on the water motion u and the structural motion x. The coefficient of added mass is related to the coefficient of mass C_m as $C_{am} = C_m - 1$.

$$F_{hydro} = \frac{1}{2}\rho C_D D \left|\dot{u} - \dot{x}\right| (\dot{u} - \dot{x}) + \rho C_m \frac{\pi}{4} D^2 \ddot{u} - \rho C_{am} \frac{\pi}{4} D^2 \ddot{x} \tag{3}$$

In this project the following implementation of the linearized Morison equation in TURBU was used, as described by van Engelen and Braam (2004). Under the assumption that the relative velocity r is small compared to the current velocity U the squared velocity in the drag term of the Morison equation can be written as

$$(U + r)|U + r| = r|r| + 2Ur \tag{4}$$

Inserting the Borgman linearization, $\sqrt{\frac{8}{\pi}}\sigma$, in $r|r|$ gives the following expression for the linearized Morison equation:

$$F_{linhydro} = \frac{1}{2}\rho C_D D \left(\sqrt{\frac{8}{\pi}}\sigma_{\dot{u}} + 2 \cdot U\right)(\dot{u} - \dot{x}) + \frac{\pi}{4}\rho C_m D^2 \ddot{u} - \frac{\pi}{4}\rho C_{am} D^2 \ddot{x} \tag{5}$$

control
To obtain a stable system, the wind turbine needs to be controlled. Therefore, a linearized controller is connected to the model in feedback. This linearized controller is derived with TURBU built-in functions (for a specific working point) from the Dowec controller that was designed with the Control Design Tool.

linearization
To obtain a linear time invariant model three steps are performed. First the equilibrium for a working point defined by V_{wind}, θ and Ω is calculated with the nonlinear model. Then the component models are linearized in this working point in their local coordinate systems. Finally the component models are connected and the rotating coordinates (in blades and drive train parts) are transformed to global fixed-frame coordinates. The transformation matrix (6) represents the multi-blade transformation as proposed by Coleman and Feingold (1958) for three corresponding signals on the three rotor blades from the fixed frame to the rotating frame.

$$\begin{vmatrix} x_{rf} \\ y_{rf} \\ z_{rf} \end{vmatrix} = T_{cm} \cdot \begin{vmatrix} x_{ff} \\ y_{ff} \\ z_{ff} \end{vmatrix} \text{ with } T_{cm} = \begin{bmatrix} 1 & \sin(\Omega t) & \cos(\Omega t) \\ 1 & \sin(\Omega t + \frac{2\pi}{3}) & \cos(\Omega t + \frac{2\pi}{3}) \\ 1 & \sin(\Omega t + \frac{4\pi}{3}) & \cos(\Omega t + \frac{4\pi}{3}) \end{bmatrix} \tag{6}$$

2.3.2 D6MW in TURBU

For the D6MW, most parts of the model are taken from the PHATAS input. Some of the input specifications had to be transformed as described in 2.4.1.

See table 2 for a comparison of the D6MW model definition in PHATAS and TURBU.

2.4 Comparison of the TURBU and PHATAS models

In this section the wind turbine model and simulation results obtained with TURBU are compared to PHATAS. The following aspects are considered, which altogether give a complete view on the differences between the codes:

2.4.1 model definition
2.4.2 working point conditions of equilibrium
2.4.3 modal analysis
2.4.4 power spectra of load signals
2.4.5 fatigue

environmental and operating conditions

1 working point equilibrium and modal analysis (wind only)
The working point and equilibrium conditions of the two models are compared for the whole operating range.

2 spectra and fatigue (wind and wave loading)
The fatigue comparison of the PHATAS and TURBU model is done with a predefined set of operating conditions (wind speed, wind direction, significant wave height, wave peak period and wave direction) shown in table 1. The set is based on equally spaced wind speeds, with some extra points just below rated (high loading). The sea states in this set are the most frequently occurring conditions for the selected wind speeds. For this first analysis, the wind and wave direction are both set to zero. This also implies aligned wind and waves (zero angle between the wind and waves $\phi_{w\&w}$), which is in agreement with the most occurring situation.

Table 1: Operating conditions for comparison

case	V_{wind} [m/s]	ϕ_{wind} [deg]	H_s [m]	T_p [s]	ϕ_{wave} [deg]
1	5.0	0.0	0.75	4.82	0.0
2	8.0	0.0	0.75	4.82	0.0
3	10.0	0.0	1.25	5.47	0.0
4	12.0	0.0	1.25	5.47	0.0
5	15.0	0.0	2.25	6.75	0.0
6	20.0	0.0	2.75	7.39	0.0
7	25.0	0.0	4.25	8.68	0.0

From this selection, a reference set (only wind loading) and a test set (wind and wave loading) are defined.

2.4.1 Model definition

Table 2 shows the differences in input specification for the PHATAS and the TURBU model.

blade geometry definition
The TURBU blade definition is more detailed than in PHATAS, mostly concerning the location of the blade axes. For this reason, BLADMODE input files are used for the TURBU blade model. The BLADMODE input is defined in the blade coordinate system (no twist and with respect to the blade axis), while TURBU mostly uses the element coordinate system. Thus the BLADMODE input data is transformed over the twist and to the elastic axis (see appendix B).

blade torsion stiffness
During preliminary analysis on the PHATAS D6MW model, some problems were encountered when including the blade torsion DOF in the model. The controller was not able to react properly

Table 2: TURBU and PHATAS input definition.

item	PHATAS value	unit	TURBU value	unit
structural: rotor properties				
blade model	nonlinear beam		linear MB	
number of blade elements	17	[-]	17	[-]
number of blade modes			6	[-]
blade structural damping	0.0048	[-]	700 4700 450[a]	[1/s]
blade mass	17.4e3	[kg]	17.3e3	[kg]
hub mass	30e3	[kg]	30e3	[kg]
hub height	91.4	[m]	91.4	[m]
upwind rotor center	5.0	[m]	5.0	[m]
structural: nacelle and drive train properties				
nacelle mass	188e3	[kg]	188e3	[kg]
nacelle center of gravity	357e3	[kgm]	1.9	[m]
shaft stiffness	3.29e8	[Nm/rad]	3.29e8	[Nm/rad]
gear ratio	92.873	[-]	92.873	[-]
loss model	prop. to torque	[Nm]	η in wkp	[-]
yaw system	inactive		no	
structural: support structure properties				
tower model	linear beam		linear MB	
number of tower elements	55		15	
number of tower modes	4		8	
tower mass	514e3	[kg]	524e3	[kg]
tower structural damping	0.0016	[-]	478 478 2670[b]	[1/s]
foundation model	coupled springs		stiffness matrix	
aerodynamic				
wind field	3D cylinder (SWIFT) 3D turbulence		3D helices longitudinal turbulence	
wind spectrum	Kaimal		Kaimal	
wind shear	power law		power law	
shear constant	0.2	[-]	0.2	[-]
tower shadow	yes, 3 directions		yes, longitudinal	
turbulence intensity I_{15}	16	[%]	16	[%]
hydrodynamic				
wave spectrum	JONSWAP		JONSWAP	
wave peak factor γ	3.3	[-]	3.3	[-]
load method	Morison		Morison	
control				
strategy	nonlinear feedback real time		linear feedback in wkp offline	
gain scheduling	yes		in wkp	
peak shaving	yes		in wkp	

[a] in lead, torsion and flap direction
[b] in side to side, fore aft and torsion direction

on the torsional vibration, but seemed to even excite this resonance. Figure 6 shows the oscillation in the blade root torsion moment and the torsion deformation. Using higher torsion stiffness variant of the LM 64.5 blade (which was already defined in the Dowec project) solved the issue. Figure 7 shows the torsion stiffness of both the blade variants.

foundation stiffness and water depth

PHATAS models the foundation with flexibility terms for translation, torsion and bending. For bending also coupling with translation is taken into account following the definition in (7). In TURBU, two methods can be selected for modelling of the foundation. The first is an extension of the tower below the earth's surface with length Z_e. The second method is similar to PHATAS,

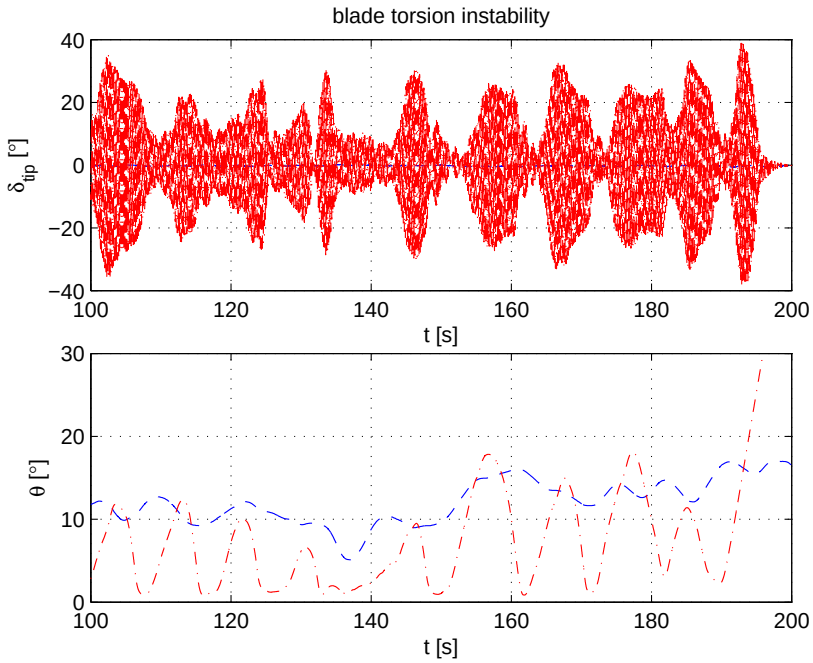

Figure 6: Blade root torsion moment and the torsion deformation at the blade tip for both the low (r-.) and the higher stiffness (b–) blade variants.

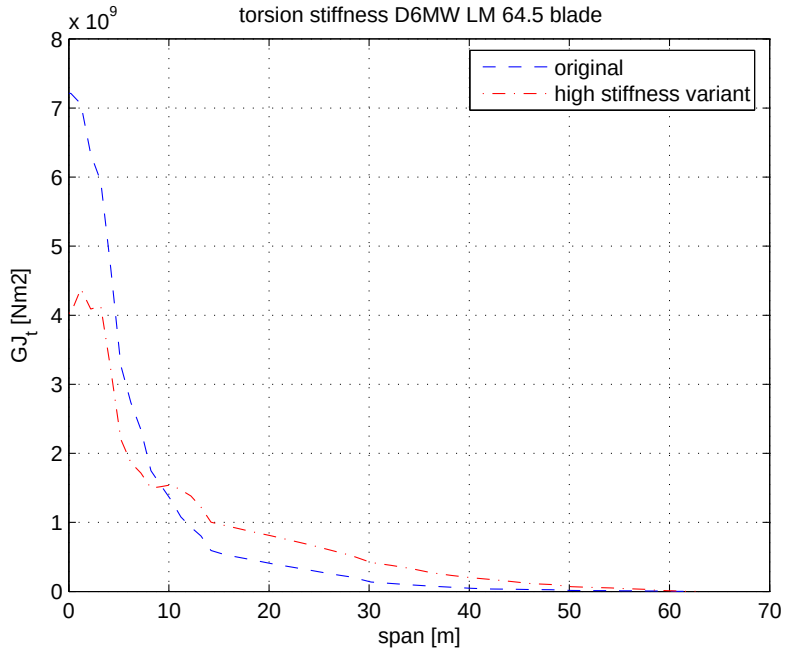

Figure 7: Torsion stiffness of the LM 64.5 blade

but requires coupling stiffness terms instead of coupling compliance terms as input (8).

$$\mathbf{P}: \begin{bmatrix} \phi \\ u \end{bmatrix} = \begin{bmatrix} \frac{1}{k_\phi} & \frac{f}{k_\phi} \\ \frac{f}{k_\phi} & \frac{1}{k_u} \end{bmatrix} \cdot \begin{bmatrix} M \\ F \end{bmatrix} \tag{7}$$

$$\mathbf{T}: \begin{bmatrix} S_{\phi\phi} & S_{\phi u} \\ S_{u\phi} & S_{uu} \end{bmatrix} \cdot \begin{bmatrix} \phi \\ u \end{bmatrix} = \begin{bmatrix} M \\ F \end{bmatrix} \tag{8}$$

Table 3 is taken from the report Kooijman et al. (2003) and shows the foundation models of the D6MW wind turbine for different water depth, which were derived by soil simulation software of Ballast Nedam Rehal (2003). The parameters are calculated with the assumption of zero shear force, but this is not the case. Although for a multi MW wind turbine the shear force on the foundation is small compared to the bending moment (+/-1% for a 100m tower), in the test setup the shear force does have a considerable contribution to the loading at the tower base. The coupling term in the foundation compliance would add an extra rotation of $\frac{14}{30} \approx 50\%$ if the shear force is included.

An alternative model used in the Dowec project is a variation of the original based on eigenfrequency analysis of the support structure. This only includes bending stiffness (no coupling), which is specified with ratio 1.13 to the original value. Table 4 shows the foundation parameters for the design water depth of 21m and the variation of depth. This alternative model neither has transverse and torsion degrees of freedom in PHATAS (k_u & k_γ) and TURBU (S_{uu} & $S_{\gamma\gamma}$).

Figure 8 shows the spectra of the tower base moments with the different foundation models at a wind speed of 15m/s. The foundation model has big impact on the dynamics, because the tower rigid body mode (top mass on rigid pile with flexible foundation at 0.5Hz) interferes with the flexible tower modes. For the first tower bending mode at 0.3Hz, the system can be simplified as an equivalent mass linked to a combination of springs in series, with the equivalent spring constant $k_{eq} = (k_1 \cdot k_2)/(k_1 + k_2)$. The estimated eigenfrequency of the combined rigid and first flexible mode is 0.24Hz, which agrees with the frequency from PHATAS and TURBU. Both the first and the second flexible tower modes are effected by this mechanism (seen in figure 8 as reduction in eigenfrequency).

With the implementation of coupling between bending and translation in PHATAS, the modes seem to interact even more (sharp peak at 1.1Hz). In TURBU, this is not observed. In fact, there is no difference at all between TURBU foundation with and without coupling, because the coupling is not active in TURBU. This is caused by the different modelling approach. In TURBU, a stiffness matrix is used and the coupling term is only active with a linear DOF. This is not required in PHATAS, which models the foundation as elasticity.

As the assumption on the calculation of the coupling is questionable and a fundamental modelling difference causes different results, the alternative model without coupling will be used. For this model, TURBU compares quite good to PHATAS (as will be discussed in section 2.4.4).

Table 3: Foundation stiffness of D6MW model

d_{water} [m]	k_u [N/m]	k_ϕ [Nm/rad]	k_γ [N/m]	f_{coup} [m]
21	inf	3.282e10	inf	14.58
26	inf	3.509e10	inf	14.13
31	inf	3.799e10	inf	12.76
36	inf	4.424e10	inf	10.41

Table 4: Adjusted foundation stiffness of D6MW model

	PHATAS		TURBU	
d_{water} [m]	k_ϕ [Nm/rad]	f_{coup} [m]	S_ϕ [Nm/rad]	$S_{u\phi}$ [N/m]
21	3.705e10	0.0	3.705e10	0
26	3.961e10	0.0	3.961e10	0
31	4.289e10	0.0	4.289e10	0
36	4.994e10	0.0	4.994e10	0

structural damping

From Newton's second law $F = m \cdot a$, the equation of motion (x) for a free unloaded mass-

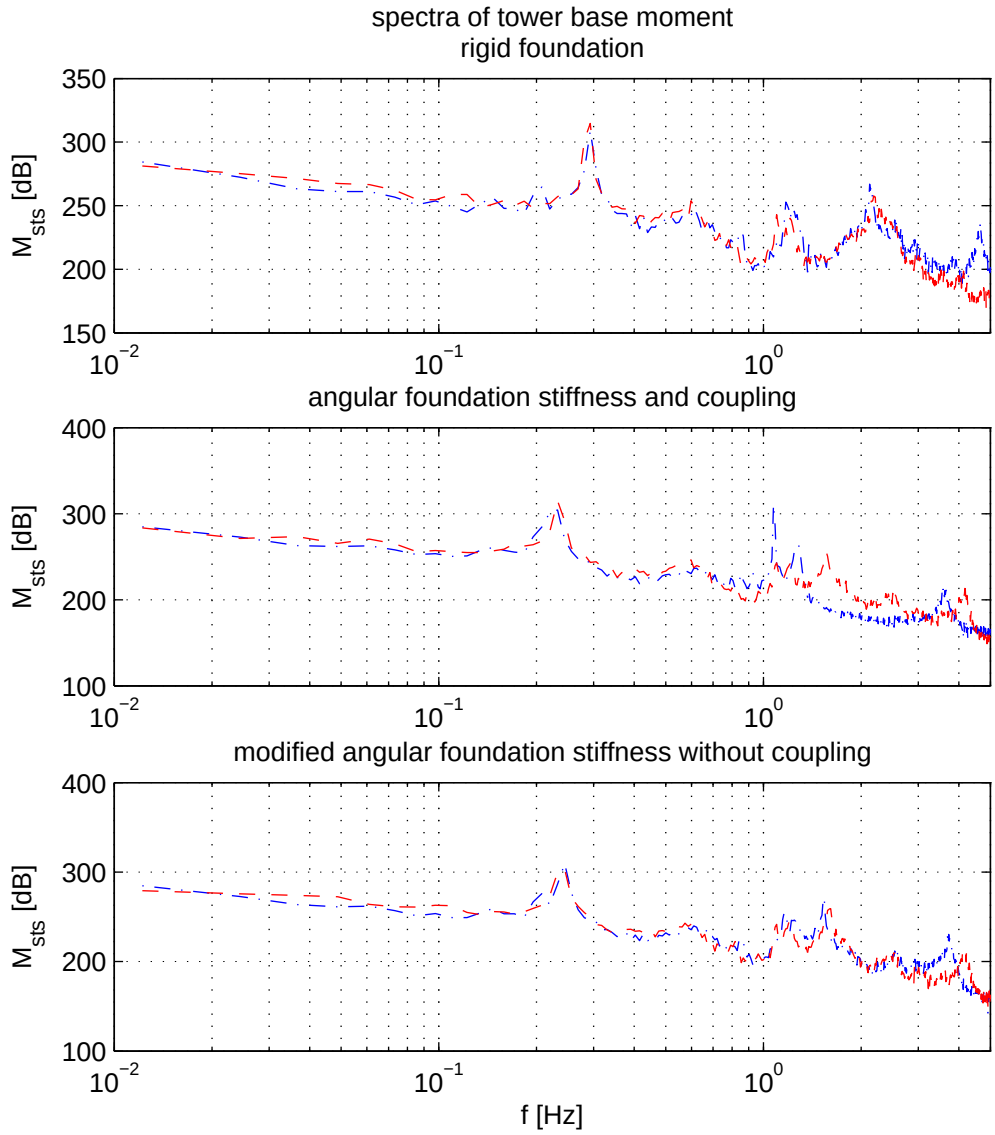

Figure 8: Spectra (vw=15m/s) of the side to side tower base moment calculated with PHATAS (bx) and TURBU (ro) for different foundation models.

spring-damper ($m-k-d$) system becomes:

$$m \cdot \ddot{x} + d \cdot \dot{x} + k \cdot x = 0 \tag{9}$$

This can also be written as:

$$\ddot{x} + 2\zeta\omega_n \cdot \dot{x} + \omega_n^2 \cdot x = 0 \tag{10}$$

with the natural frequency $\omega_n = \sqrt{\frac{k}{m}}$, the damping ratio $\zeta = \frac{d}{d_{cr}}$ and the critical damping $d_{cr} = 2\sqrt{k \cdot m}$.

The structural damping of a system is usually defined as the percentage decrease of two peaks of an oscillation (after release from a none zero displacement) and this value is called the logarithmic damping decrement δ. The D6MW specifies 3% damping for the blades, and 1% for the support structure. The relation between damping ratio ζ and the logarithmic damping decrement δ_{LD} is

for small damping values defined as in equation 11.

$$\zeta = \frac{\delta_{LD}}{\sqrt{4\pi^2 + \delta_{LD}^2}} \approx \frac{\delta_{LD}}{2\pi} \tag{11}$$

The structural damping in PHATAS is specified as a fraction of the critical damping for the first mode (12), while in TURBU a ratio between stiffness and damping is defined (13).

$$\mathbf{P} : \zeta_P = \frac{d}{d_{cr}} \tag{12}$$

$$\mathbf{T} : dr_T = \frac{k}{d} \tag{13}$$

These two definitions combined, give us the relation between PHATAS and TURBU input:

$$dr_T = \frac{\omega_n}{2\zeta_P} \tag{14}$$

Table 5 shows the damping ratio's for both models. From the FFT comparison shown in 2.4.4, the damping (peak shape) of the first modes of the blade and tower matches good.

Table 5: Structural damping of D6MW model

dir	description	f [Hz]	ζ_P [-]	dr_T [1/s]
1	B_{flap}	0.69	4.77e-3	4.54e2
2	B_{lead}	1.07	4.77e-3	7.04e2
3	B_{tors}	7.16	4.77e-3	4.71e3
1	T_{fa}	0.225	1.59e-3	4.44e2
2	T_{sts}	0.225	1.59e-3	4.44e2
3	T_{tors}	1.35	1.59e-3	2.67e3

drive train losses
In Kooijman et al. (2003), the PHATAS proportional power loss model (15) is derived from the specified power loss curve of the D6MW machine.

$$\mathbf{P} : P_{loss} = c_p \cdot P_a + c_c \cdot \Omega \tag{15}$$

$$\mathbf{T} : \eta = P_e / P_a \tag{16}$$

In TURBU, the losses are defined as overall efficiency η in each working point (16). To make an accurate comparison possible, a table is constructed for the overall efficiency that matches the PHATAS power loss model. Figure 9 shows the original efficiency factor and both the PHATAS and TURBU approximation. Figure 10 shows the resulting power losses for the three cases.

2.4.2 Working point conditions of equilibrium

The working point of a wind turbine is defined by wind speed V_w, blade pitch angle θ and rotor speed Ω. Figure 11 shows these operating conditions and the resulting produced power.

The blade root moments (figure 12), blade deformations at the tip (figure 13), tower base moments (figure 14) and resulting displacement at the tower top (figure 15) are important properties to look at when comparing the equilibrium state of a wind turbine.

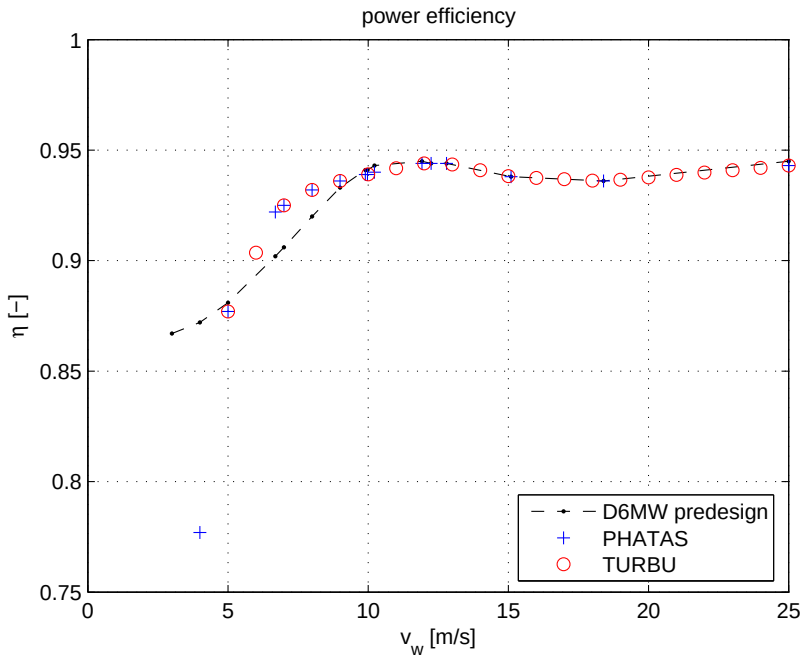

Figure 9: Overall drive train efficiency η

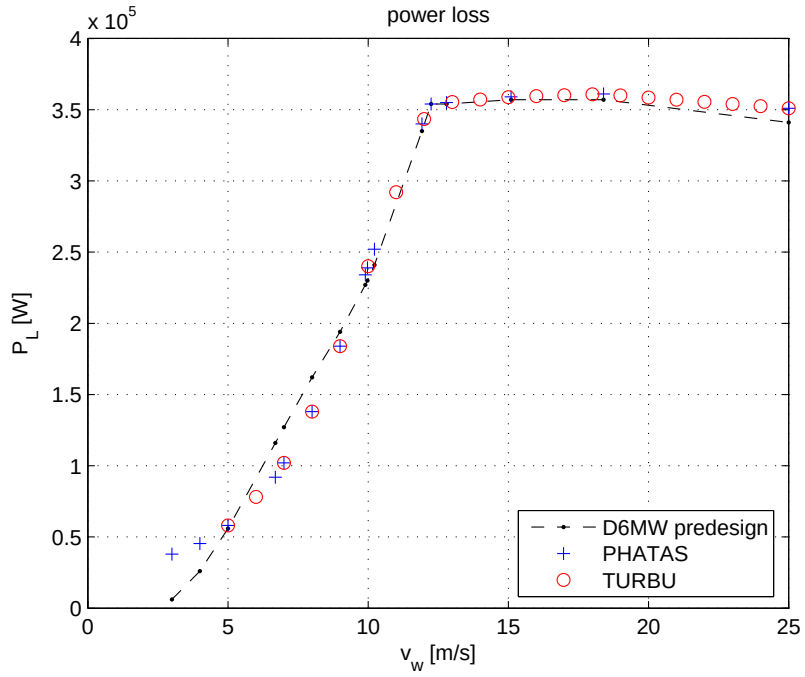

Figure 10: Power losses for original D6MW design compared to PHATAS and TURBU model

Both the operational data and the equilibrium state (loading and deformation) of the two wind turbine models show small differences.

The blade pitch angle determined during linearization of the control algorithm from the CDT does not provide the correct working point to achieve rated power. The automatic search also does not find the correct working point. This is corrected by hand, reducing the pitch angle above rated with 1.35 degrees to get rated power of 6MW. The resulting angles do match with the equilibrium from PHATAS.

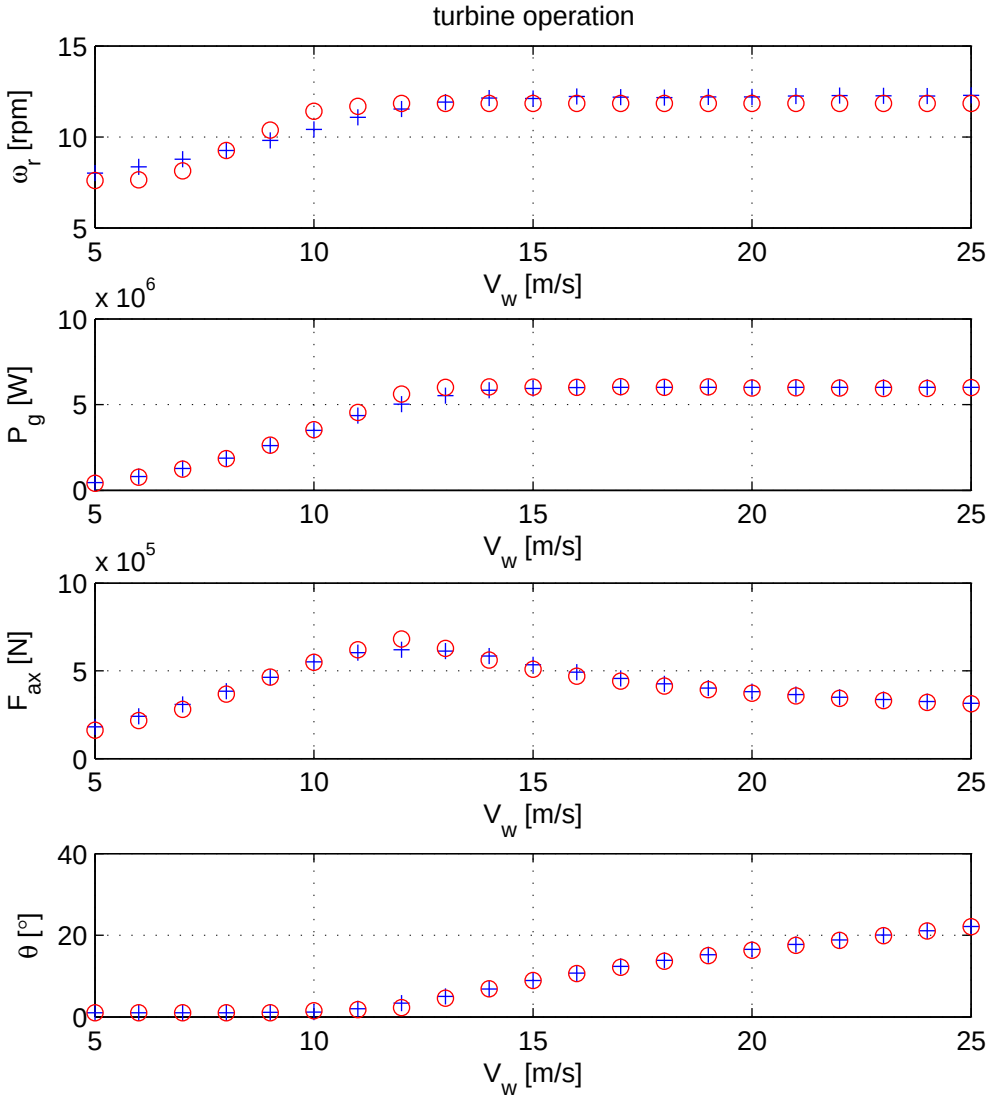

Figure 11: Turbine operation of PHATAS (bx) and TURBU (ro) model compared

The difference near rated in axial thrust and blade flap moments is caused by less peak shaving in TURBU. Peak shaving is a control strategy for load reduction near rated wind speed (maximum thrust), which slightly increases the blade pitch angle to shave off the sharp load peak. The PHATAS pitch angle at 12m/s is indeed larger than the TURBU working point. As pitch angle is selected by hand, this can easily be adjusted.

The fore aft tower base moment (and fore aft tower top deformation) shows an offset across the whole operating range of approximately 5%; this is not due to wind loading (good match of axial thrust on the rotor).

The side to side tower data also has an offset of 5% at high wind speeds; this is probably due to drive train loss that is not accounted for in TURBU (the loads are based on the full aerodynamic torque).

A deviation in torsion blade root moment, caused by reversal of the aerodynamic moment on the blade within TURBU, was solved during this project (discussed in more detail in appendix C).

As fatigue is caused by load variations, the stationary loading has no direct impact on this. However, it changes the equilibrium state of the wind turbine, which in turn also affects load variations.

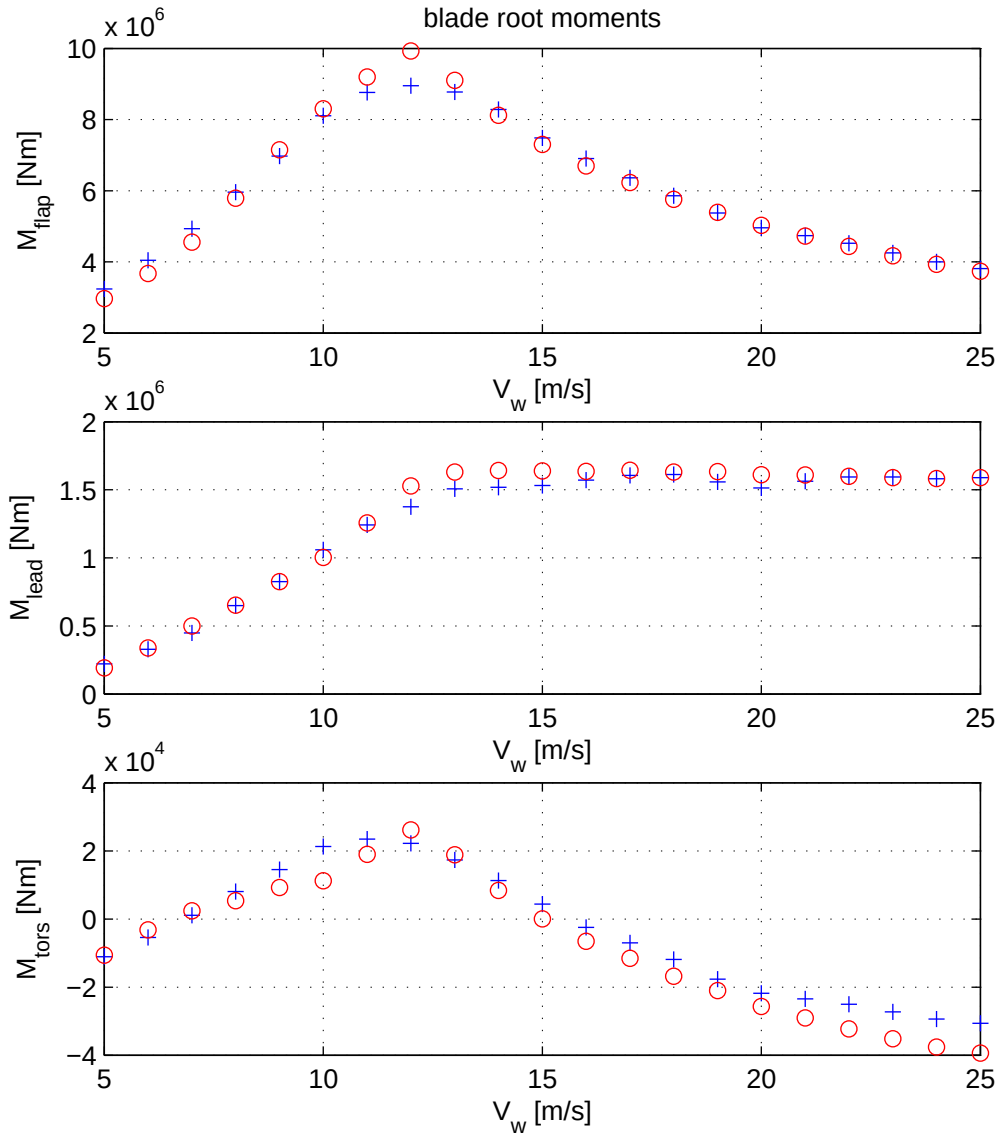

Figure 12: Equilibrium blade root moments calculated with PHATAS (bx) and TURBU (ro) for different wind speeds across the operating range.

2.4.3 Modal analysis

The linearized TURBU model can be decomposed to find the modes of the wind turbine under the specified operating conditions. PHATAS also calculates some of the first eigenfrequencies of the model in each working point. Stepping through the total operating range, a full description of the wind turbine behaviour is constructed and models can be compared.

The modal parameters plotted against increasing wind speed in figure 16.

2.4.4 Power spectra of load signals

Not only modal parameters, but also load spectra of the wind turbine model can be used to compare the TURBU model with PHATAS. Two methods are available in TURBU to obtain these spectra.

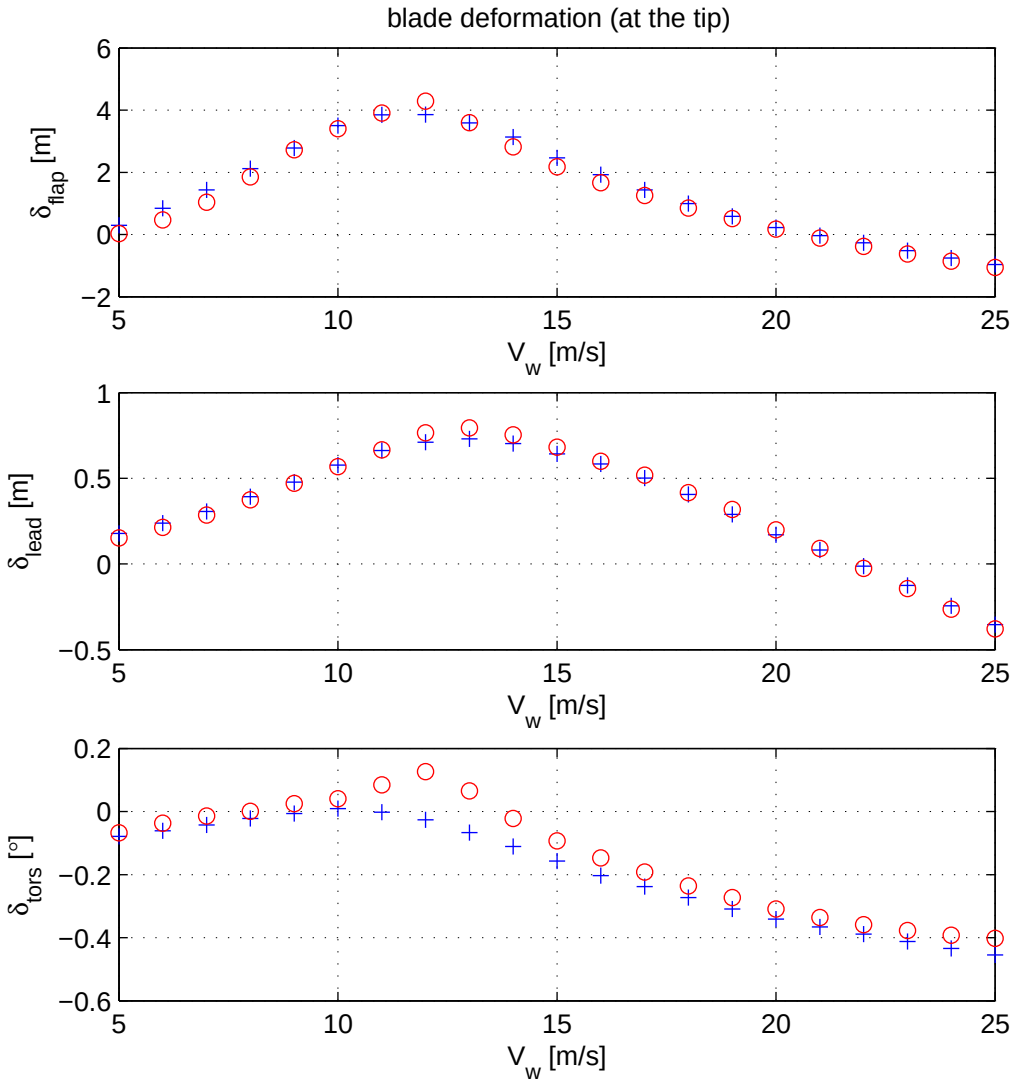

Figure 13: Equilibrium blade tip deformation calculated with PHATAS (bx) and TURBU (ro) for different wind speeds across the operating range.

1 directly from frequency domain formulation From application LOAD in TURBU, the power spectra of the blade root and tower base moments of the wind turbine model in operation (subject to wind, wave and gravity loading) can be obtained.

2 indirectly from load histories (time domain simulations) Next to the direct formulation in the frequency domain, these spectra can also be extracted from TURBU time series using FFT methods.

The results (time series) from PHATAS are processed with the second method. An example of the resulting time series (tower base side to side bending moment) from both codes is shown in figure 17. As expected, the plot shows a lightly damped oscillation of the first tower mode.

The wind (in rotating reference frame) and wave excitation spectra are shown in figure 18. Figure 19 shows the blade root moment spectra and figure 20 the tower base moment spectra, both calculated from time series at above rated wind speed of 15 m/s. The overall FFT results from PHATAS and TURBU match very good, both eigenfrequencies and associated damping. The blade flap (and resulting fore aft tower moments) are underestimated by TURBU below 0.1Hz,

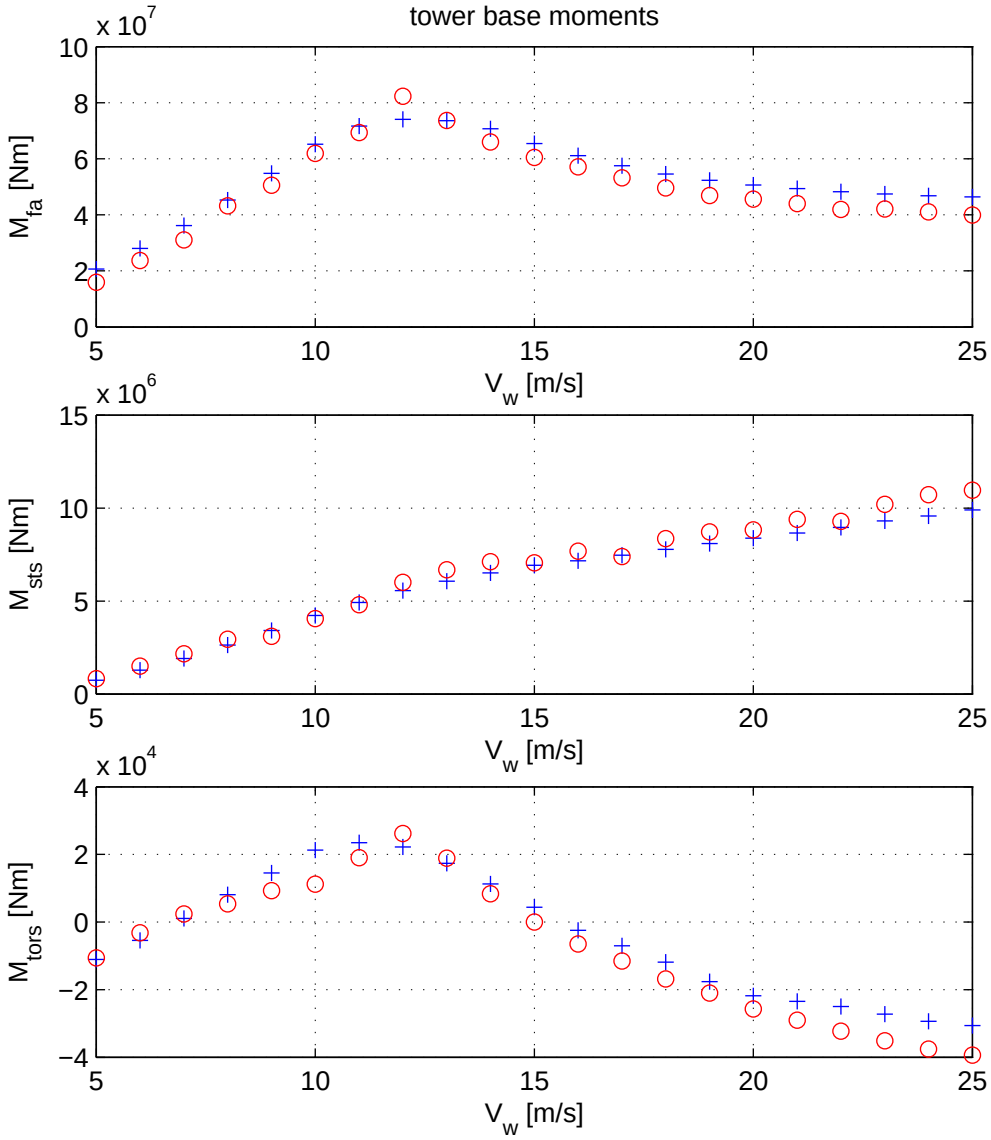

Figure 14: Equilibrium tower base moments calculated with PHATAS (bx) and TURBU (ro) for different wind speeds across the operating range.

in the region of wind excitation. For the blade flap TURBU is 20dB lower in PSD (which is a factor $\sqrt{10} \approx 3$ in blade flap moment). The underestimation can be partly explained through the linearization in the 15 m/s working point. A blow-up of the area around 15m/s in the upper box of figure 12 would show a stronger *increase* of δ_{flap} below 15m/s than *decrease* above 15 m/s. This implies that the increase of flap loads during wind fall is underestimated in TURBU as concerns the 15 m/s working point. The peak at 4Hz in the side to side tower FFT differs in frequency.

2.4.5 Fatigue load

In this section some first results on fatigue loads as calculated with PHATAS and TURBU are presented. The theory behind fatigue analysis is covered in chapter 4.

Throughout this report, an equivalent load is used for fatigue analysis. The equivalent 1Hz (eq1Hz) fatigue load is the single load amplitude with a frequency of 1Hz that represents the fatigue loading of the sum of all the different amplitudes during the considered time series. The

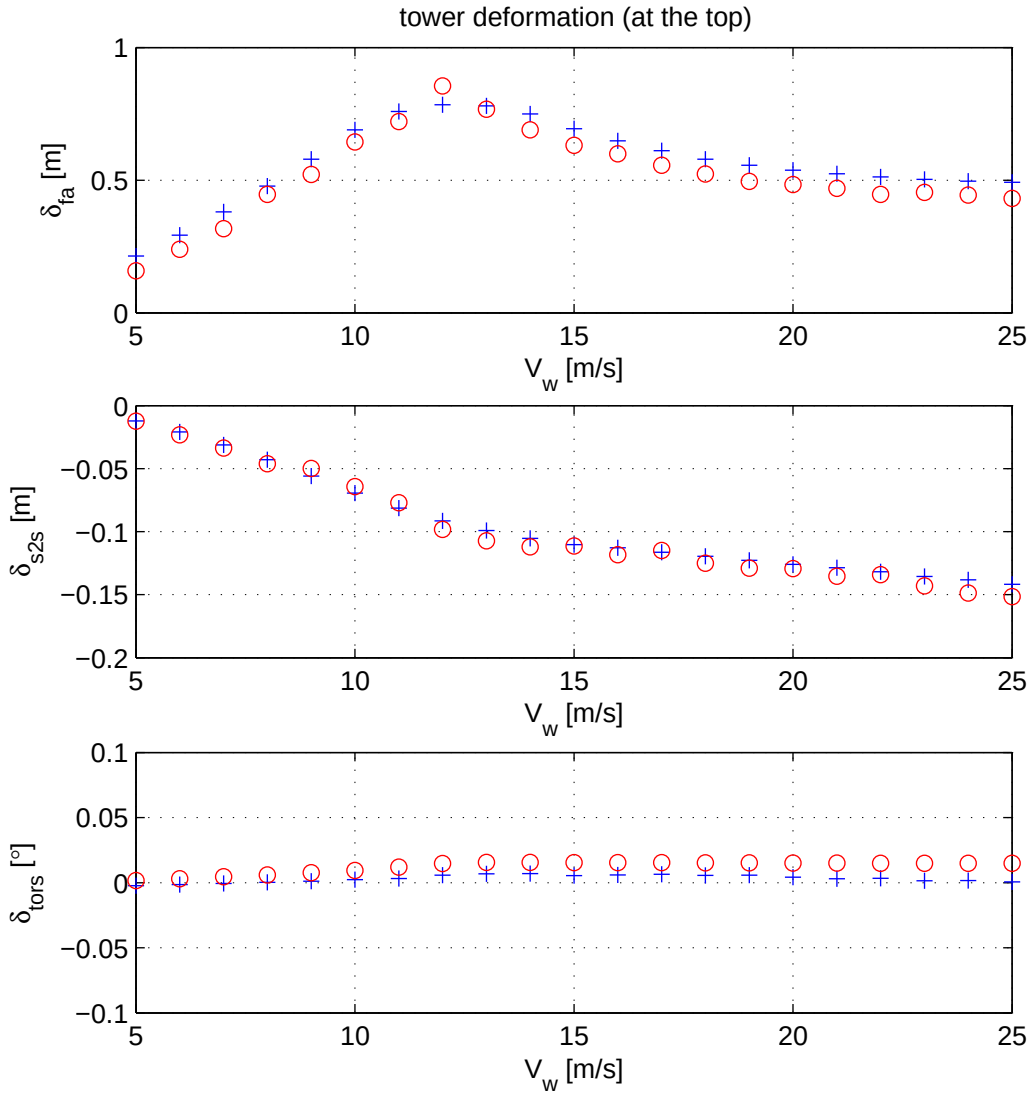

Figure 15: Equilibrium tower top deformation calculated with PHATAS (bx) and TURBU (ro) for different wind speeds across the operating range.

equivalent 1Hz fatigue loads for the selected test cases (see table 1) are shown for the blade root moments in figure 21 and the tower base moments in figure 22. As representation of the actual fatigue, the average of the fatigue during six 10min time series is used. Table 7 shows the values of the calculated eq1Hz fatigue loads and the standard deviation σ within the set of six series. Table 6 shows the calculated eq1Hz fatigue loads compared for wind speed of 15m/s.

Table 6: Fatigue loads for case 5 (wind speed of 15m/s)

		PHATAS		TURBU	
case	load	M_{eq1Hz} [Nm]	σ [Nm]	M_{eq1Hz} [Nm]	σ [Nm]
5	B_{flap}	9.133e+006	3.612e+005	8.390e+006	3.692e+005
5	B_{lead}	7.338e+006	9.661e+004	7.492e+006	1.298e+005
5	B_{tors}	1.691e+005	1.001e+004	1.204e+005	5.948e+003
5	T_{fa}	2.799e+007	2.031e+006	2.073e+007	7.350e+005
5	T_{sts}	1.435e+007	2.274e+006	1.246e+007	2.129e+006
5	T_{tors}	3.932e+006	4.105e+004	4.592e+006	1.030e+005

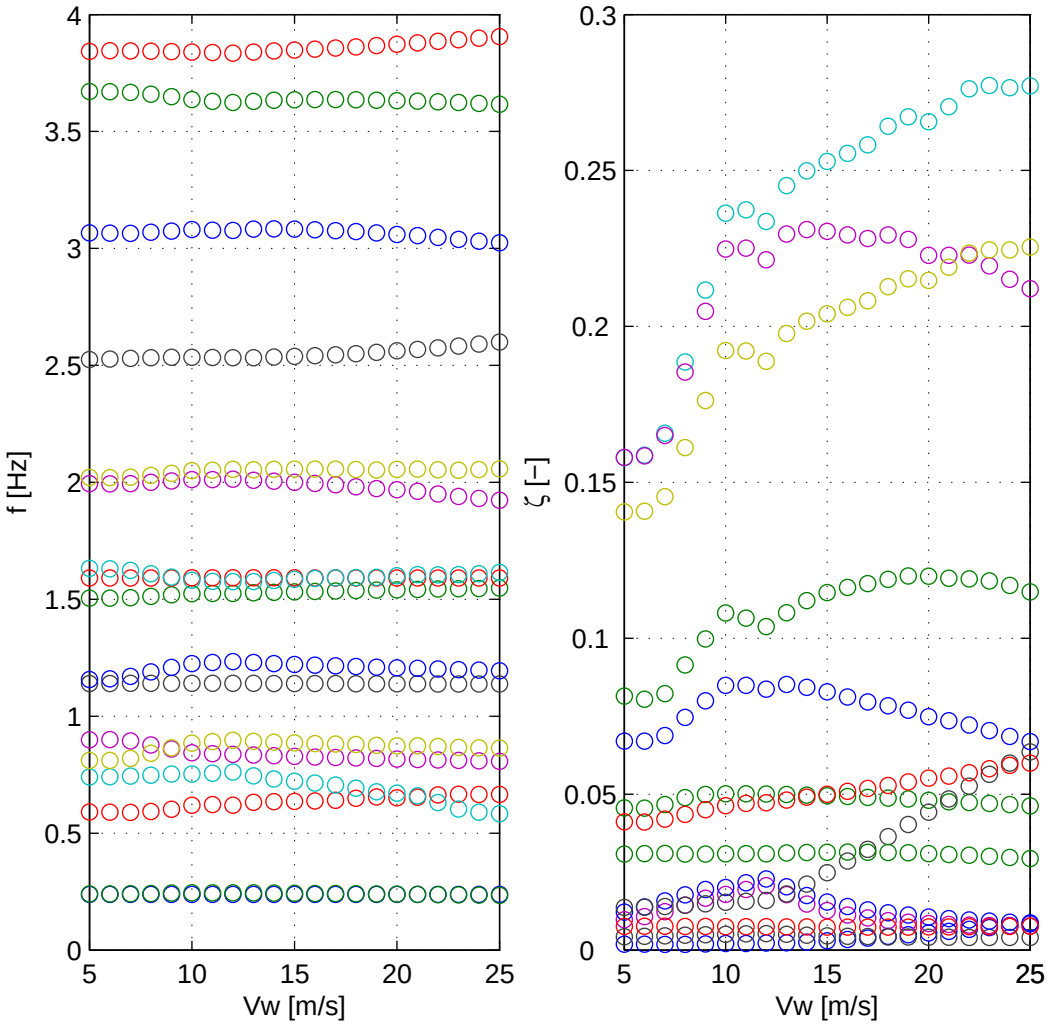

Figure 16: Modal parameters (frequency and damping) of the D6MW model for increasing wind speed.

Table 7: Tower base side to side fatigue for all test cases

		PHATAS		TURBU	
case	v_{wind} [m/s]	M_{eq1Hz} [Nm]	σ [Nm]	M_{eq1Hz} [Nm]	σ [Nm]
1	5	4.603e+006	8.835e+005	2.269e+006	6.248e+005
2	8	8.338e+006	1.586e+006	4.585e+006	9.020e+005
3	10	1.203e+007	3.432e+006	6.260e+006	8.829e+005
4	12	1.175e+007	2.356e+006	8.851e+006	2.492e+006
5	15	1.435e+007	2.274e+006	1.246e+007	2.129e+006
6	20	1.547e+007	1.376e+006	1.984e+007	4.366e+006
7	25	2.317e+007	3.665e+006	2.543e+007	4.204e+006

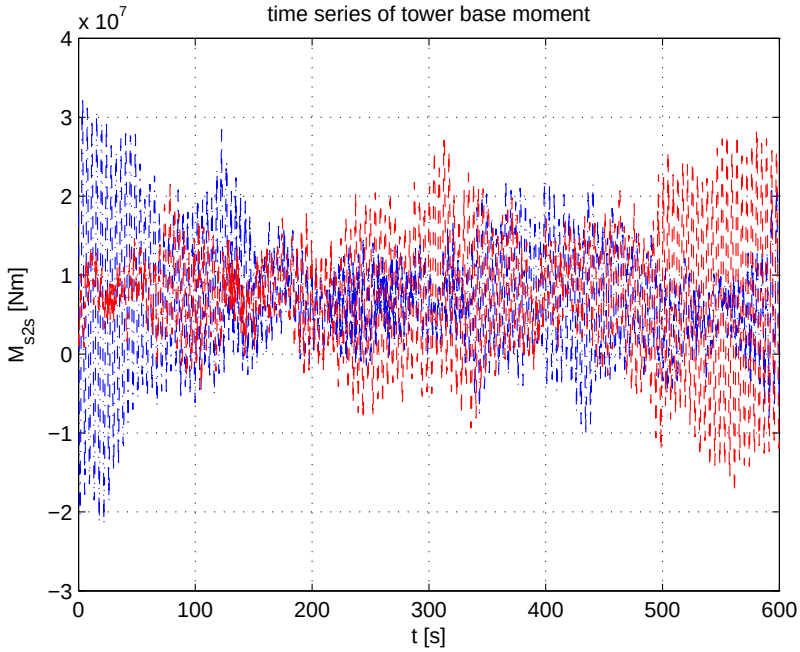

Figure 17: Time series of the side to side tower base moment ($V_w = 15m/s$)] from PHATAS (b-.) and TURBU (r–).

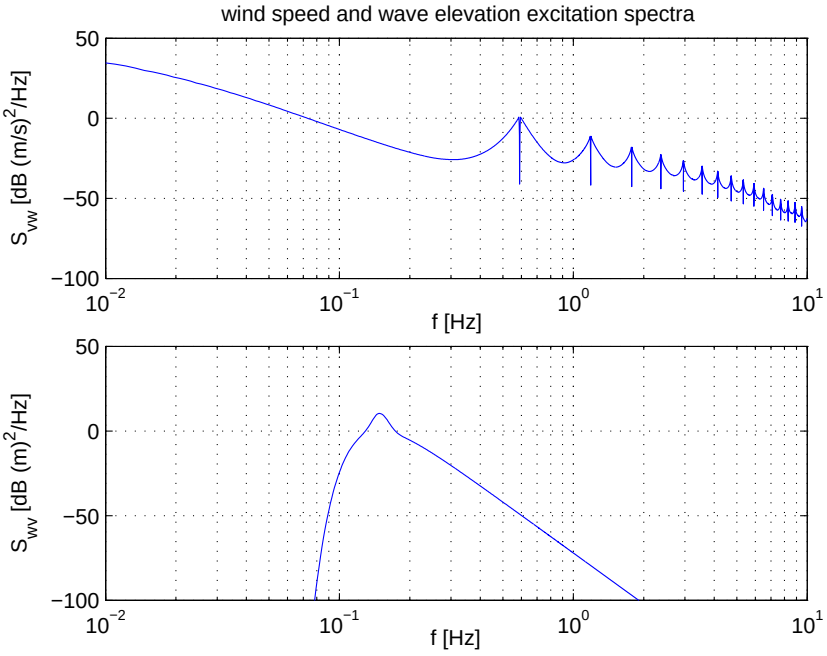

Figure 18: Wind and wave exitation spectra ($V_w = 15m/s$).

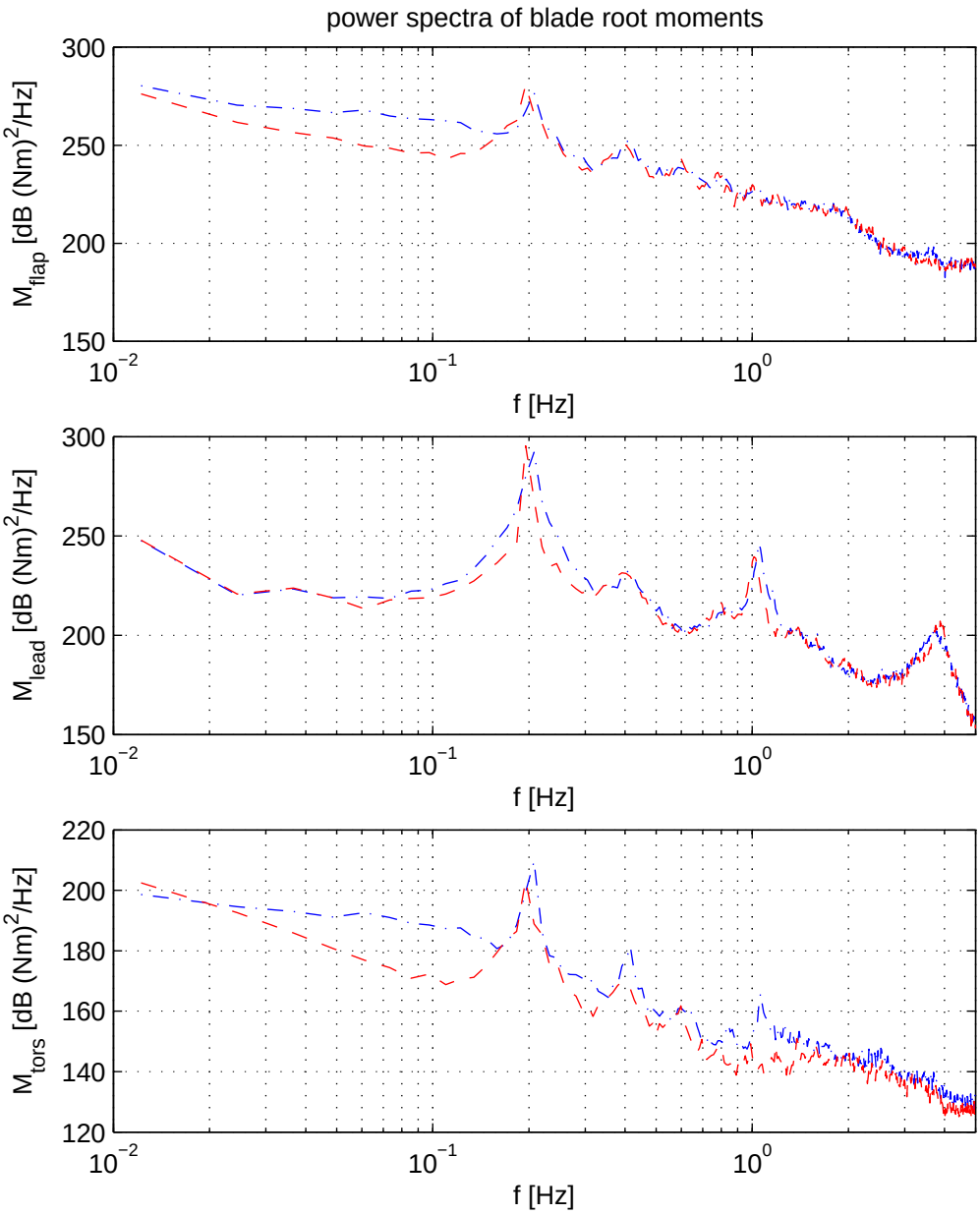

Figure 19: Spectra of the blade root moments ($V_w = 15m/s$) calculated with PHATAS (b-.) and TURBU (r–).

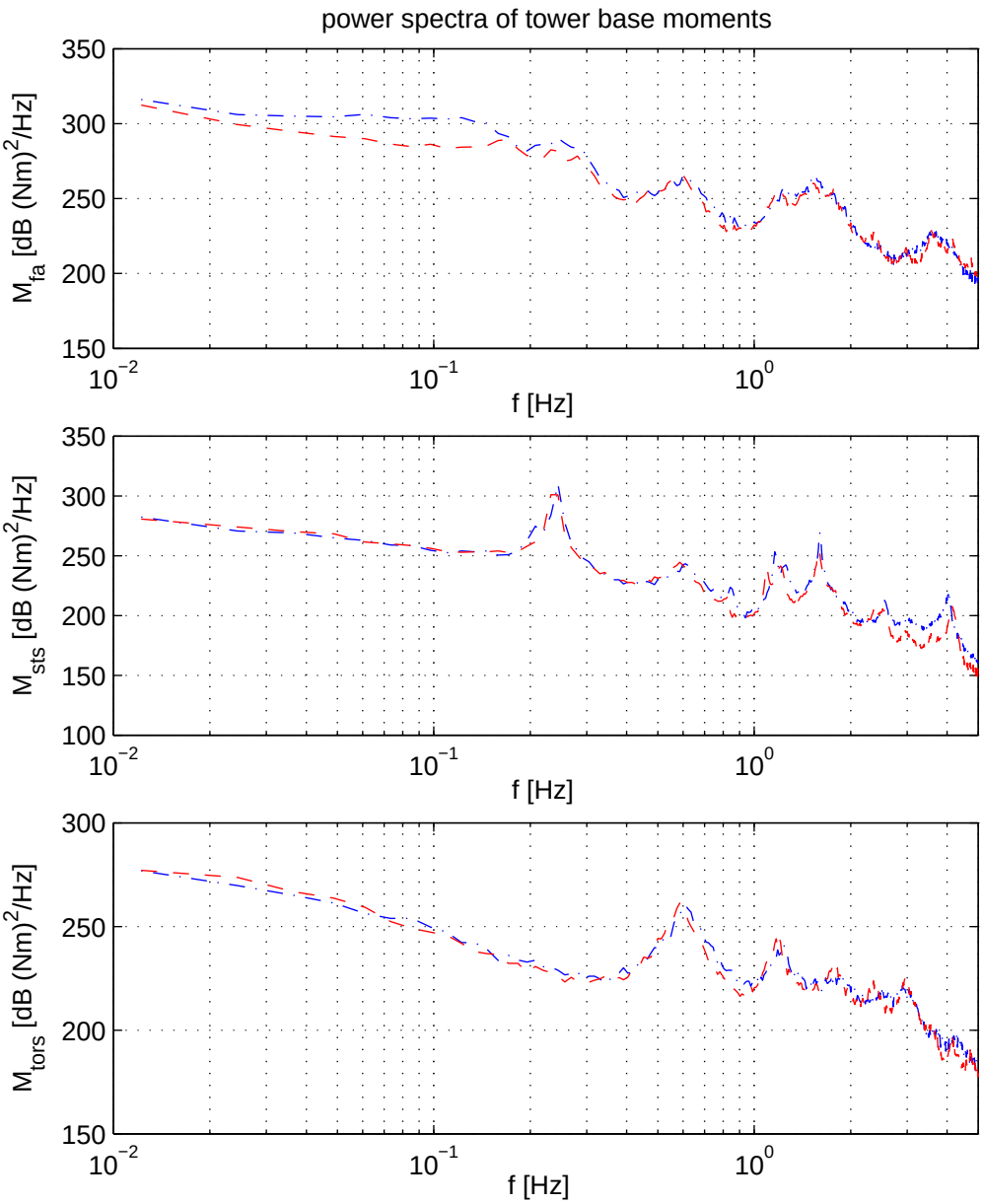

Figure 20: Spectra of the tower base moments ($V_w = 15m/s$) calculated with PHATAS (b-.) and TURBU (r–).

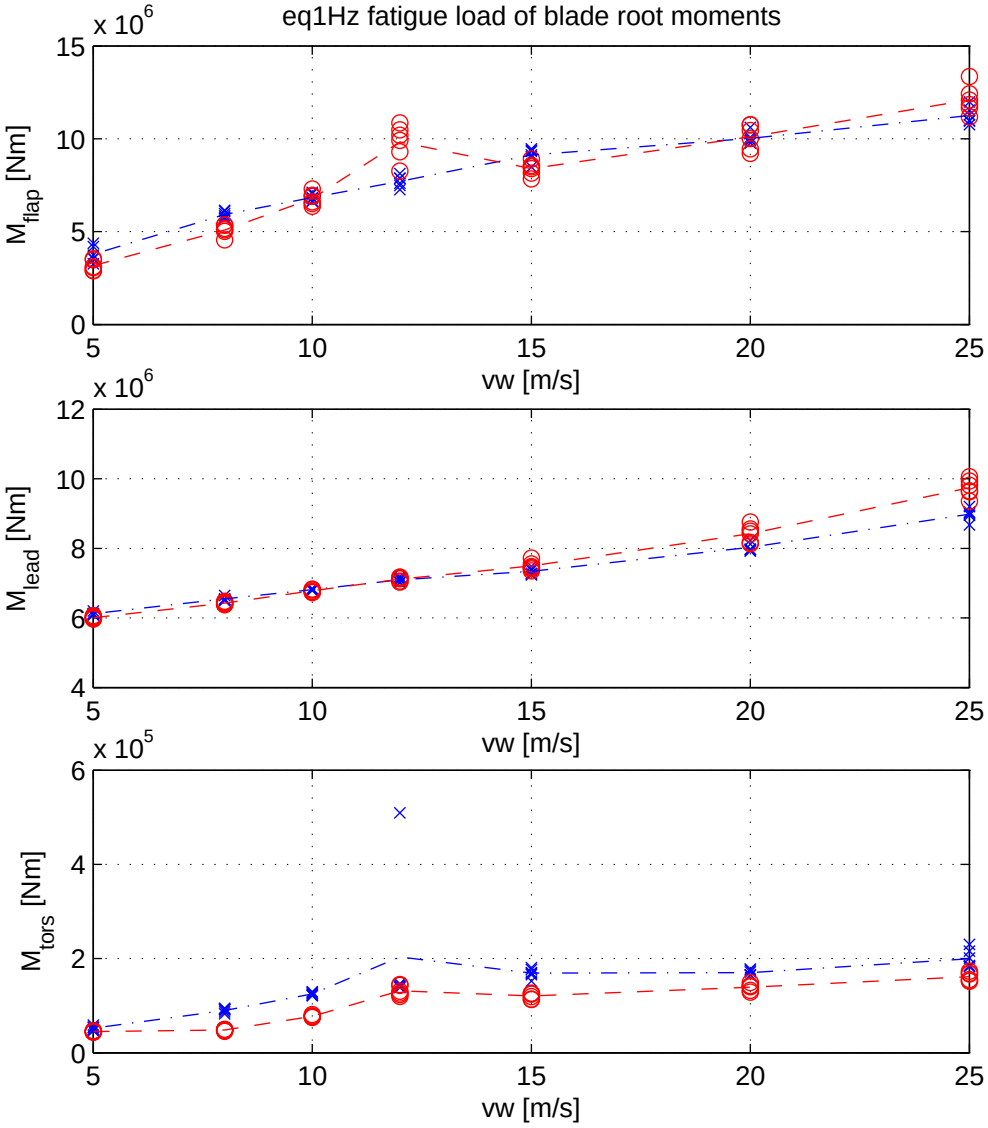

Figure 21: The equivalent 1Hz fatigue loads on the blade root calculated with PHATAS (bx) and TURBU (ro). The markers are the individual results and the lines the average of the six load series.

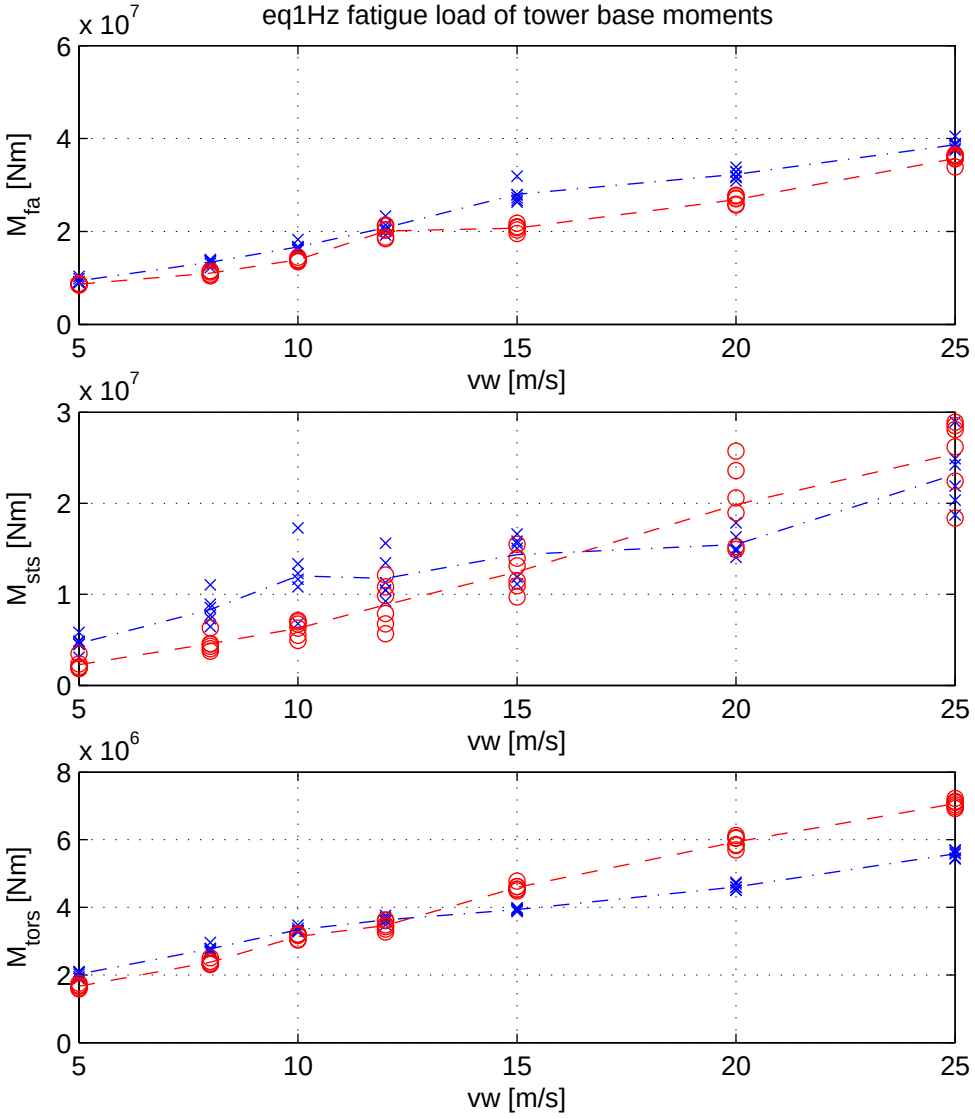

Figure 22: The eq1Hz fatigue loads on the tower base calculated with PHATAS (bx) and TURBU (ro). The markers are the individual results and the lines the average of the six load series.

3 Integral design methods

This chapter gives a glance at some of the integral design methods that come available with the development of TURBU. The two sections focus on characterization of the wind turbine dynamics and design optimization respectively.

3.1 Characterization of the wind turbine

In the design phase, it is essential to have a characterization of the wind turbine dynamics and loading. When this description covers the whole operating range, it can be considered a footprint of the wind turbine. Whereas nonlinear tools would need long calculation times to derive such a footprint, with TURBU it can be obtained fast enough (minutes) to be used for design iteration.

A common method for visualization and analysis of the whole working range of a wind turbine is the so called Campbell diagram. In this section, a new method is shown using actual power spectra of load signals. The idea behind this visualization comes from Rossetti et al. (2008). As an example, this method is applied to several situations (section 3.1.3), for instance to show the influence of water depth on the D6MW design.

3.1.1 Description of the method

In rotational machinery the influence of rotational speed on the system dynamics is often shown with a Campbell diagram. In a traditional Campbell diagram, frequency of eigenmodes are plotted against rotational frequency. The intersections, called critical speeds, between 1p, 2p etc. rotational speed lines and the eigenfrequencies indicate potential problems. The original Campbell diagram of the D6MW predesign (from Kooijman et al. (2003)) is shown in figure 23.

The shown power spectral density contour plot (figures 24 and 25) is a modified Campbell diagram. It combines load spectra at different operating points with 1p, 3p etc. lines of rotational speed. The spectra are plotted in an easy to read two axes, 3D graph, where the magnitude is represented by color. In addition to the load spectra, the eigenfrequencies of the wind turbine can be drawn to show their dependence on operating point and to make a clear distinction between system dynamics and excitation effects. From this diagram the critical points in the operating region can easily be identified. As different from the Campbell diagram, this is done using the actual (simulated) loads on the system. The ability to compare the relative impact of the occurring critical speeds on the wind turbine loading improves the selection of the critical operating points.

Main advantages of this visualization technique:

- gives an overall picture of the wind turbine dynamics throughout its operating range
- improves the selection of critical operating points, by assessing actual loads on the system

Due to the overview on the system in operation, areas of application can be structural design, control design and even measurement/monitoring existing wind turbines. In theory this diagram can be constructed from both simulated as well as measured data, although it requires a lot of measurements (40+ for 5-25 m/s region) to obtain a smooth fill of the contour. A relatively constant mean wind speed is also required.

3.1.2 Implementation of the method in TURBU

This method makes use of the ECN code TURBU, both for modeling the wind turbine, as for the calculation of load spectra in the frequency domain. The main steps in the construction of the shown power spectral density contour plot are listed below.

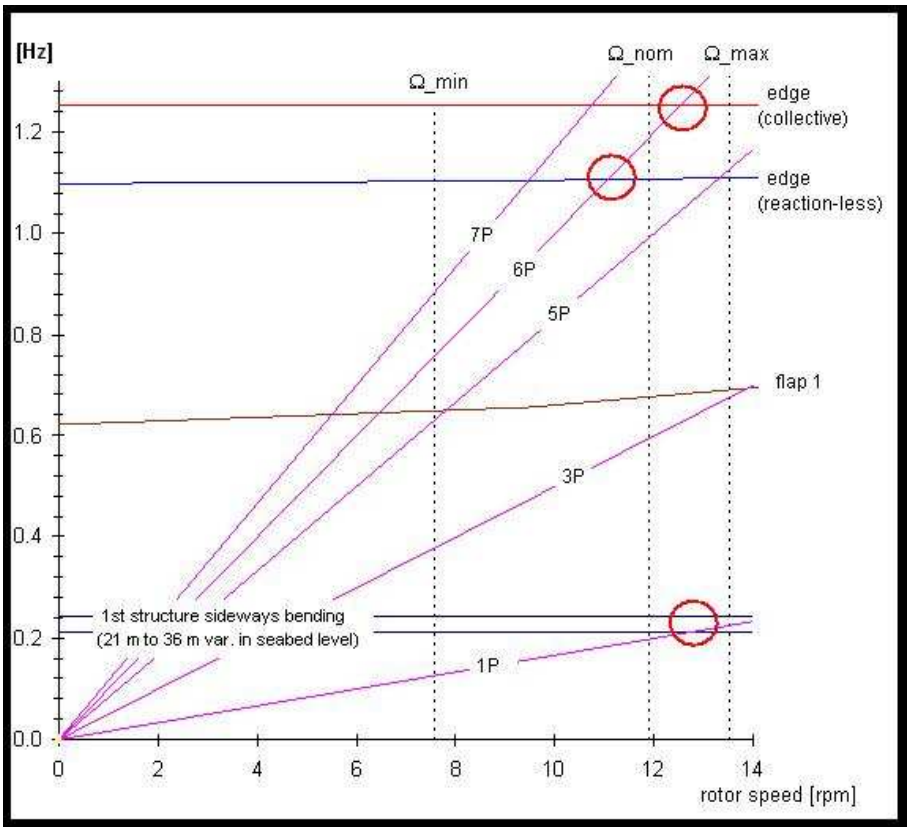

Figure 23: Original Campbell diagram for the D6MW wind turbine, taken from Kooijman et al. (2003). Remark: the mode at 1.1Hz is a backward whirl mode, which could be excited by the 5P&7P rotational frequencies.

1 find operating points for a specified fine grid of mean wind speeds
Run the control loop within TURBU (function `tbuctrlomgparprl()`) with Control Design Tool data file `fileFBomgCDT.mat` and the array of required wind speeds to obtain the working points [V_{wind}, Ω, θ].

2 use TURBU in a `for` loop to calculate power spectra in all operating points
The approach here is to build the loop around the TURBU code, which involves modifying the input parameter files for each new operating point. Save the calculated spectra in a result file, along with the operating points (and system matrix if Eigen frequencies lines are also desired).

3 plot the spectra as a 2D filled contour with MatLAB function `contourf()`

4 add 1p, 3p, 6p etc. rotational speed lines using saved operating points

5 (add eigenfrequencies as dots for each operating point, not shown in the figures)

The result as shown in the figures 24 and 25 is obtained in a couple minutes.

3.1.3 Application of the method

The analysis method with the modified Campbell diagram is applied to a test case: the effect of increasing water depth on the dynamics of the whole wind turbine.

influence of water depth on D6MW dynamics

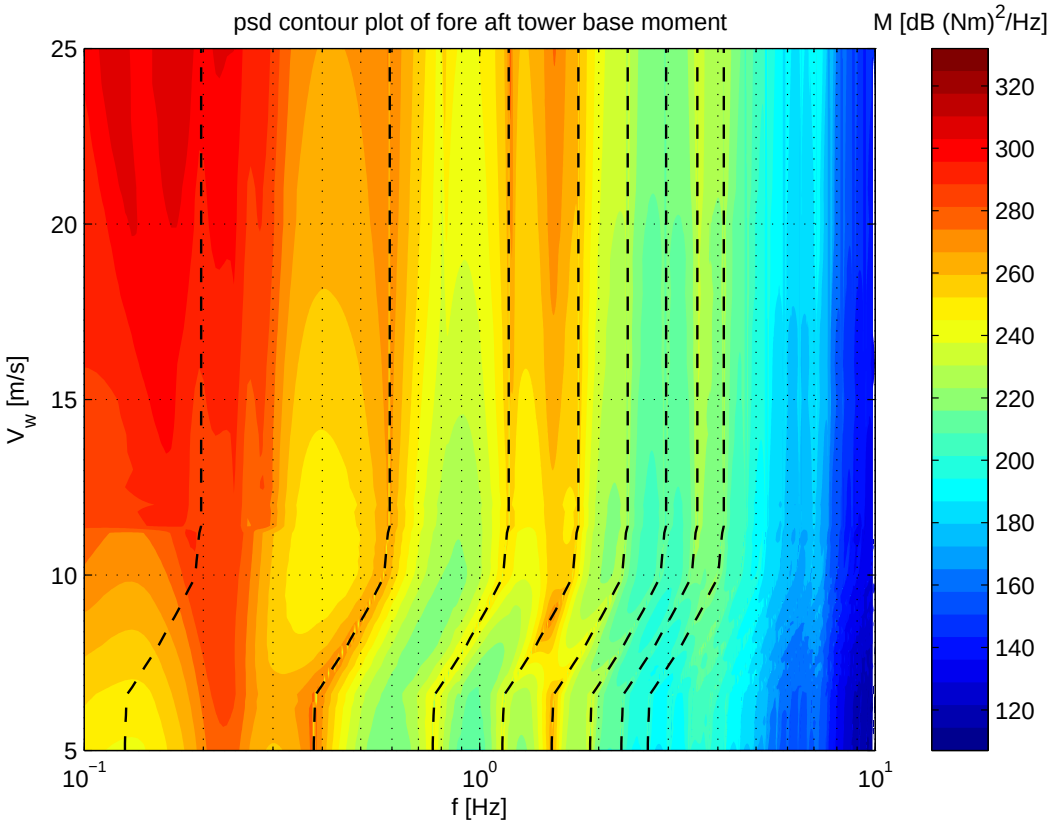

Figure 24: Modified Campbell diagram for the fore aft tower base moment, created from actual loading on the wind turbine. The dashed lines represent the 1P, 3P, 6P etc. frequencies of the rotor. The critical points, from rotation, loading or resonances, can easily be selected.

The water depth at an offshore site is not the same for each wind turbine, due to roughness and slope of the sea bed. As offshore wind farms become larger this will only increase. Scour (sand at sea bed washed away from the support structure) also increases the effective water depth (and length) of the support structure. This water depth, and the resulting support structure length for a certain hub height, is an important parameter for the design of wind turbines. It directly affects the support structure eigenfrequencies. For large offshore wind turbines, the first eigenfrequency is very critical. It lies between the wave loading and the 1P rotor speed.

Shown in figure 26 and 27 are the modified Campbell diagrams for two increased water depths (26m and 31m). The foundation stiffness is adjusted accordingly. The support structure pile diameter and wall thickness are kept constant, as if the same wind turbine assembly stands in deeper water. As the first frequency of the support structure decreases, it moves towards the 1P loading. The second tower bending mode also decreases and comes near the 6P speed of the rotor.

3.2 Optimization

In this section, the use of TURBU for optimization of wind turbine design is examined. The first section gives a description of the used method. The last section shows results on two cases: tower stiffness and peak shave pitch angle.

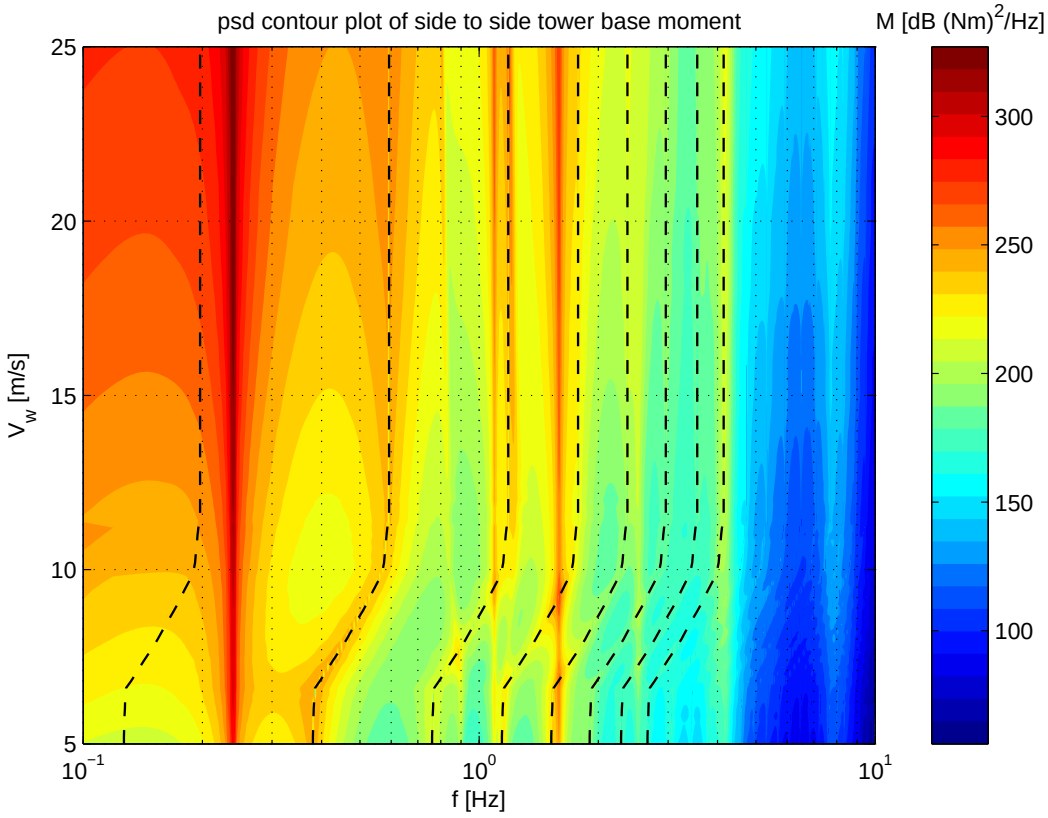

Figure 25: Modified Campbell diagram for the side to side tower base moment, created from actual loading on the wind turbine. The dashed lines represent the 1P, 3P, 6P etc. frequencies of the rotor. The critical points, from rotation, loading or resonances, can easily be selected.

3.2.1 Method for optimization with TURBU

For optimization, it would be convenient to have a single measure of wind turbine performance. This would be cost of energy, where it all comes down to. To determine the contribution of for instance blade fatigue on the cost of energy is not straightforward. On the other hand, ideally there is only a single design driver. However this is also not a real life situation, certainly not for a complex system as a wind turbine.

The optimization approach followed here is parameter variation. This is not an automated process, but still requires a lot of wind turbine design knowledge. The designer determines the driver and where to look for the optimum (performance).

The basic output from TURBU consists of working point equilibrium (mean) and frequency spectra of the selected outputs (variation). Using Parseval's theorem for real-valued processes a single measure of the performance can be obtained from the power spectra (Balmer (1997)); taking the square root of the cumulative power spectral density gives the standard deviation (17). Together, the mean and standard deviation define the output and are used for selecting the optimum. For most cases this is a useful measure, but for some situations extreme values (minimum blade tip tower clearance for instance) are design driving. Which measure to select is also up to the wind turbine designer.

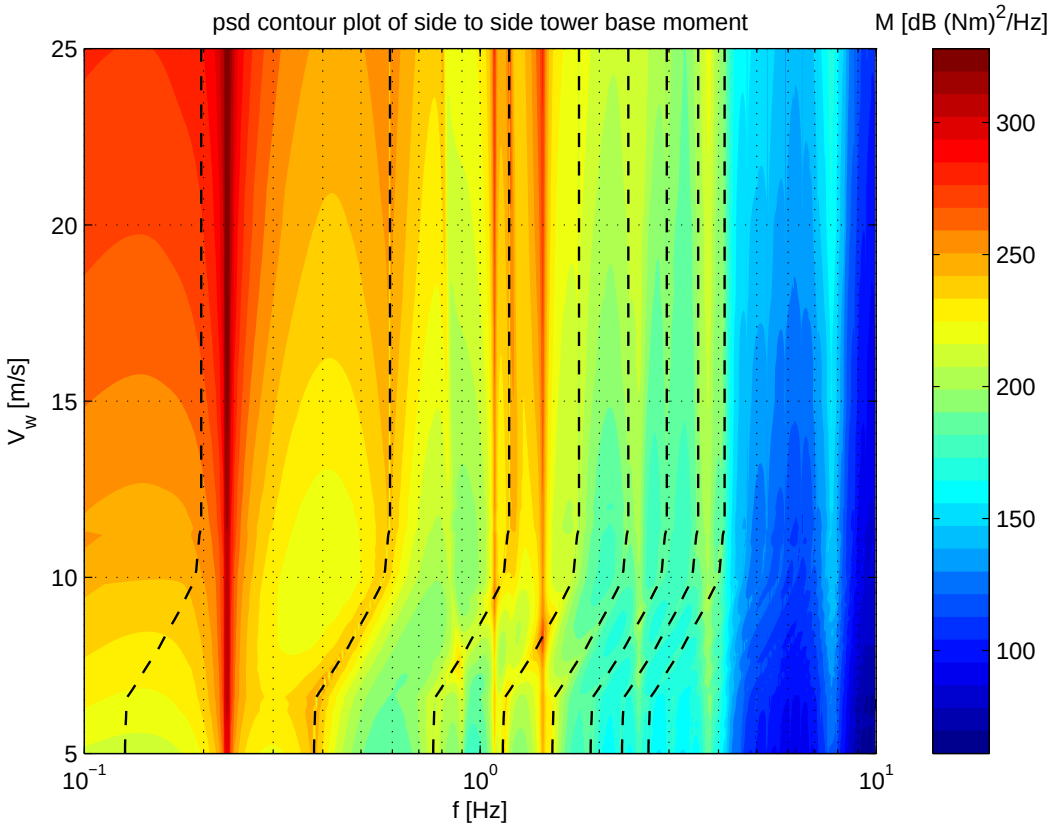

Figure 26: Modified Campbell diagram for the side to side tower base moment at 26m water depth.

$$\sigma = \sqrt{\mathrm{E}[x(t)^2] - \mu^2}$$
with
$$\mathrm{E}[x(t)^2] = \int_{-\infty}^{\infty} S(f)\mathrm{d}f \tag{17}$$

3.2.2 Application of optimization

Now the performance indicators are estabished, the optimization is applied to two cases. The cost functions are just examples to show the effect of weighing gain and load.

tower stiffness

As already discussed before, tower stiffness is an important design parameter because it determines the eigenfrequencies of the support structure of a wind turbine. In TURBU, the stiffness of the tower (modelled as multibody system) can easily be scaled with multiplication factors, both fore aft and sideways (`mlSsfraf` and `mlSsside`). In this section, parameter variation on the tower stiffness shows the balance between loading and (material) cost. The variation on the tower bending moment is used as measure of loading, while tower mass defines material cost. Important to note that this search gives a first estimate of the possible stiffness values. The tower design should also be checked on buckling and tower top displacement for instance.

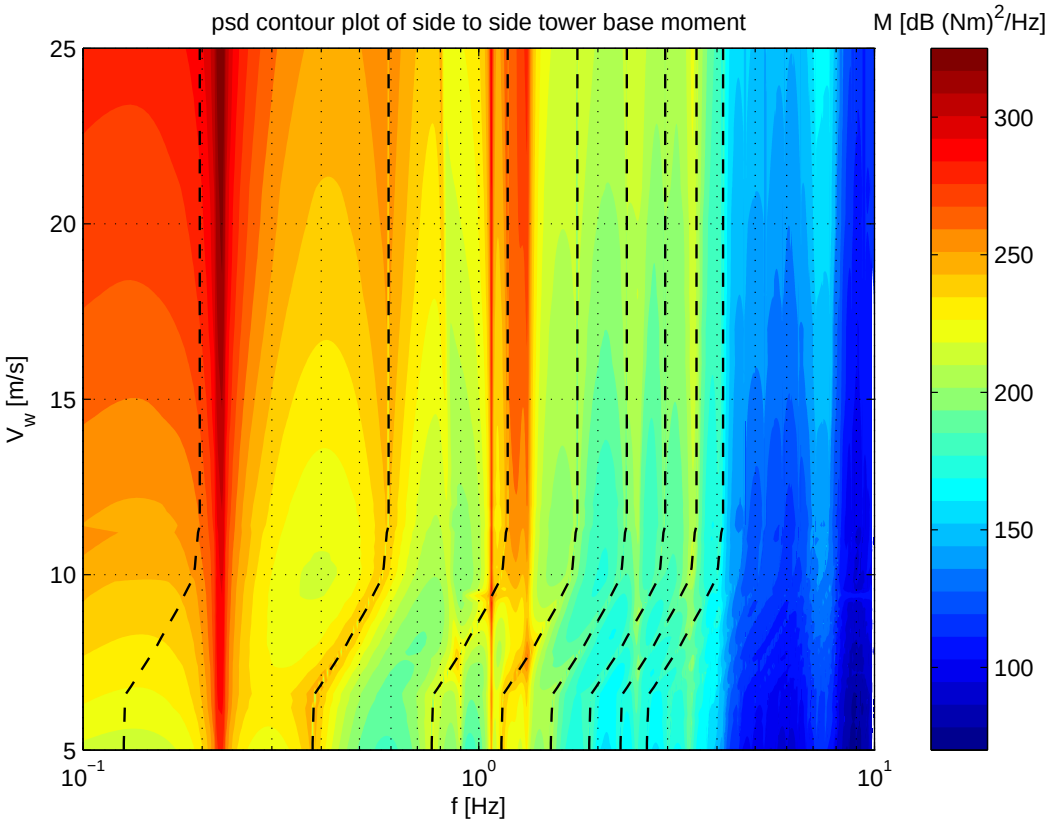

Figure 27: Modified Campbell diagram for the side to side tower base moment at 31m water depth.

The relation between stiffness (EI) and mass (m) for a cylinder with diameter d and height h is derived with equation 18.

$$\begin{aligned} EI &= E \cdot \tfrac{\pi}{64} \cdot (d_{out}^4 - d_{in}^4) \\ m &= \rho \cdot \tfrac{\pi}{4} \cdot (d_{out}^2 - d_{in}^2) \cdot h \\ EI &= \tfrac{E}{\rho \cdot h}(\tfrac{m \cdot d_{out}^2}{8} - \tfrac{m^2}{4\pi \cdot \rho \cdot h}) \end{aligned} \tag{18}$$

It appears that for $\rho \cdot h >> d_{out}^2$, in SI units, the mass of the tower is proportional to its stiffness ($m \propto EI$), which is usually the case for wind turbines.

Figure 28 shows the balance between loading and cost for the chosen cost function. Obviously, the rotational speed has big impact on the result. In figure 29, the stiffness variation for the whole operating range is shown.

peak shaving blade pitch angle

Peak shaving is a method to reduce the load near rated wind speed. When rated wind speed is approached, the aerodynamic load increases rapidly. As the blades start to pitch above rated (to loose power), the load drops. This peak load can be reduced by already starting to pitch somewhat before rated wind speed. The downside is the loss of produced power at rated wind.

The selection of the peak shave pitch angle can be cumbersome. On the one hand there is the peak load (blade flap moment), on the other the produced power (inverse proportional to cost). Figure 30 shows the result of the parameter variation.

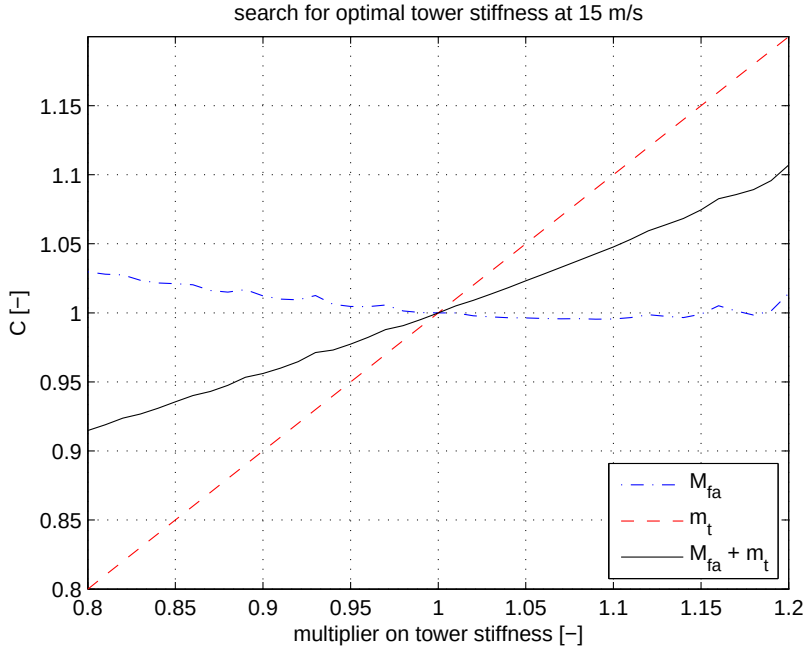

Figure 28: Optimization of the tower stiffness, for a cost function that balances load and material cost, at above rated wind speed (15m/s) and rated rotor speed (11.8rpm).

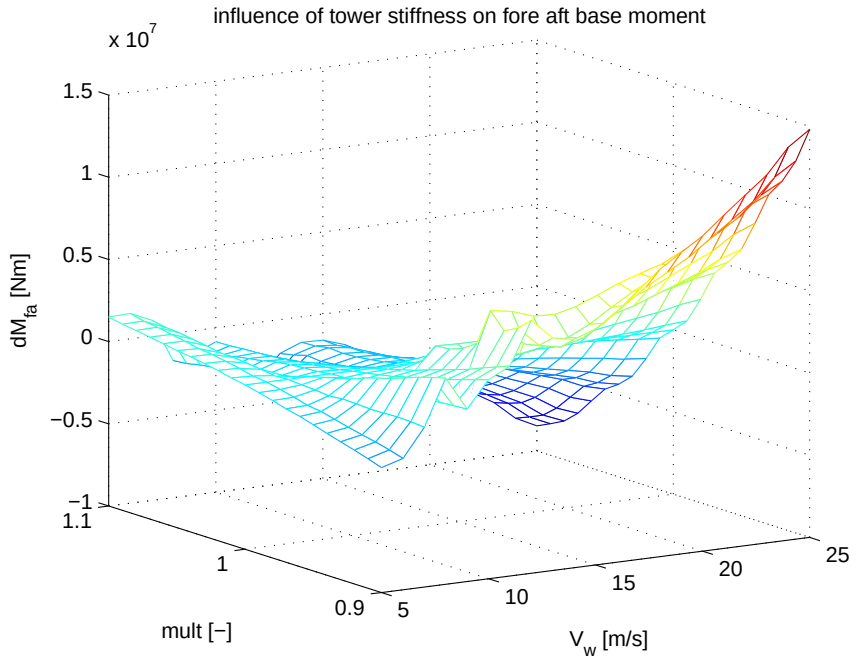

Figure 29: Influence of tower stiffness on the fore aft tower base moment. At above rated wind speeds, the added load dM_{fa} with respect to the reference situation at $mult = 1$ increases with decreasing tower stiffness.

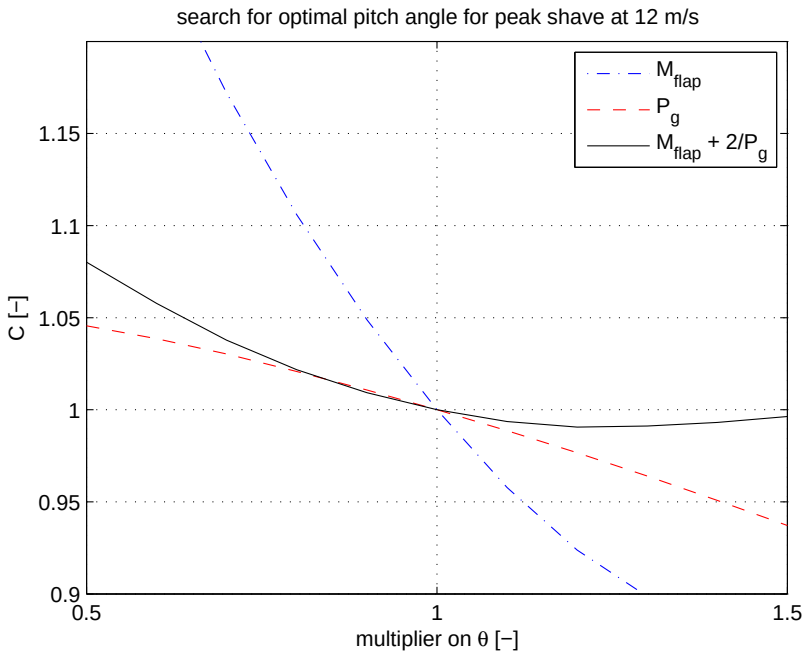

Figure 30: Optimization of the peak shave pitch angle at rated wind speed, for a cost function that balances load and produced power.

4 Fatigue analysis

Fatigue is one of the design drivers for wind turbines, due to long lifetime combined with relatively high rotational speed. Offshore, wave loading and water current have to be included in the analysis, which drastically increases the number of load cases. The calculation time involved using non linear time domain tools will also increase beyond acceptable values. Is it possible to use the fast linear frequency domain tool TURBU to determine sea states contributing to fatigue? The resulting reduced set of load cases could then be analyzed in detail with a nonlinear time domain tool.

This chapter starts with some background theory on fatigue. Then life time fatigue damage calculated with TURBU shown for different wind turbine components. The full sea state scatter diagram (also including wind and wave direction) calculated with TURBU is analyzed and worst cases for fatigue are selected. Finally, the results are compared with PHATAS, including the influence of hydrodynamic loading on fatigue

4.1 Fatigue theory

Fatigue is the progressive structural damage that occurs when a material is subjected to cyclic loading, even when stress levels remain well below the yield stress. One of the methods to calculate fatigue damage is rainflow counting. This method is described in several standard books on wind turbine (fatigue) load analysis such as Madsen (1990). The result of this counting sequence is an histogram containing the number of load variations that occurred within specified load bins during a time record, which can be from simulations as well as measurements. Figure 31 shows the fatigue load histogram of the side to side tower base moment at a wind speed of 15 m/s as an example. The TURBU results have been obtained through time domain simulations with the linearized wind turbine model driven by wind, wave and gravity loading. The stochastic wind and wave excitations are the inverse Fourier transforms of the helix-oriented wind spectra and the wave elevation spectrum, combined with the underwater wave strength fading functions as by Airy's theory.

Throughout this report, an equivalent load is used for fatigue analysis. The equivalent fatigue load concept has the advantage that the fatigue damage during a certain time span is expressed with a single value. The slope m of the SN-curve is used to transform the load bins from the fatigue counting method to an equivalent level at a predefined frequency.

$$R_{eq} = \left(\sum_{i=1}^{N_{bin}} \frac{R_i^m \cdot n_i}{n_{eq}} \right)^{\frac{1}{m}} \tag{19}$$

Thus, the equivalent 1Hz fatigue load is the single load amplitude with a frequency of 1Hz that represents the fatigue loading of the sum of all the different amplitudes during the considered time series. The equivalent number of load cycles for a 10min time series is $n_{eq1Hz} = 10 \cdot 60/1 = 600$. Another common specification is the equivalent 1P fatigue load, which is defined at the number of revolutions in the time interval. This report uses the equivalent 1Hz fatigue load.

The equivalent fatigue load to compare fatigue between components of the wind turbine (like tower and blades), because the actual damage in components is determined by the fatigue loads and material properties. The lifetime damage is also useful to determine the worst case scenarios for lifetime fatigue loading of the wind turbine (see section 4.3).

The calculation of fatigue damage during life time requires some extra steps, which are listed and explained below.

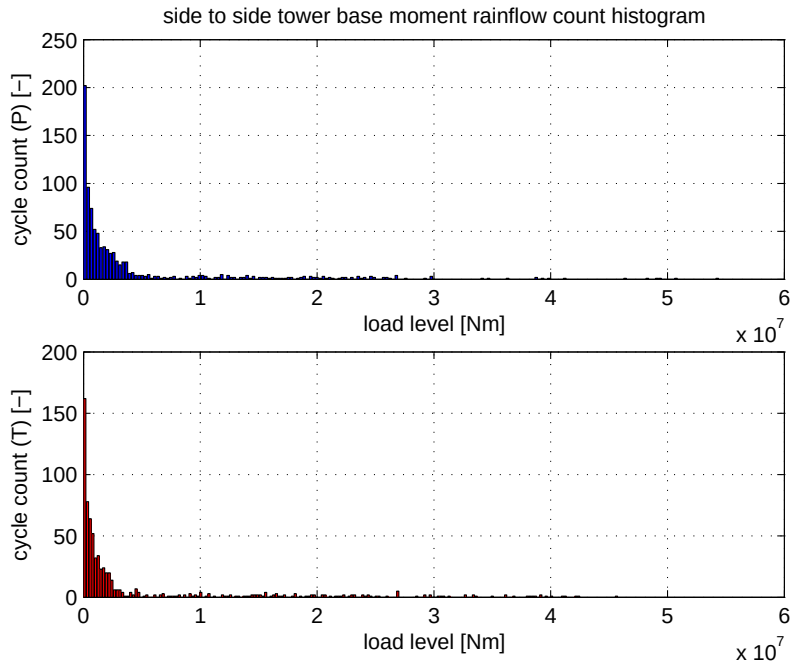

Figure 31: Fatigue load histogram of the side to side tower base moment at a wind speed of 15 m/s, as calculated with PHATAS (top) and TURBU (bottom).

1 determine the stress from the equivalent bending moment (20

$$S = \frac{M \cdot y}{I} \tag{20}$$

with M the bending moment in the cross section, I the area moment of inertia for a cylinder defined by $I = \frac{\pi}{64} \cdot (D_{out}^4 - D_{in}^4)$, D the cross section diameter and y the distance from the center to the edge of the cross section.

2 find the number of load cycles to failure for this stress level from the SN curve

3 apply Miner's rule (22) to determine the damage

The material properties are defined in the SN curve, which is determined with measurements on material samples and shows the number of cycles to failure (N) for a given stress amplitude (S). This research uses the SN curves for glass fiber composite (blades), high strength steel (blade flange and bolts) and structural steel (tower) shown in figure 32. These are simplified curves, only determined by slope m and one point K on the curve (21), which is fine for our purpose to demonstrate the method. More advanced analysis methods exist that use a sectioned SN curve or take mean stress level into account (Sutherland (2000)).

$$S_i^m \cdot N_i = K \tag{21}$$

with $K = S_{ref}^m \cdot n_{ref}$ the material constant at the reference loading.

To determine the total fatigue damage in parts of the wind turbine during its lifetime, the damage that occurred during each operating condition is summed according to the Palmgren-Miner rule (22). In theory, the component will not fail, when total damage D remains below unity. As simplified SN curves are used this is not exact science, but it can be used to compare fatigue damage in the blades and tower. With equation 21, the total fatigue damage is calculated as in

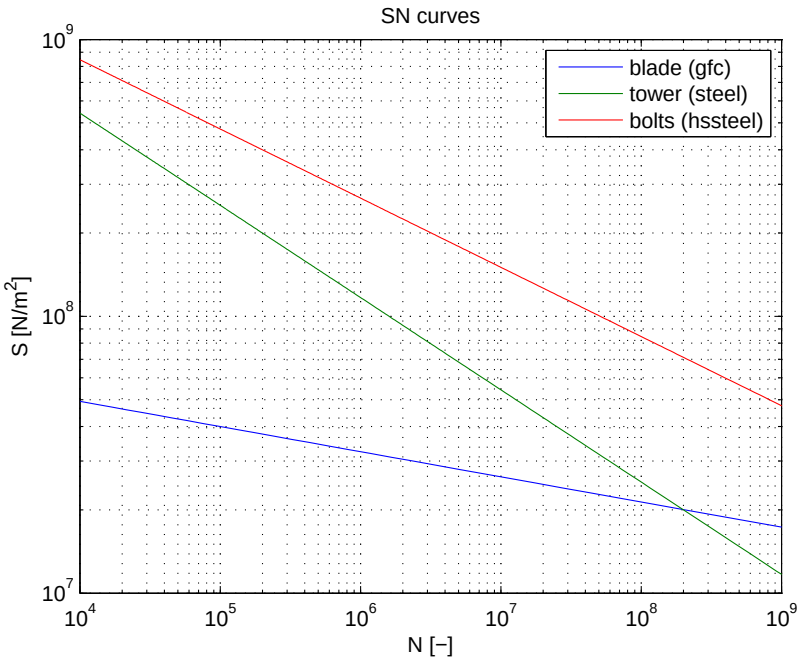

Figure 32: SN curves for the blades (glass fiber composite with $m = 11$), tower (structural steel with $m = 3$) and bolts (high strength steel with $m = 4$).

(22).

$$D = \sum_{i=1}^{k} \frac{n_i}{N_i}\bigg|_{S_i} = \sum_{i=1}^{k} \frac{n_i \cdot S_i^m}{K} \tag{22}$$

with n_i the number of cycles at given stress amplitude S_i, and N_i the number of cycles to failure for this amplitude.

This evaluation gives just a rough estimate, as the following assumptions are not valid in real life:
- simplified fatigue analysis (SN curve and loading)
- only production cases (100% availability)

Considerations when assessing fatigue are:

- number of time series
- length of the time records
- SN curve (slope, constants and limits)

In figure 33 and 34 the effect is shown of the number of series and the simulation time used to calculate the tower base fatigue load at a certain operating condition. The figures show both results with wind loading as with combined wind and wave loading. Due to the relatively slow wave dynamics, longer time series are expected to give better results in the case of combined loading. However, the difference between wind and added wave loading is small. In both cases, the values start to converge for 10min simulation and longer, which is the commonly used length for wind turbine fatigue calculation.

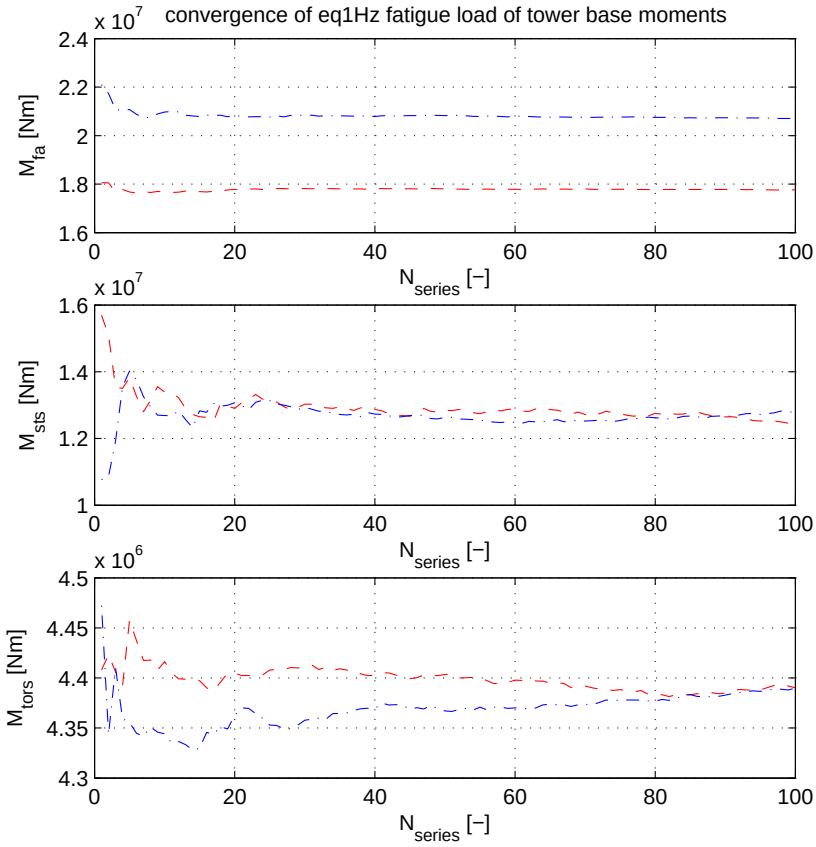

Figure 33: Average 1Hz equivalent fatigue load calculated from an increasing number of 10min time series. Both results are obtained with TURBU, but with wind (bo) and wave (ro) loading. The average of twenty time series is a good estimate of the actual fatigue load.

4.2 Life time fatigue damage

To determine the damage contribution of a sea state to the total life time fatigue, the steps from section 4.1 are performed using the calculated equivalent fatigue load. The sea states are measured as 3 hours average, while the equivalent 1Hz fatigue loads for each operating condition in the scatter diagram are calculated as the average of six 10min series. To determine the life time damage, the loads are extrapolated to life time operation by defining the number of load cycles as $n_i = (3 \cdot 60 \cdot 60) \cdot n_{o3oc}$, with n_{o3oc} the number of occurrence of the 3 hour operating condition (wind and sea state) during the life time. The following formula (23) summarizes the life time damage calculation.

$$D = \sum_{s=1}^{N_s} \frac{(3 \cdot 60 \cdot 60) \cdot n_{o3oc_s} \cdot S_{eq1Hz_s}^m}{K} \tag{23}$$

Table 8 shows the life time damage in the blade root, blade flange bolts and tower (during normal operating conditions, as assumed throughout this report). It is a simplified analysis (see 4.1), used to show the method and get an estimate of fatigue damage in different components. Only the blade root section and the tower base section are analyzed, instead of the whole component span.

Due to the combination of moderate loading and a relative strong relation between stress level and number of cycles to failure (flat SN curve), the blade fatigue damage during normal production

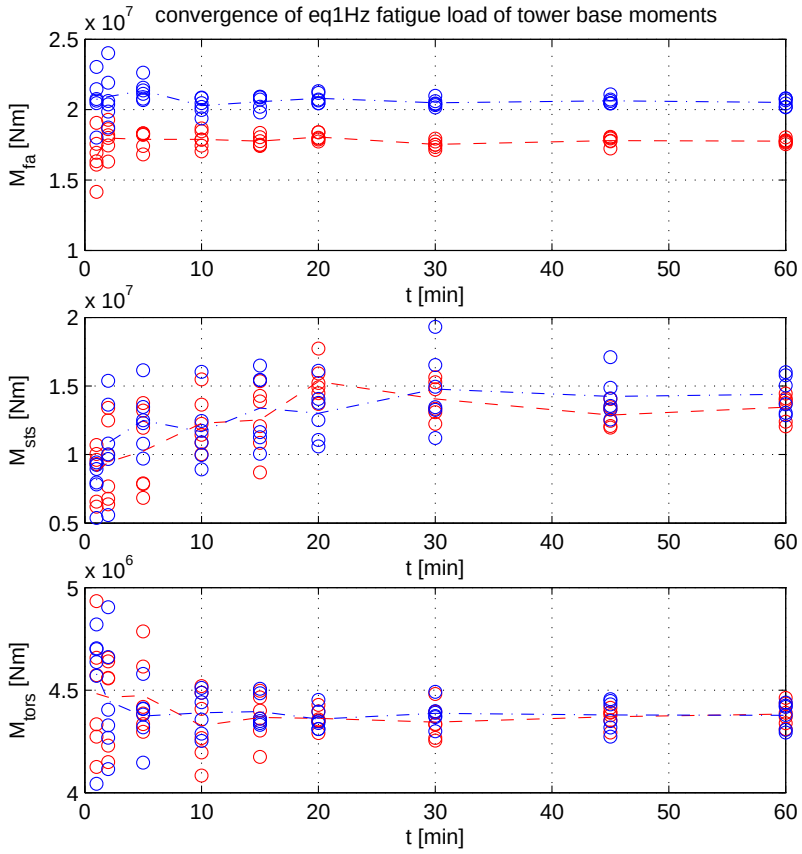

Figure 34: Average 1Hz equivalent fatigue load calculated from six time series with different record length. Both results are obtained with TURBU, but with wind (bo) and wave (ro) loading. The fatigue load starts to converge for time series of 10 minutes.

is minimal. However, fatigue of the steel bolts used to connect the blade to the hub should be analyzed for normal production. Also, the flat SN curve of the blade material could cause a high contribution to fatigue during ultimate load operating conditions such as extreme wind gusts or emergency shutdown. Unfortunately, these can not (yet) be analyzed with TURBU.

The tower fatigue damage is significant, considering the fact that only normal production is taken into account. However, ultimate load cases will have less effect on fatigue damage for steel components like the tower (steep SN curve) compared to composites.

Table 8: Fatigue damage during the wind turbine life time.

comp (mat)	load	D [-]
blade root (gfc)	B_{flap}	0.011
	B_{lead}	0.001
	B_{tors}	0.000
blade bolt (hs steel)	B_{flap}	0.359
	B_{lead}	0.325
	B_{tors}	0.000
tower (steel)	T_{fa}	0.514
	T_{sts}	0.504
	T_{tors}	0.001

4.3 Sea state selection

In this section, the full sea state scatter diagram is analyzed with TURBU. To speed up the calculation, some optimization can be applied on the load set, as described in E. Figure 35 shows cross sections of the equivalent 1Hz side to side tower base fatigue at selected wind speeds (V_{wind}) and angle between wind and waves ($\theta_{w\&w}$). Figure 36 shows the fatigue damage on the tower base for the same sections of the full scatter analysis as in figure 35.

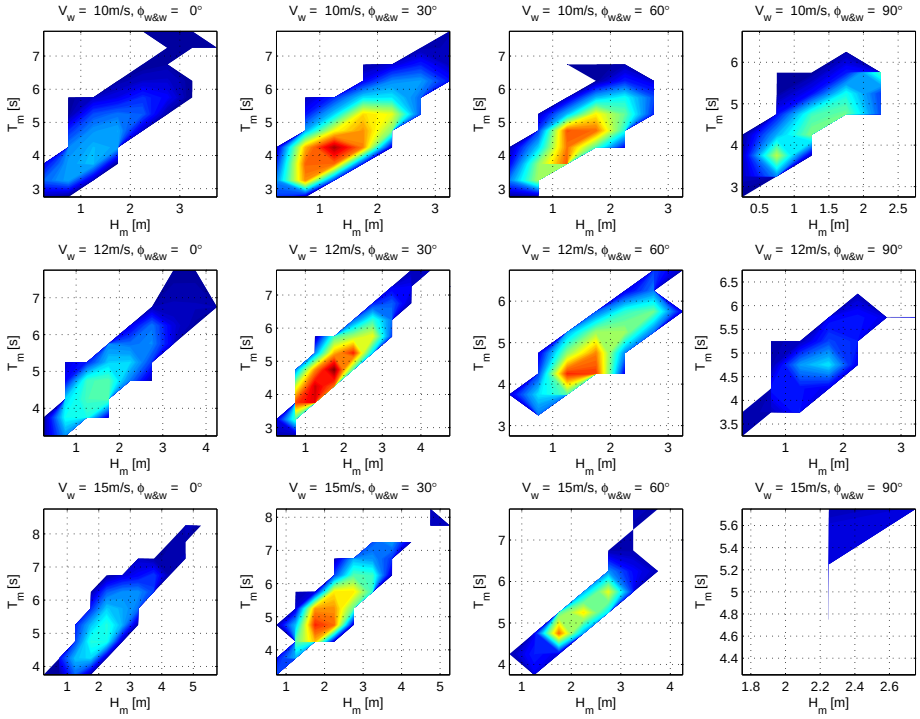

Figure 35: Equivalent 1Hz fatigue load calculated on the whole scatter for side to side tower bending. The rows of the plot matrix represent the angle between wind and wave direction ($\theta_{w\&w}$) and the columns different wind speeds (V_{wind}). Each plot then shows the equivalent 1Hz fatigue load (colored; b:low - r:high) at different sea states (wave height H_s, wave period T_p).

These plots are used to select the worst case scenarios, both for equivalent fatigue loading (M_{eq1Hz}) as well as contribution to damage (D_s) during life time (see table 9). This is a minimal set of load cases, used to demonstrate the method and compare the result with PHATAS. The scenarios are evaluated in the next section. The distribution of damage with number of load cases is shown in figure 37. The sea states are sorted for decreasing damage and plotted as cumulative sum, to show the potential of load case reduction.

Table 9: Worst case scenarios for fatigue during the wind turbine life time.

case	load	M_{eq1Hz} [Nm]	D_s [-]	V_{wind} [m/s]	H_m [m]	T_m [s]	$\phi_{w\&w}$ [deg]
wc1	B_{flap}	1.184e7		25	3.75	5.75	30
wc2	B_{flap}		1.423e-4	12	1.25	4.25	0
wc3	T_{sts}	5.877e7		13	3.25	5.75	90
wc4	T_{sts}		1.632e-3	10	1.75	4.75	60

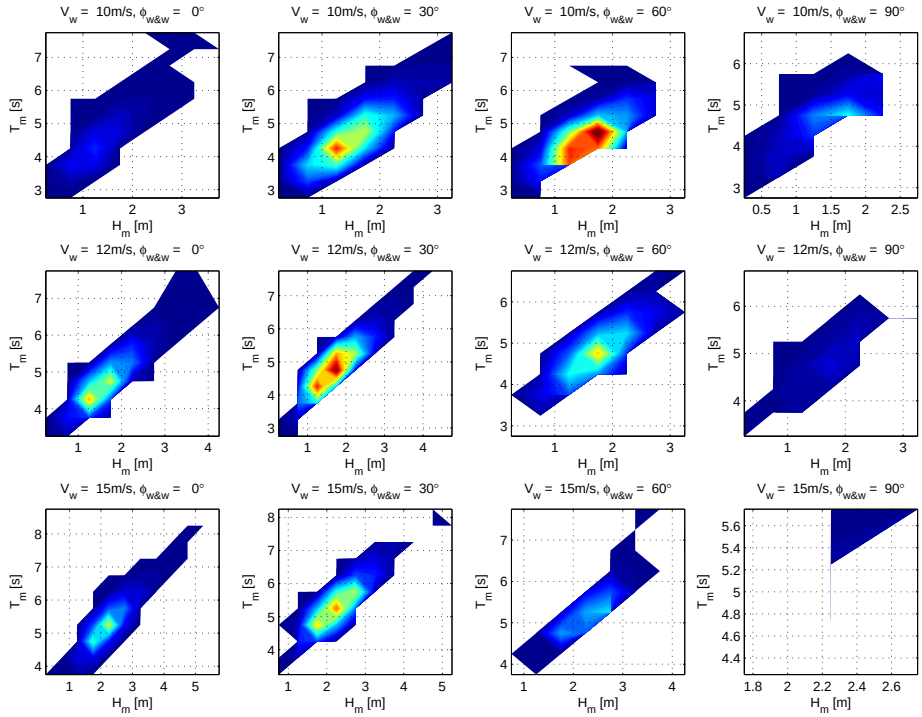

Figure 36: Tower damage from the side to side fatigue loading (for description see figure 35).

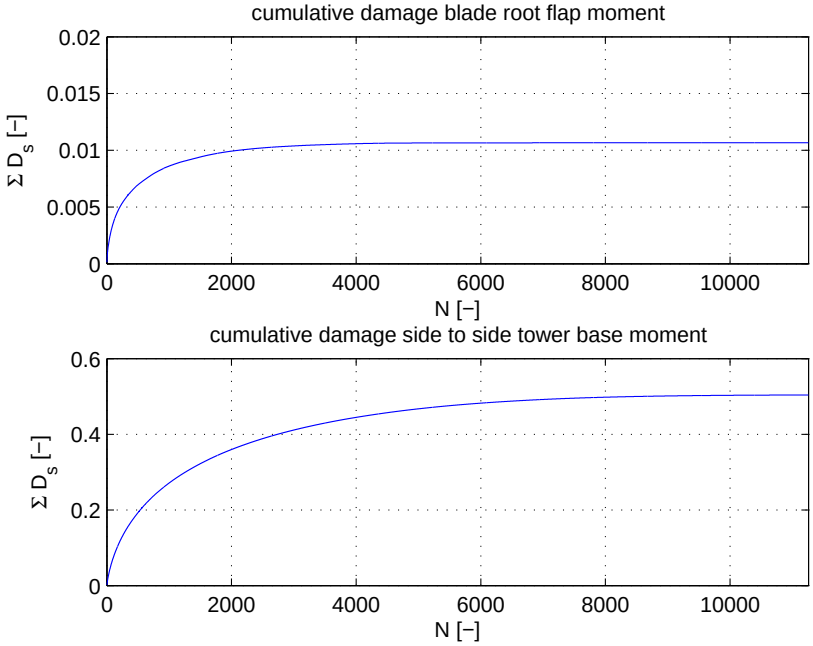

Figure 37: Cumulative sum of fatigue damage for the unique sea states.

4.4 Fatigue comparison between PHATAS and TURBU

In 2.4.5, fatigue calculated with PHATAS and TURBU is compared for the most occurring operating conditions. In this section the analysis is extended to different type of loading and some worst case scenarios as identified in section 4.3.

4.4.1 Wave loading

Figure 38 shows the effects of water (for depth d_{water} submerged support structure) and wave loading on the side to side tower base moment spectra, both for PHATAS and TURBU results.

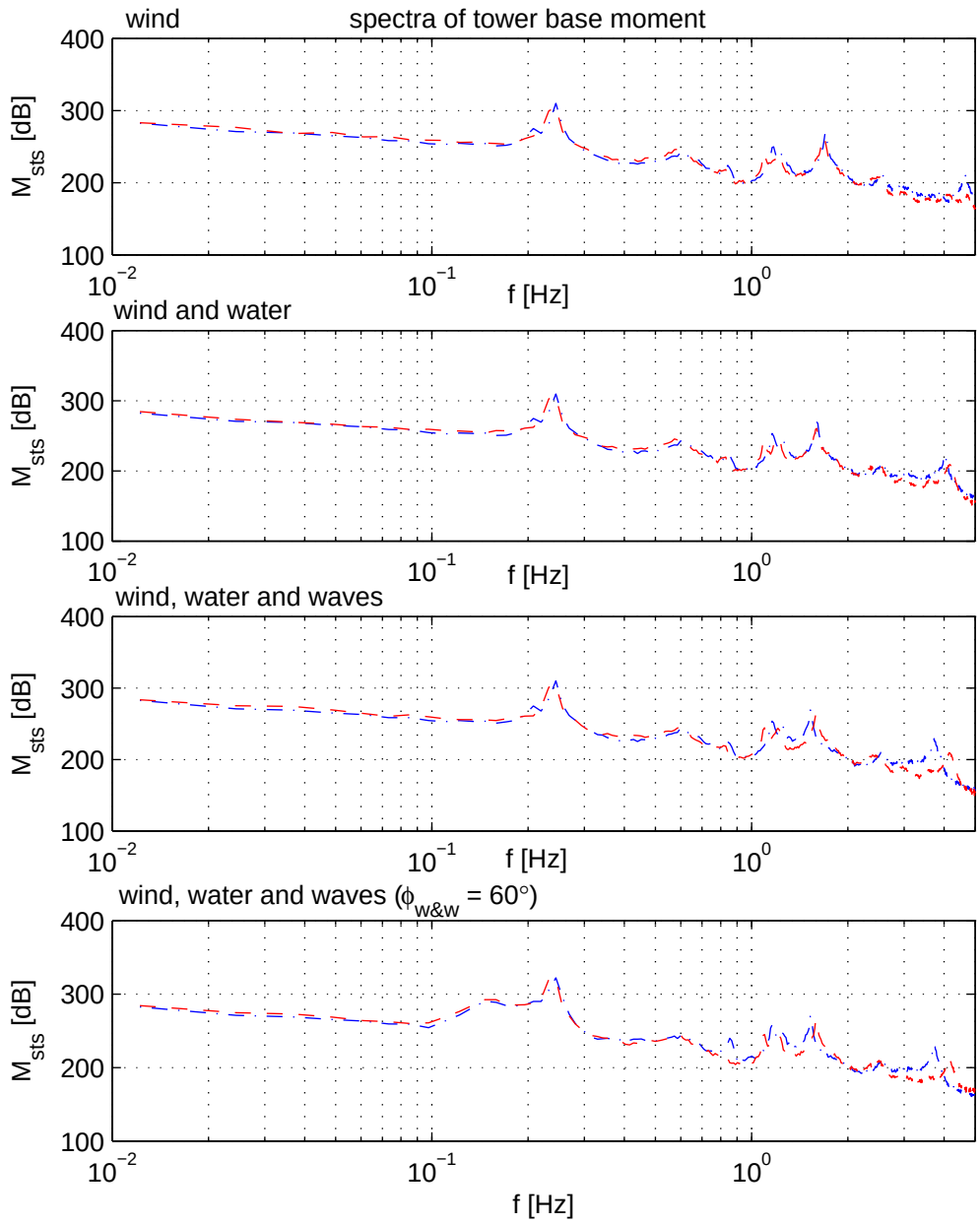

Figure 38: Spectra of the side to side tower base moment (vw=15m/s) calculated with PHATAS (b-.) and TURBU (r–) for different loading.

In table 10 and figure 39 the effect of the angle between wind and wave loading is investigated. The fore aft tower fatigue results from PHATAS and TURBU are similar, apart from the offset already observed in section 2.4.5. Both PHATAS and TURBU show an increase of the side to side tower fatigue load with angle (up to 90 degrees), but the absolute value differs. This is probably due to the linearization of the hydrodynamic loading, which should be improved with the new linearization method (see A).

Table 10: Side to side tower equivalent 1Hz fatigue for different angles between wind and wave loading.

		PHATAS		TURBU	
case	$\phi_{w\&w}$ [deg]	M_{eq1Hz} [Nm]	σ [Nm]	M_{eq1Hz} [Nm]	σ [Nm]
5	0	1.435e+007	2.274e+006	1.314e+007	1.492e+006
5	30	1.892e+007	4.126e+006	1.886e+007	4.932e+006
5	60	2.721e+007	5.823e+006	3.352e+007	2.112e+006
5	90	3.158e+007	5.851e+006	4.478e+007	5.986e+006
5	180	1.426e+007	3.333e+006	1.189e+007	9.454e+005

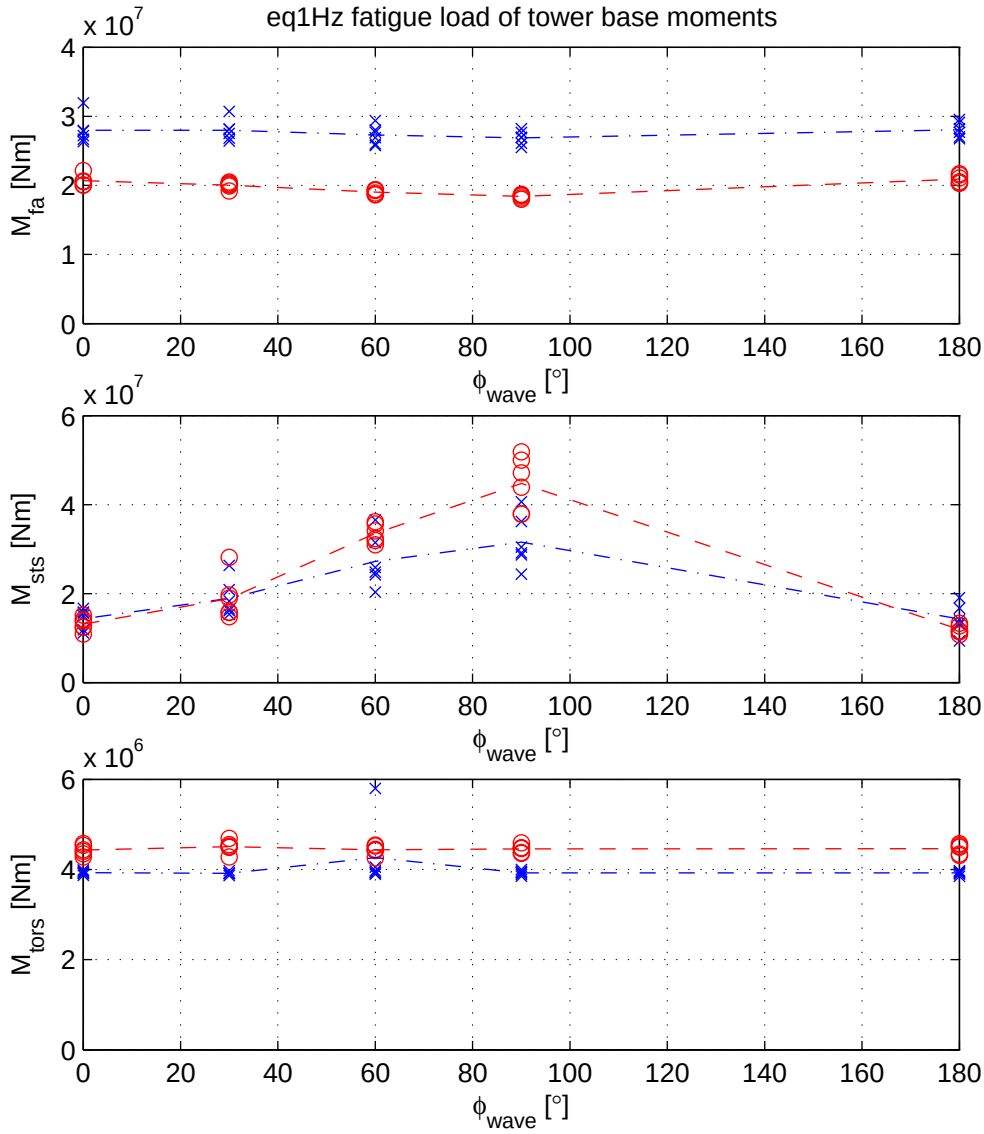

Figure 39: Influence of wave direction on the tower base fatigue calculated with PHATAS (bx) and TURBU (ro).

4.4.2 Worst case scenarios

Table 11 shows the equivalent 1Hz fatigue loads on the blade root and the tower base at the worst scenarios from 9. The blade fatigue difference at high wind speed (wc1) between TURBU and PHATAS is within a few percent. The large difference around rated (wc2) is caused by the pitch angle peak shaving setting. The side to side tower base fatigue does not match very good. For

both wc3 and wc4, the wave direction is oblique to the wind. Figure 39 already showed large differences between TURBU and PHATAS for increasing angle between wind and waves. This could be caused by the linearization of the hydrodynamic loading.

Table 11: Comparison of the TURBU and PHATAS fatigue results at the worst case scenarios.

		PHATAS		TURBU	
case	load	M_{eq1Hz} [Nm]	σ [Nm]	M_{eq1Hz} [Nm]	σ [Nm]
wc1	B_{flap}	1.114e+007	4.960e+005	1.184e+007	1.004e+006
wc2	B_{flap}	7.705e+006	3.115e+005	1.037e+007	6.967e+005
wc3	T_{sts}	4.275e+007	8.671e+006	5.877e+007	8.535e+006
wc4	T_{sts}	2.879e+007	6.673e+006	3.717e+007	6.665e+006

5 Discussion

This chapter summarizes the conclusions drawn from the results presented in previous chapters. Also some recommendations are given for further research.

5.1 Conclusions

model comparison

The working point equilibrium derived with PHATAS and TURBU shows good overall resemblance across the whole operating range. Both the blade pitch angle obtained from the linearized controller, as from the automatic search routine in TURBU differ from the required pitch angle for rated power. This is solved by specifying the angle by hand. The tower base fore aft bending moment differs with a constant offset for all operating points. A difference in blade torsion was discovered from the model comparison, but solved during the project. The reversed aerodynamic moment coefficient caused twice the aerodynamic moment on the blade (and a high torsion deformation). The resulting difference in aeroelastic behaviour stresses the importance of taking torsion into account for large blades.

The power spectra of blade root and tower base moments show very similar dynamic behavior of the PHATAS and TURBU model. An underestimation in blade root flap moment from TURBU by a factor 3 at low frequencies (<0.1Hz) is observed, which is at least partly due to linearization. As expected, this also shows in the fore aft tower base bending moment. The foundation (model) has big impact on the tower dynamics. The different foundation modelling approach in PHATAS and TURBU (elasticity versus stiffness matrix) can cause different results, for instance with coupling between rotation and translation. In this project, a foundation model with only angular stiffness is used (both PHATAS and TURBU).

As a first comparison, blade root and tower base fatigue is analysed for a selection of operating conditions. Blade results match very good, but there are some differences in the tower fatigue. In fore aft direction above rated wind speed, the fatigue calculated with TURBU is lower than PHATAS. Side to side tower fatigue from TURBU increases linearly with wind speed, while results from PHATAS flatten around rated wind speed.

design methods

During the design phase, a complete characterization of the dynamics and loading of the wind turbine is essential. The proposed method uses TURBU to determine a modified Campbell diagram based on loading. It is fast enough to be used for design iteration. The applied cases demonstrate the use and added value of this approach.

Optimization of wind turbine design is possible with TURBU. The calculation speed allows the designer do conduct a detailed parameter variation for the whole operating range within minutes. Care should be taken when defining the driver for optimization (cost function); an optimal solution for loading can be the worst cost wise. Again some example cases show the application of TURBU in this field.

fatigue and load case reduction

For the analysed test case (normal production at 15m/s wind), the commonly used set of 6 10min time series showed to be adequate for tower fatigue calculation.

Due to the relative strong relation between stress level and number of cycles to failure (flat SN curve) of glass fiber composite combined with moderate loading, normal production does not really contribute to fatigue damage in the blade (root) itself. The fatigue of the steel bolts used to connect the blade to the hub should be analyzed for normal production. Also, the flat SN curve of the blade material could cause a high contribution to fatigue during ultimate load operating conditions such as extreme wind gusts or emergency shutdown. Unfortunately, these can not

(yet) be analyzed with TURBU.

For the support structure, fatigue during normal production is design driving. As expected, wave loading has most impact on the fatigue of the support structure. The wind loading dominates blade fatigue. The angle between wind and waves has a significant influence on fatigue of the support structure; increasing angle decreases the fore aft and almost doubles the side to side tower base fatigue for the test case. These oblique load cases show large differences between TURBU and PHATAS, which is probably due to the linearization of the hydrodynamic loading.

The results of the proposed method for load case reduction are promising. The calculation speed of TURBU allows the designer to analyse the full sea state scatter diagram to select the sea states contributing to fatigue. However, there are still some differences between the PHATAS and TURBU results to be further investigated.

5.2 Recommendations

Some recommendations for further research on the load case reduction strategy are listed below.

- investigate the cause of the difference in the results for tower bending
  The results from TURBU for tower bending differ from those obtained with PHATAS, for both static and fatigue loads. For the static situation, this is not caused by aerodynamic loading (the axial thrust on the rotor shows a good match). As the tower and nacelle combination (top mass on a pole) is a destabilizing system, strong interaction exist between tower base loading and tower top deformation.

- extend the fatigue calculation in TURBU
  The current fatigue analysis in TURBU uses a very simplified SN curve. Other programs can be used to apply more advanced methods, but for these load set calculations it would be convenient to also include it in TURBU.

- compare calculated fatigue with measurements
  Although PHATAS is a validated wind turbine analysis tool, it is essential to compare the results of the fatigue analysis to measurements on a real wind turbine, focusing on fatigue load cases.

- compare fatigue results from scatter analysis to distribution approach
  Not every offshore site has available such extensive measurement data as used in this project. It would be very interesting to compare the fatigue results from a full scatter analysis with results using (probability) distributions for the sea states. This could then be used to develop a method for selecting sea states contributing to fatigue from smaller measurement sets.

Bibliography

Arena, F. and V. Nava (2008): *On linearization of Morison force given by high three-dimensional sea wave groups*. Probabilistic Engineering Mechanics, 23(2-3):104 – 113.

Balmer, L. (1997): *Signals and systems*. Prentice Hall, second edition.

Borgman, L.E. (1967a): *Random hydrodynamic forces on objects*. Annals of mathematical statistics, 38(1):37 – 51.

Borgman, L.E. (1967b): *Spectral analysis of ocean wave forces on piling*. Journal of the waterways and harbors division, 93:129–156.

Coleman, R.P. and A.M. Feingold (1958): *Theory of self-excited mechanical oscillations of helicopter rotors with hinged blades*. Report NACA-TN-3844; NACA-TR-1351, NASA, Langley Research Center.

Dowec (2003): *http://www.ecn.nl/units/wind/rd-programme/aerodynamics/projects/dowec/*.

Eecen, P. (2003): *Wind waves; Forces due to waves on offshore wind turbines*. Report ECN-C–03-097, ECN.

van Engelen, T. (2007): *Control design based on aero-hydro-servo-elastic linear models from TURBU (ECN)*. Proceedings of the European Wind Energy Conference Milan. pages 68–81.

van Engelen, T. and H. Braam (2004): *TURBU Offshore; Computer program for frequency domain analysis of horizontal axis offshore wind turbines - Implementation*. Report ECN-C–04-079, ECN.

Gere, J. and S. Timoshenko (1999): *Mechanics of materials*. Stanley Tornes, fourth edition.

Ghosh, P.K. (1983): *The prediction of hydrodynamic viscous damping of offshore structures in waves and current by the stochastic linearization method*. Master's thesis, Massachustts Institute of Technology (MIT).

Henderson, A. (2003): *Design methods for offshore wind turbines at exposed sites (OWTES)*. Report, DuWind.

Henderson, A. and M. Zaaijer (2008): *Hydrodynamic loading on offshore wind turbine support structures*. Engineering integrity, vol. 25, pag. 24-31.

Kensche, C. (2004): *Fatigue of composites for wind turbines*. Proceedings of the 3rd international conference on fatigue of composites.

Kooijman, H., C. Lindenburg, D. Winkelaar and E. van der Hooft (2003): *Aero-elastic modelling of the Dowec 6MW predesign in PHATAS*. Report ECN-CX–01-135, ECN.

Kuhn, M. (2001): *Dynamics and design optimization of offshore wind energy conversion systems*. Ph.D. thesis, Delft University of Technology.

Lindenburg, C. (2002): *Aeroelastic modelling of the LMH64-5 blade*. Report DOWEC-02-KL-083/0, ECN.

Lindenburg, C. (2005): *PHATAS release 'APR-2005' user's manual*. Report ECN-I–05-005, ECN.

Madsen, P. (1990): *Recommended practices for wind turbine testing and evaluation; 3. FATIGUE LOADS*. International Energy Agency, 2 edition.

Mandell, J., R. Reed and D. Samborsky (1992): *Fatigue of fiberglass wind turbine blade materials*. Report, Montana State University.

Morison, J.R., M.P. O'Brien, J.W. Johnson and S.A. Schaaf (1950): *The force exerted by surface wave on piles*. Petroleum Transactions of the American Institute of Mining Engineers, 189:149 – 154.

Peters, H. and H. Boonstra (1988): *Fatigue loading on a single pile platform due to combined action of waves and currents*. Behavior of offshore structures. pages 1015–1035.

Ragan, P. and L. Manuel (2007): *Comparing estimates of wind turbine fatigue loads using time-domain and spectral methods*. Wind engineering, vol. 31, no. 2, pag. 83-99.

Rehal, R. (2003): *Foundation design monopile*. Report, Ballast Nedam.

Roberts, J.B. and P.D. Spanos (1990): *Random Vibration and Statistical Linearization.* Wiley.

Rossetti, M., M. Guadayoi, O. Goula and J. Prats (2008): *Wind turbine dynamics validation and controller optimization*. Proceedings of the European Wind Energy Conference Brussels. pages 27–29.

RWS (2009): *North Sea measurements*. http://www.golfklimaat.nl/.

Sarpkaya, T. and I. Isaacson (1981): *Mechanics of wave forces on offshore structures*. Van Nostrand Reinhold Company Inc.

Sherratt, F., N. Bishop and T. Dirlik (2005): *Predicting fatigue life from frequency-domain data: current methods*. Engineering integrity society.

Spanos, P.T.D. and T.W. Chen (1981): *Random response to flow-induced forces*. Journal of the Engineering Mechanics Division, 107(6):1173 – 1190.

Sutherland, H. (2000): *A summary of the fatigue properties of wind turbine material*. Wind energy, vol. 3, pag. 1-34.

van der Tempel, J. (2006): *Design of support structures for offshore wind turbines*. Ph.D. thesis, Delft University of Technology.

Westra, C. and H. Beurskens (2009): *Vandaag bouwen aan energie van morgen*. Booklet.

Winkelaar, D. (1992): *SWIFT program for three-dimensional wind simulation*. Report ECN-R–92-013, ECN.

Wolfram, J.P. (1999): *On alternative approaches to linearization and Morison's equation for wave forces*. Proceedings Royal Society, 455:2957 – 2974.

Wouters, D. and T. van Engelen (2008): *Modern wind turbine controller design*. Proceedings of the global wind power conference 2008, China.

Zaaijer, M. (2001): *Properties of offshore support structures for large scale wind turbines*. Proceedings of the Offshore Wind Energy Conference.

A Linearization of the Morison equation

This chapter gives a concise description of the different linearizations of the Morison equation. First different linearization models found in literature are discussed, starting with the condition of no water current (U = 0 m/s). Next the implementation of a (linearized) Morison equation in TURBU including the effect of the current velocity and the structural displacements.

A.1 Morison equation

In offshore engineering the wave loads on a slender body are modelled using the Morison equation, see Morison et al. (1950). The original Morison equation was developed for an immovable cylinder with its largest cross sectional dimension $\frac{1}{20}$ of the wave length λ.

$$Q(t) = \rho_w C_m \frac{\pi}{4} D^2 \ddot{u}(t) + \frac{1}{2} \rho_w C_D D |\dot{u}(t)| \dot{u}(t) \tag{24}$$

Here C_m is the mass force coefficient, C_D is the drag force coefficient, D the cylinder diameter,ρ_w the water density, $\dot{u}$ and $\ddot{u}$ the wave velocity and wave acceleration. To account for the effect of the structural movement on the wave loading the Morison equation is modified

$$F(t) = \rho_w \left(C_m - 1\right) \frac{\pi}{4} D^2 \left(\ddot{v}(t) - \ddot{x}(t)\right) + \rho_w \frac{\pi}{4} D^2 \ddot{v}(t) + \frac{1}{2} \rho_w C_D D |\dot{v}(t) - \dot{x}(t)| (\dot{v}(t) - \dot{x}(t)) \tag{25}$$

With $\dot{x}$ and $\ddot{x}$ the structural motions and $\dot{v}$ the water loading of the mean current velocity U and the wave velocity $\dot{u}$

$$\dot{v} = U + \dot{u} \tag{26}$$

Detailed information about the Morison equation and the selection of the coefficients C_D and C_m can be found in Sarpkaya and Isaacson (1981). To apply the Morison equation in linear frequency domain models like TURBU the nonlinear drag term has to be linearized.

A.2 Literature

A.2.1 Linearization without current

The linearization of the Morison equation is based on the equivalent linearization technique. Borgman (1967b) was one of the first to apply this technique for the linearization of the drag term in the Morison equation. Nowadays this linearization of the Morison equation is often named after Borgman , see Arena and Nava (2008) and Wolfram (1999).

Borgman expresses the Morison equation by its autocorrelation function $R_F(\tau)$, see Borgman (1967a).

$$R_F(\tau) = K_d^2 \sigma_{\dot{u}}^4 G(R_{\dot{u}}(\tau)/\sigma_{\dot{u}}^2) + K_i^2 R_{\ddot{u}}(\tau) \tag{27}$$

where

$$K_d = \frac{1}{2}\rho_w D C_D$$
$$K_i = \frac{1}{4}\rho_w \pi D^2 C_m$$

The function $G(\rho)$ in equation 27is a function of correlation coefficient ρ

$$G(\rho) = \frac{\left[(4\rho^2+2)\sin\rho^{-1} + 6\rho\sqrt{1-\rho}\right]}{\pi} \tag{28}$$

Approximating $G(\rho)$ by a power series in ρ gives:

$$G(\rho) = \frac{1}{\pi}\left[8\rho + \frac{4}{3}\rho^3 + \frac{1}{15}\rho^5 + \ldots\right] \tag{29}$$

For ρ = 1 taking only the first term the difference with $G(\rho)$, equation 28 is about 15%. Including the second term the difference with $G(\rho)$ is reduced to 1%. The linearized approximation of the autocorrelation function, taking only the first term of $G(\rho)$, gives the auto correlation function:

$$R_F(\tau) = \frac{8}{\pi}K_d^2\sigma_{\dot{u}}^2 R_{\dot{u}}(\tau) + K_i^2 R_{\ddot{u}}(\tau) \tag{30}$$

This linearization of the autocorrelation function is equivalent to linearizing the Morison equation:

$$Q_{lin} = \sqrt{\frac{8}{\pi}}K_d\sigma_{\dot{u}}\dot{u} + K_i\ddot{u} \tag{31}$$

Another approach for the equivalent linearization method is to handle the non linearities in stiffness and damping in the equation of motion. See Roberts and Spanos (1990). The A general equation of motion used is

$$\ddot{x} + g(x,\dot{x}) = f(t) \tag{32}$$

with $g(x,\dot{x})$ a non linear function of x and $\dot{x}$.

The first step is to define an equivalent linear equation:

$$\ddot{x} + \beta_e\dot{x} + k_e x = f(t) \tag{33}$$

The difference ϵ between the nonlinear and linear equation is

$$\epsilon = g(x, \dot{x}) - \beta_e \dot{x} + k_e x \tag{34}$$

The difference ϵ is squared and mean is determined. Next the mean square difference is minimized by taking the derivatives with respect to the linearized coefficients β_e and k_e. To find the minimum the derivatives are set to zero.

$$\frac{\partial \mathrm{E}\{\epsilon^2\}}{\partial \beta_e} = \frac{\partial \mathrm{E}\{\epsilon^2\}}{\partial k_e} = 0 \tag{35}$$

This gives

$$\beta_e = \frac{\mathrm{E}\{g(x, \dot{x})\dot{x}\}}{\mathrm{E}\{\dot{x}^2\}} \tag{36}$$

$$k_e = \frac{\mathrm{E}\{g(x, \dot{x})x\}}{\mathrm{E}\{x^2\}} \tag{37}$$

$$\tag{38}$$

Wolfram (1999) minimizes for the condition without current the mean square of the difference between the non linear Morison equation and the linear Morison equation. The non linear Morison equation is:

$$Q = K_d |\dot{u}| \dot{u} + K_i \ddot{u} \tag{39}$$

and the linear Morison equation is defined as:

$$Q_{lin} = \beta_e \dot{u} + K_i \ddot{u} \tag{40}$$

The mean square of the difference ϵ between Q and Q_{lin} is determined and minimized for the term β_e

$$\frac{\partial \mathrm{E}\{\epsilon^2\}}{\partial \beta_e} = -2\mathrm{E}\{K_d \dot{u}^2 |\dot{u}| - \beta_e \dot{u}^2\} = 0 \tag{41}$$

This gives the same linearization result as Borgman for $\dot{u}$ being a zero mean Gaussian random variable.

$$\beta_e = K_d \frac{\mathrm{E}\{\dot{u}^2 |\dot{u}|\}}{\mathrm{E}\{\dot{u}^2\}} = K_d \frac{\sqrt{\frac{8}{\pi}} \sigma_{\dot{u}}^3}{\sigma_{\dot{u}}^2} \tag{42}$$

A.2.2 Linearization with current and structural displacement

Spanos and Chen (1981) and Ghosh (1983) extended the linearization to the modified Morison equation 25 with current and structural displacement included.

The Morison equation contains only a non linear damping part that has to be linearized

$$F_D(r) = \frac{1}{2}\rho C_D D(r+U)|r+U| \tag{43}$$

where r is the relative fluid-structure velocity

$$r = \dot{u} - \dot{x} \tag{44}$$

Assuming the linear damping term to be β_e, the difference ϵ is

$$\epsilon = F_D(r) - \beta_e r \tag{45}$$

According to equation 36 this gives

$$\beta_e = \frac{\mathrm{E}\{F_D(r)r\}}{\mathrm{E}\{r^2\}} \tag{46}$$

The linearized damping coefficient β_e is now for a non zero mean random variable $r+U$

$$\beta_e = \frac{1}{2}\rho C_D D\mathrm{E}\{2|r+U|\} = \frac{1}{2}\rho C_D D\left[\sqrt{\frac{8}{\pi}}\sigma_r \exp\left(-\frac{U^2}{2\sigma_r^2}\right) + 2\mathrm{Erf}\left(\frac{U}{\sqrt{2}\sigma_r}\right)\right] \tag{47}$$

Ghosh (1983) gives an detailed account of the different steps to get β_e.

A.3 TURBU implementation of linearized Morison equation

A.3.1 TURBU linearized Morison equation

In this project the following implementation of the linearized Morison equation in TURBU was used. See van Engelen and Braam (2004) Under the assumption that the relative velocity r is small compared to the current velocity U the squared velocity in the drag term of the Morison equation can be written as

$$(U+r)|U+r| = r|r| + 2Ur \tag{48}$$

Inserting the Borgman linearization, $\sqrt{\frac{8}{\pi}}\sigma$, in $r|r|$ gives the following expression for the lin-

earized Morison equation:

$$F(t) = \frac{1}{2}\rho C_D D\left(\sqrt{\frac{8}{\pi}}\sigma_{\dot{u}} + 2\cdot U\right)(\dot{u}-\dot{x}) + \rho C_m \frac{\pi}{4}D^2\ddot{u} - \rho\left(C_m - 1\right)\frac{\pi}{4}D^2\ddot{x} \qquad (49)$$

A.3.2 New linearized Morison equation in TURBU

Meanwhile a new linearization procedure is developed for TURBU. The loads in both fore aft and side to side direction are considered simultaneously. The description below is taken from the user manual of TURBU (van Engelen (2009) draft).

The linearization of the hydrodynamic viscous forces is quite cumbersome if the water current does not exceed the horizontal wave speed or tower speeds by far. In the sequel, the visco-hydrodynamic load expressions are normalized with $C_{\mathrm{V}}(z)\cdot\frac{1}{2}\rho_{\mathrm{w}}D(z)$. The normalised force coordinates $q_{\mathrm{fa,vn}}$ and $q_{\mathrm{sd,vn}}$ are expressed in the relative water velocity coordinates U_{fa} and U_{sd}, and the size $\hat{q}_{\mathrm{vn}}(z)$ of the normalised viscous force ($\mathrm{c}_{cw}, \mathrm{c}_c, \mathrm{c}_w, \mathrm{s}_c, \mathrm{s}_w$ short forms of $\cos(\phi_{\mathrm{c}} - \phi_{\mathrm{w}}), \cos\phi_{\mathrm{c}}, \cos\phi_{\mathrm{w}}, \sin\phi_{\mathrm{c}}, \sin\phi_{\mathrm{w}}$,):

$$\begin{aligned} q_{\mathrm{fa,vn}}(z) &= \sqrt{\hat{q}_{\mathrm{vn}}(z)}\cdot U_{\mathrm{fa}}(z), \quad \text{with } U_{\mathrm{fa}}(z) = \mathrm{c}_c\cdot\bar{w}(z) + \mathrm{c}_w\cdot\delta w(z) - v_{\mathrm{fa}}(z) \\ q_{\mathrm{sd,vn}}(z) &= \sqrt{\hat{q}_{\mathrm{vn}}(z)}\cdot U_{\mathrm{sd}}(z), \quad \text{with } U_{\mathrm{sd}}(z) = \mathrm{s}_c\cdot\bar{w}(z) + \mathrm{s}_w\cdot\delta w(z) - v_{\mathrm{sd}}(z) \end{aligned} \qquad (50)$$

The size $\hat{q}_{\mathrm{vn}}$ of the normalised hydrodynamic viscous force vector is given by:

$$\begin{aligned} \hat{q}_{\mathrm{vn}}(z) &= U_{\mathrm{fa}}(z)^2 + U_{\mathrm{sd}}(z)^2 \\ &= \bar{w}(z)^2 + 2\mathrm{c}_{cw}\cdot\bar{w}(z)\cdot\delta w(z) - 2\mathrm{c}_c\cdot\bar{w}(z)\cdot v_{\mathrm{fa}}(z) - 2\mathrm{s}_c\cdot\bar{w}(z)\cdot v_{\mathrm{sd}}(z) \\ &\quad + \delta w(z)^2 + v_{\mathrm{fa}}(z)^2 + v_{\mathrm{sd}}(z)^2 - 2c_{\mathrm{w}}\cdot\delta w(z)\cdot v_{\mathrm{fa}}(z) - 2\mathrm{s}_w\cdot\delta w(z)\cdot v_{\mathrm{sd}}(z) \end{aligned} \qquad (51)$$

The pursued expressions for the normalized visco-hydrodynamic force coordinates in foreaft and sideward direction include gains from variations in the horizontal wave speed and the foreaft and sideward tower speed, denoted as per:

$$\begin{aligned} \delta q_{\mathrm{fa,vn}}(z) &= K_{\mathrm{fw}}(z)\cdot\delta w(z) + K_{\mathrm{ff}}(z)\cdot\delta v_{\mathrm{fa}}(z) + K_{\mathrm{fs}}(z)\cdot\delta v_{\mathrm{sd}}(z) \\ \delta q_{\mathrm{sd,vn}}(z) &= K_{\mathrm{sw}}(z)\cdot\delta w(z) + K_{\mathrm{sf}}(z)\cdot\delta v_{\mathrm{fa}}(z) + K_{\mathrm{ss}}(z)\cdot\delta v_{\mathrm{sd}}(z) \end{aligned} \qquad (52)$$

If the water current $\bar{w}$ is much larger than the variations δw, δv_{fa} and δv_{sd} then the gains are simply obtained from basic linearisation of the expressions for $\sqrt{\hat{q}_{\mathrm{vn}}}$, U_{fa} and U_{sd} by setting δw, δv_{fa} and δv_{sd} equal to zero in the partial derivatives of these expressions.

However, if $\bar{w}$ is of similar size as (the standard deviation of) δw, δv_{fa} and δv_{sd} then the determination of the gains is more complicated. The general expressions for the unlinearized viscous force variations are:

$$\begin{aligned} \delta q_{\mathrm{fa,vn}}(z) &= \sqrt{\hat{q}_{\mathrm{vn}}(z)}\cdot U_{\mathrm{fa}}(z) - \overline{\sqrt{\hat{q}_{\mathrm{vn}}(z)}\cdot U_{\mathrm{fa}}(z)} \\ \delta q_{\mathrm{sd,vn}}(z) &= \sqrt{\hat{q}_{\mathrm{vn}}(z)}\cdot U_{\mathrm{sd}}(z) - \overline{\sqrt{\hat{q}_{\mathrm{vn}}(z)}\cdot U_{\mathrm{sd}}(z)} \end{aligned} \qquad (53)$$

which can be rewritten as:

$$\begin{aligned}
\delta q_{\mathrm{fa,vn}}(z) &= \sqrt{\bar{\hat{q}}_{\mathrm{vn}}(z)}\cdot\delta U_{\mathrm{fa}}(z) + \delta\sqrt{\hat{q}_{\mathrm{vn}}(z)}\cdot\bar{U}_{\mathrm{fa}}(z) + \delta\sqrt{\hat{q}_{\mathrm{vn}}(z)}\cdot\delta U_{\mathrm{fa}}(z) \\
&\quad + \sqrt{\bar{\hat{q}}_{\mathrm{vn}}(z)}\cdot\bar{U}_{\mathrm{fa}}(z) - \overline{\sqrt{\hat{q}_{\mathrm{vn}}(z)}\cdot U_{\mathrm{fa}}(z)}] \\
\delta q_{\mathrm{sd,vn}}(z) &= \sqrt{\bar{\hat{q}}_{\mathrm{vn}}(z)}\cdot\delta U_{\mathrm{sd}}(z) + \delta\sqrt{\hat{q}_{\mathrm{vn}}(z)}\cdot\bar{U}_{\mathrm{sd}}(z) + \delta\sqrt{\hat{q}_{\mathrm{vn}}(z)}\cdot\delta U_{\mathrm{sd}}(z) \\
&\quad + \sqrt{\bar{\hat{q}}_{\mathrm{vn}}(z)}\cdot\bar{U}_{\mathrm{sd}}(z) - \overline{\sqrt{\hat{q}_{\mathrm{vn}}(z)}\cdot U_{\mathrm{sd}}(z)}]
\end{aligned} \tag{54}$$

It is clear that the 4^{th} and 5^{th} term are equal and thus cancel, since the hydrodynamic load variations do not affect the mean hydrodynamic load level. If the water current $\bar{w}$ is very small, then the intensity of the visco-hydrodynamic load variations will exceed [by far] the time-average value based on $\bar{w}$, obtained under the assumption of zero wave and tower velocity. In that case it is common practice to use an *effective* value $\sqrt{\tilde{\hat{q}}_{\mathrm{vn}}(z)}$ instead of mean value $\sqrt{\bar{\hat{q}}_{\mathrm{vn}}(z)}$ as (direct) influence factor for the relative water speed variations δU_{fa} and δU_{sd}; this effective value depends on the intensity of the variations. This also holds for the parameterization of the influence of U_{fa} and U_{sd} through the variation $\delta\sqrt{\hat{q}_{\mathrm{vn}}(z)}$ of the load vector size; the carrying through of said intensity in the second order terms $\delta\sqrt{\hat{q}_{\mathrm{vn}}(z)}\cdot\delta U_{\mathrm{fa}}(z)$ and $\delta\sqrt{\hat{q}_{\mathrm{vn}}(z)}\cdot\delta U_{\mathrm{sd}}(z)$ even yields additional influence factors for the wave and tower speed variations[1]. The expressions that set up the point of departure for the determination of the gains in small water currents then become:

$$\begin{aligned}
\delta q_{\mathrm{fa,vn}}(z) &= \sqrt{\tilde{\hat{q}}_{\mathrm{vn}}(z)}\cdot\delta U_{\mathrm{fa}}(z) + \tfrac{1}{2}\delta\hat{q}_{\mathrm{vn}}(z)\cdot U_{\mathrm{fa}}(z)/\sqrt{\tilde{\hat{q}}_{\mathrm{vn}}(z)} \\
\delta q_{\mathrm{sd,vn}}(z) &= \sqrt{\tilde{\hat{q}}_{\mathrm{vn}}(z)}\cdot\delta U_{\mathrm{sd}}(z) + \tfrac{1}{2}\delta\hat{q}_{\mathrm{vn}}(z)\cdot U_{\mathrm{sd}}(z)/\sqrt{\tilde{\hat{q}}_{\mathrm{vn}}(z)}
\end{aligned} \tag{55}$$

The following signal properties are used for the derivation of the gains in Eq. 52 from the expressions in Eq. 55:

- The tower speeds δv_{fa} and δv_{sd} are (almost) uncorrelated with the wave speed δw since the wind dominates the tower deformation; this implies:

$$\mathrm{E}[\delta w\cdot\delta v_{\mathrm{fa}}] \sim 0 \quad ; \quad \mathrm{E}[\delta w\cdot\delta v_{\mathrm{sd}}] \sim 0 \tag{56}$$

- The sign of δw, δv_{fa} and δv_{sd} is random to that of current $\bar{w}$; this implies:

$$\begin{aligned}
\mathrm{E}[\bar{w}\cdot\delta w] &= 0 \quad ; \quad \mathrm{E}[\bar{w}\cdot\delta v_{\mathrm{fa}}] = 0 \quad ; \quad \mathrm{E}[\bar{w}\cdot\delta v_{\mathrm{sd}}] = 0 \\
\mathrm{E}[\bar{w}+\delta w] &= \bar{w} \quad ; \quad \mathrm{E}[\bar{w}+\delta v_{\mathrm{fa}}] = \bar{w} \quad ; \quad \mathrm{E}[\bar{w}+\delta v_{\mathrm{sd}}] = \bar{w}
\end{aligned} \tag{57}$$

- Phase/space plots of $\{\delta v_{\mathrm{fa}}, \delta v_{\mathrm{sd}}\}$ usually show a rather wide ellipse, so that δv_{fa} and δv_{fa} are close to orthogonal because of 90^{o} phase shift and thus

$$\mathrm{E}[\delta v_{\mathrm{fa}}\cdot\delta v_{\mathrm{sd}}] \sim 0 \tag{58}$$

The first and second property imply that all (cross-variation-)product terms $\delta w\cdot v_{\mathrm{fa}}$, $\bar{w}\cdot v_{\mathrm{fa}}$ etc. vanish from Eq. 51 when it is used for the derivation of an expression for the effective, *intensity based* force size $\tilde{\hat{q}}_{\mathrm{vn}}$. Actually, only the squared terms are left and we decided to let the effective normalised force value be equal to the squared water current augmented with the sum of squared

[1] These second order terms contain 'powers of three' of variations of the form $(\delta(x_1)^2\cdot\delta(x_2)$; a belonging influence factor includes the expectation of the squared variation, which represents the intensity.

effective speed variation values:

$$\begin{aligned}\tilde{\hat{q}}_{\rm vn}(z) &= f(\bar{w}(z)^2 + \delta w(z)^2 + \delta v_{\rm fa}(z)^2 + \delta v_{\rm sd}(z)^2) \\ &= \bar{w}(z)^2 + \tilde{w}(z)^2 + \tilde{v}_{\rm fa}(z)^2 + \tilde{v}_{\rm sd}(z)^2\end{aligned} \tag{59}$$

The effective speed values are standard deviations multiplied with μ and $\frac{1}{2}\sqrt{8/\pi}$:

$$\begin{aligned}\tilde{w}(z) &= \mu(z) \cdot \tfrac{1}{2}\sqrt{8/\pi} \cdot \sigma_w(z) \\ \tilde{v}_{\rm fa}(z) &= \mu(z) \cdot \tfrac{1}{2}\sqrt{8/\pi} \cdot \sigma_{v_{\rm fa}}(z) \\ \tilde{v}_{\rm sd}(z) &= \mu(z) \cdot \tfrac{1}{2}\sqrt{8/\pi} \cdot \sigma_{v_{\rm sd}}(z)\end{aligned} \tag{60}$$

The multipliers μ and $\frac{1}{2}\sqrt{8/\pi}$ are included because of the applied optimized stochastic linearisation, which is dealt with after elaboration of the force variation expressions by Eq. 55.

When the first term of the Taylor series of $U_{\rm fa}$, $U{\rm sd}$ and $q_{\rm vn}$ is carried through in Eq. 55, the following expressions arise:

$$\begin{aligned}\delta q_{\rm fa,vn} &= \sqrt{\tilde{\hat{q}}_{\rm vn}(z)} \cdot \left(\frac{\partial U_{\rm fa}}{\partial w} \cdot \delta w(z) + \frac{\partial U_{\rm fa}}{\partial v_{\rm fa}} \cdot \delta v_{\rm fa}(z) + \frac{\partial U_{\rm fa}}{\partial v_{\rm sd}} \cdot \delta v_{\rm sd}(z) \right) + \\ &\quad \frac{{\rm c}_c \cdot \bar{w}(z) + {\rm c}_w \cdot \delta w(z) - \delta v_{\rm fa}(z)}{2\sqrt{\tilde{\hat{q}}_{\rm vn}(z)}} \cdot \left(\frac{\partial \hat{q}_{\rm vn}}{\partial w} \cdot \delta w(z) + \frac{\partial \hat{q}_{\rm vn}}{\partial v_{\rm fa}} \cdot \delta v_{\rm fa}(z) + \frac{\partial \hat{q}_{\rm vn}}{\partial v_{\rm sd}} \cdot \delta v_{\rm sd}(z) \right) \\ \delta q_{\rm sd,vn} &= \sqrt{\tilde{\hat{q}}_{\rm vn}(z)} \cdot \left(\frac{\partial U_{\rm sd}}{\partial w} \cdot \delta w(z) + \frac{\partial U_{\rm sd}}{\partial v_{\rm fa}} \cdot \delta v_{\rm fa}(z) + \frac{\partial U_{\rm sd}}{\partial v_{\rm sd}} \cdot \delta v_{\rm sd}(z) \right) + \\ &\quad \frac{{\rm s}_c \cdot \bar{w}(z) + {\rm s}_w \cdot \delta w(z) - \delta v_{\rm sd}(z)}{2\sqrt{\tilde{\hat{q}}_{\rm vn}(z)}} \cdot \left(\frac{\partial \hat{q}_{\rm vn}}{\partial w} \cdot \delta w(z) + \frac{\partial \hat{q}_{\rm vn}}{\partial v_{\rm fa}} \cdot \delta v_{\rm fa}(z) + \frac{\partial \hat{q}_{\rm vn}}{\partial v_{\rm sd}} \cdot \delta v_{\rm sd}(z) \right)\end{aligned} \tag{61}$$

The following partial derivatives hold:

$$\begin{aligned}\frac{\partial U_{\rm fa}}{\partial w} &= {\rm c}_w & & & \frac{\partial U_{\rm sd}}{\partial w} &= {\rm s}_w \\ \frac{\partial U_{\rm fa}}{\partial v_{\rm fa}} &= -1 & \text{and} & & \frac{\partial U_{\rm sd}}{\partial v_{\rm fa}} &= 0 \\ \frac{\partial U_{\rm fa}}{\partial v_{\rm sd}} &= 0 & & & \frac{\partial U_{\rm sd}}{\partial v_{\rm sd}} &= -1\end{aligned} \tag{62}$$

and

$$\begin{aligned}\frac{\partial \hat{q}_{\rm vn}}{\partial w} \cdot \delta w(z) &= 2{\rm c}_{cw}\bar{w}(z)\delta w(z) + 2\delta w(z)^2 - 2{\rm c}_w\delta v_{\rm fa}(z)\delta w(z) - 2{\rm s}_w\delta v_{\rm sd}(z)\delta w(z) \\ \frac{\partial \hat{q}_{\rm vn}}{\partial v_{\rm fa}} \cdot \delta v_{\rm fa}(z) &= -2{\rm c}_c\bar{w}(z)\delta v_{\rm fa}(z) + 2\delta v_{\rm fa}(z)^2 - 2{\rm c}_w\delta w(z)\delta v_{\rm fa}(z) \\ \frac{\partial \hat{q}_{\rm vn}}{\partial v_{\rm sd}} \cdot \delta v_{\rm sd}(z) &= -2{\rm s}_c\bar{w}(z)\delta v_{\rm sd}(z) + 2v_{\rm sd}(z)^2 - 2{\rm s}_w\delta w(z)\delta v_{\rm sd}(z)\end{aligned} \tag{63}$$

so that (dependency on (z) omitted):

$$\begin{aligned}\frac{\partial \hat{q}_{\rm vn}}{\partial w}\cdot\delta w + \frac{\partial \hat{q}_{\rm vn}}{\partial v_{\rm fa}}\cdot\delta v_{\rm fa} + \frac{\partial \hat{q}_{\rm vn}}{\partial v_{\rm sd}}\cdot\delta v_{\rm sd} \;=\; 2(\; &{\rm c}_{cw}\bar{w}\delta w - {\rm c}_c\bar{w}\delta v_{\rm fa} - {\rm s}_c\bar{w}\delta v_{\rm sd} \\ &+\delta w^2 + \delta v_{\rm fa}^2 + \delta v_{\rm sd}^2 - 2{\rm c}_w\delta w\delta v_{\rm fa} - 2{\rm s}_w\delta w\delta v_{\rm sd}\;)\end{aligned} \tag{64}$$

It is clear that the 4$^{\rm th}$, 5$^{\rm th}$ and 6$^{\rm th}$ terms in the right hand sides of Eq. 61 contain expressions in variation δ as power-of-one, power-of-two and power-of-three (δ^1-, $delta^2$-, δ^3-expressions). These latter three terms have to be reduced to only δ^1-expressions in order to arrive at contributions to the pursued gains in Eq. 52.

The δ^2-expressions can principally not be maintained: δ^2-squares cause skew, essential non-linear affections to the force variations; δ^2-cross-products cause no contribution as by properties 56 and 58. So, the δ^2-expressions have to be neglected in the sequel. The δ^3-expressions can be reduced to δ^1-expressions if they include a δ^2-factor for which an effective, intensity based value can be assumed. Properties 59 and 60 tell that typical non-zero values of the cross products $\delta w\delta v_{\rm fa}$, $\delta w\delta v_{\rm sd}$ and $\delta v_{\rm fa}\delta v_{\rm sd}$ do *not* exist. Hence, only δ^3-expressions that include a squared variation are to be maintained. This concerns the terms with the factors δw^3, $\delta w^2\cdot\delta v_{\rm fa}$, $\delta w^2\cdot\delta v_{\rm sd}$, $\delta v_{\rm fa}^3$, $\delta v_{\rm fa}^2\delta w$, $\delta v_{\rm fa}^2\delta v_{\rm sd}$, $\delta v_{\rm fa}^2\delta v_{\rm sd}$, $\delta v_{\rm sd}^3$, $\delta v_{\rm sd}^2\delta w$ and $\delta v_{\rm sd}^2\delta v_{\rm fa}$.

When we only maintain the δ^1- and relevant δ^3-expressions in the 4$^{\rm th}$ to 6$^{\rm th}$ terms of Eq. 61 and replace squared variations $\delta(.)^2$ by squared effective values $\tilde{(.)}^2$, the numerators of these terms evolve to the following expressions (dependency on (z) omitted):

$$\begin{aligned}&\tfrac{1}{2}({\rm c}_c\bar{w} + {\rm c}_w\delta w - \delta v_{\rm fa})\cdot(\;\tfrac{\partial \hat{q}_{\rm vn}}{\partial w}\cdot\delta w + \tfrac{\partial \hat{q}_{\rm vn}}{\partial v_{\rm fa}}\cdot\delta v_{\rm fa} + \tfrac{\partial \hat{q}_{\rm vn}}{\partial v_{\rm sd}}\cdot\delta v_{\rm sd}\;)\;\;\mapsto \\ &\qquad({\rm c}_c{\rm c}_{cw}\bar{w}^2 + {\rm c}_w\tilde{w}^2 + 3{\rm c}_w\tilde{v}_{\rm fa}^2 + {\rm c}_w\tilde{v}_{\rm sd}^2)\cdot\delta w - ({\rm c}_c{\rm s}_c\bar{w}^2 + 2{\rm s}_w{\rm c}_w\tilde{w}^2)\cdot\delta v_{\rm sd} \\ &\qquad\qquad -({\rm c}_c{}^2\bar{w} + 2{\rm c}_w{}^2\tilde{w}^2 + \tilde{w}^2 + \tilde{v}_{\rm fa}^2 + \tilde{v}_{\rm sd}^2)\cdot\delta v_{\rm fa} \\ &\tfrac{1}{2}({\rm s}_c\bar{w} + {\rm s}_w\delta w - \delta v_{\rm sd})\cdot(\;\tfrac{\partial \hat{q}_{\rm vn}}{\partial w}\cdot\delta w + \tfrac{\partial \hat{q}_{\rm vn}}{\partial v_{\rm fa}}\cdot\delta v_{\rm fa} + \tfrac{\partial \hat{q}_{\rm vn}}{\partial v_{\rm sd}}\cdot\delta v_{\rm sd}\;)\;\;\mapsto \\ &\qquad({\rm s}_c{\rm c}_{cw}\bar{w}^2 + {\rm s}_w\tilde{w}^2 + {\rm s}_w\tilde{v}_{\rm fa}^2 + 3{\rm s}_w\tilde{v}_{\rm sd}^2)\cdot\delta w - ({\rm s}_c{\rm c}_c\bar{w}^2 + 2{\rm s}_w{\rm c}_w\tilde{w}^2)\cdot\delta v_{\rm fa} \\ &\qquad\qquad -({\rm s}_c{}^2\bar{w}^2 + 2{\rm s}_w{}^2\tilde{w}^2 + \tilde{w}^2 + \tilde{v}_{\rm fa}^2 + \tilde{v}_{\rm sd}^2)\cdot\delta v_{\rm sd}\end{aligned} \tag{65}$$

When the above evolvations and the results of Eq. 62 are carried through in Eq. 61, then appropriate expressions are obtained for the derivation of the gains in Eq. 52.

$$\begin{aligned}\delta q_{\rm fa,vn} \;=\;& \sqrt{\tilde{\hat{q}}_{\rm vn}(z)}\cdot(\;{\rm c}_w\delta w(z) - \delta v_{\rm fa}(z)\;) + \\ &\frac{1}{\sqrt{\tilde{\hat{q}}_{\rm vn}(z)}}\cdot[\;({\rm c}_c{\rm c}_{cw}\bar{w}^2 + {\rm c}_w\tilde{w}^2 + 3{\rm c}_w\tilde{v}_{\rm fa}^2 + {\rm c}_w\tilde{v}_{\rm sd}^2)\cdot\delta w - ({\rm c}_c{\rm s}_c\bar{w}^2 + 2{\rm s}_w{\rm c}_w\tilde{w}^2)\cdot\delta v_{\rm sd} \\ &\qquad -({\rm c}_c{}^2\bar{w} + 2{\rm c}_w{}^2\tilde{w}^2 + \tilde{w}^2 + \tilde{v}_{\rm fa}^2 + \tilde{v}_{\rm sd}^2)\cdot\delta v_{\rm fa}\;] \\ \delta q_{\rm sd,vn} \;=\;& \sqrt{\tilde{\hat{q}}_{\rm vn}(z)}\cdot(\;{\rm s}_w\delta w(z) - \delta v_{\rm sd}(z)\;) + \\ &\frac{1}{\sqrt{\tilde{\hat{q}}_{\rm vn}(z)}}\cdot[\;({\rm s}_c{\rm c}_{cw}\bar{w}^2 + {\rm s}_w\tilde{w}^2 + {\rm s}_w\tilde{v}_{\rm fa}^2 + 3{\rm s}_w\tilde{v}_{\rm sd}^2)\cdot\delta w - ({\rm s}_c{\rm c}_c\bar{w}^2 + 2{\rm s}_w{\rm c}_w\tilde{w}^2)\cdot\delta v_{\rm fa} \\ &\qquad -({\rm s}_c{}^2\bar{w}^2 + 2{\rm s}_w{}^2\tilde{w}^2 + \tilde{w}^2 + \tilde{v}_{\rm fa}^2 + \tilde{v}_{\rm sd}^2)\cdot\delta v_{\rm sd}\;]\end{aligned} \tag{66}$$

The expressions for the desired height dependent gains follow in a straightforward way:

$$\begin{aligned} K_{\mathrm{fw}}(z) &= \mathrm{c}_w\sqrt{\tilde{\hat{q}}_{\mathrm{vn}(z)}} + (\mathrm{c}_c\mathrm{c}_{cw}\bar{w}_{(z)}{}^2 + \mathrm{c}_w\tilde{w}_{(z)}{}^2 + 3\mathrm{c}_w\tilde{v}_{\mathrm{fa}(z)}{}^2 + \mathrm{c}_w\tilde{v}_{\mathrm{sd}(z)}{}^2)/\sqrt{\tilde{\hat{q}}_{\mathrm{vn}(z)}} \\ K_{\mathrm{ff}}(z) &= -\sqrt{\tilde{\hat{q}}_{\mathrm{vn}(z)}} - (\mathrm{c}_c{}^2\bar{w} + 2\mathrm{c}_w{}^2\tilde{w}_{(z)}{}^2 + \tilde{w}_{(z)}{}^2 + \tilde{v}_{\mathrm{fa}(z)}{}^2 + \tilde{v}_{\mathrm{sd}(z)}{}^2)/\sqrt{\tilde{\hat{q}}_{\mathrm{vn}(z)}} \\ K_{\mathrm{fs}}(z) &= -(\mathrm{c}_c\mathrm{s}_c\bar{w}_{(z)}{}^2 + 2\mathrm{s}_w\mathrm{c}_w\tilde{w}_{(z)}{}^2)/\sqrt{\tilde{\hat{q}}_{\mathrm{vn}(z)}} \end{aligned} \tag{67}$$

and

$$\begin{aligned} K_{\mathrm{sw}}(z) &= \sqrt{\tilde{\hat{q}}_{\mathrm{vn}(z)}}\cdot(\mathrm{s}_w) + (\mathrm{s}_c\mathrm{c}_{cw}\bar{w}_{(z)}{}^2 + \mathrm{s}_w\tilde{w}_{(z)}{}^2 + \mathrm{s}_w\tilde{v}_{\mathrm{fa}(z)}{}^2 + 3\mathrm{s}_w\tilde{v}_{\mathrm{sd}(z)}{}^2)/\sqrt{\tilde{\hat{q}}_{\mathrm{vn}(z)}} \\ K_{\mathrm{sf}}(z) &= -(\mathrm{s}_c\mathrm{c}_c\bar{w}_{(z)}{}^2 + 2\mathrm{s}_w\mathrm{c}_w\tilde{w}_{(z)}{}^2)/\sqrt{\tilde{\hat{q}}_{\mathrm{vn}(z)}} \\ K_{\mathrm{ss}}(z) &= -\sqrt{\tilde{\hat{q}}_{\mathrm{vn}(z)}} - (\mathrm{s}_c{}^2\bar{w}_{(z)}{}^2 + 2\mathrm{s}_w{}^2\tilde{w}_{(z)}{}^2 + \tilde{w}_{(z)}{}^2 + \tilde{v}_{\mathrm{fa}(z)}{}^2 + \tilde{v}_{\mathrm{sd}(z)}{}^2)/\sqrt{\tilde{\hat{q}}_{\mathrm{vn}(z)}} \end{aligned} \tag{68}$$

B Transformation of blade properties

This section describes the transformation of blade properties from ECN BLADMODE input data based on detailed LM data (in the blade coordinate system) to TURBU/PHATAS (element coordinate system). TURBU allows for different elastic, aerodynamic, center of gravity and shear center axis offset definition. The bending stiffness must be given in the element coordinate system, with origin in the elastic center and crosssection axes that coincide with the elastic neutral orientation. Therefore we chose to define all input data in the element coordinate system, as is the case in PHATAS. The input is primarily derived from (more extensive) BLADMODE input and original LM data, but compared to PHATAS input for consistency check.

The following input differences between PHATAS and TURBU must be considered. As mentioned in chapter 2 on modelling, all the axis in PHATAS are defined on the chord. Whereas in PHATAS the elastic axis and the blade axis coincide, in TURBU (and BLADMODE) this elastic axis must be defined in both flap- and leadwise direction. Prebend (in both directions) can also be added using this elastic offset. In PHATAS, prebend is defined as a curvature and added separately. This result in a slight difference in prebend specification.Further, TURBU allows for seperate values for aerodynamic twist (chordline) and structural twist (elastic neutral axis).

The transformation of properties from the blade coordinate system to twist oriented is done as follows (Gere and Timoshenko (1999))

$$EI_{flat} = \frac{(EI_{lead} + EI_{flap})}{2} - \left(\frac{(EI_{lead} - EI_{flap})}{2} \cdot \cos(2\alpha_{struc}) + EI_{cross} \cdot \sin(2\alpha_{struc}) \right) \tag{69}$$

$$\tan(2\theta) = \frac{-2EI_{cross}}{(EI_{flap} - EI_{lead})} \tag{70}$$

$$\begin{bmatrix} \epsilon \\ \eta \end{bmatrix} = \begin{bmatrix} \cos(\alpha) & \sin(\alpha) \\ -\sin(\alpha) & \cos(\alpha) \end{bmatrix} \cdot \begin{bmatrix} x \\ y \end{bmatrix} \tag{71}$$

C Blade torsion modelling difference

The torsion moment (and deformation) calculated with TURBU showed a considerable difference compared to PHATAS (figure 41). The torsion moment and resulting deformation was a factor ten larger, which seemed to come from a fundamental modelling difference. Looking at the separate contributions to blade torsion the difference was finally uncovered.

The blade root torsion moment consists of three components.

1 the aerodynamic moment due to the offset of the aerodynamic center with respect to the blade axis
(+ when offset is to the leading edge)

2 the moment as consequence of flap deformation and lead force
(- when flap is +)

3 the moment as a result of lead deformation and flap force
(+ when lead is +)

When the blade pitches, the effects become even more complex. Figure 40 shows the separate effects, and the aggregate result. From this analysis, the difference was found in the reversed definition of the aerodynamic moment coefficient C_M. Instead of cancelling the aerodynamic moment, this effectively doubled the torsion moment on the blade, resulting in different aeroelastic behavior. Finally this issue was solved by correcting the sign of the aerodynamic moment coefficient C_M in the TURBU input handling (file `rotorpar.m`). Now comparable results are obtained, as shown in figure 41 and 12.

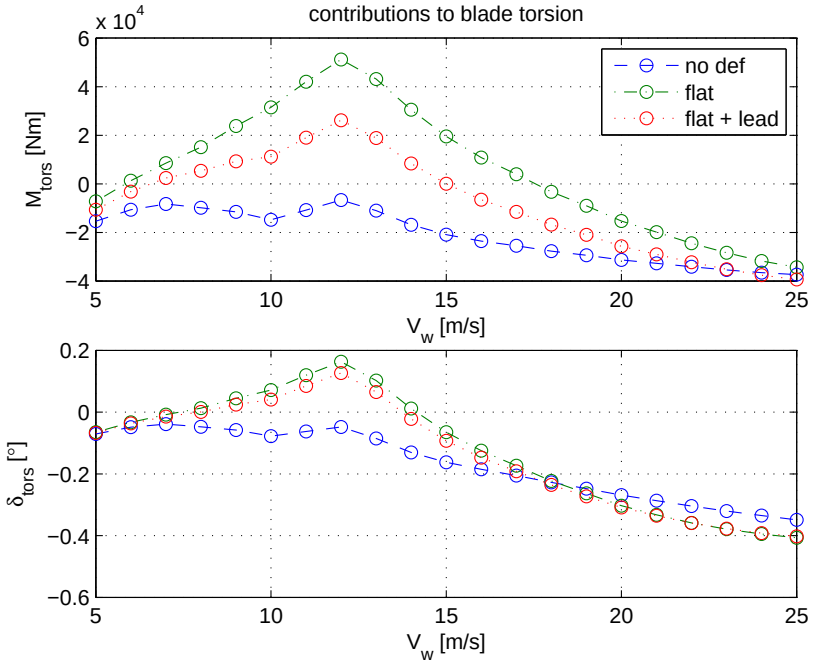

Figure 40: Contributions to blade torsion of aerodynamic moment, flap and lead wise deformation for different wind speeds across the operating range.

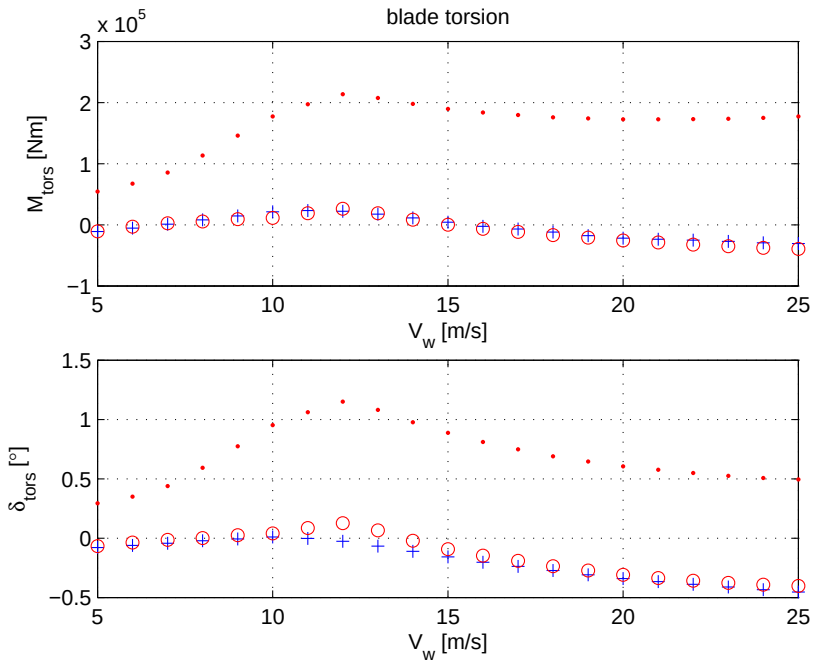

Figure 41: Equilibrium blade torsion calculated with PHATAS (bx) and TURBU (ro) and TURBU with reversed C_M (r.) for different wind speeds across the operating range.

D Sea state measurements at IJmuiden offshore site YM6

The sea conditions at the IJmuiden offshore site YM6 have been monitored for more than twenty years now. This campaign was set up to get better understanding of the North sea and create an extensive database for offshore development. The measurements are publicly available on RWS (2009). The wind and wave data are recorded as 3 hours average. The measurements used in this project are wind speed V_{wind} and direction ϕ_{wind}, mean wave height H_m, period T_m and direction ϕ_{wave}. PHATAS (ROWS) and TURBU use the significant wave height H_s and peak period T_p to define the sea state. For a fully developed sea with JONSWAP peak factor $\gamma_{js} = 3.3$, the following relations hold:

$$\begin{aligned} H_s &= H_m \\ T_p &= 1.286 \cdot T_m \end{aligned} \tag{72}$$

This research uses the data from 1979 to 2001, which makes up more then twenty years of the wind turbine lifetime. This twenty year is the current design and certification lifetime, but for offshore wind turbines this is could change in the future (longer lifetime is favourable due to relatively high installation cost). To reduce the amount of points, the data is grouped in bins. Wind speed is sorted in 1m/s bins, the direction of wind and waves is divided in twelve sections (of thirty degrees). The wave height and period are grouped in 0.5m and 0.5s bins. The effect of water current loading is not considered in this project, because no measurement data is available on current and direction. Figure 43 shows the wind speed distribution (Weibull; shape 2, mean 10) and figure 42 shows the dominant wind and wave direction (SW).

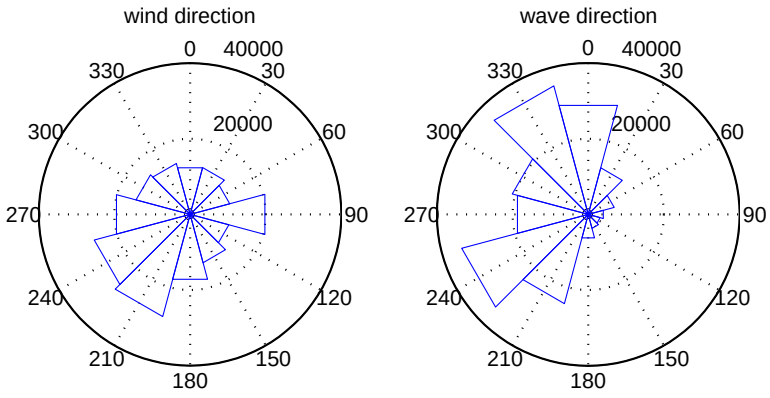

Figure 42: Wind and wave direction at IJmuiden. The dominant direction is South-West for both wind and waves.

Sea state data is usually represented in a scatter diagram, showing the number of occurrences of each combination of wave height and period in a certain time span. Such a 3D scatter of the used data is shown in figure 44.

When wind and wave direction are also included, we speak of 4D (angle between wind and waves), or even 5D (direction of both) sea state scatter. This last set is important for fatigue analysis on the support structure, which does not rotate along with the wind (loading).

Another subset of the whole dataset is defined as the most occurring sea states for each wind speed, where direction between wind and waves is zero degrees. This dataset is used to compare PHATAS and TURBU results in section 2.4.

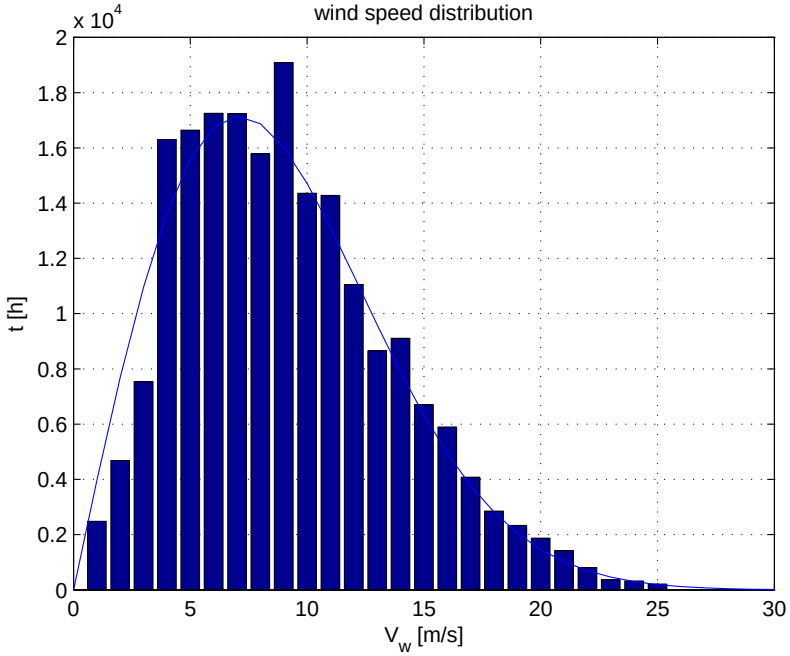

Figure 43: Wind speed distribution at IJmuiden. The wind speed distribution follows a Weibull pattern.

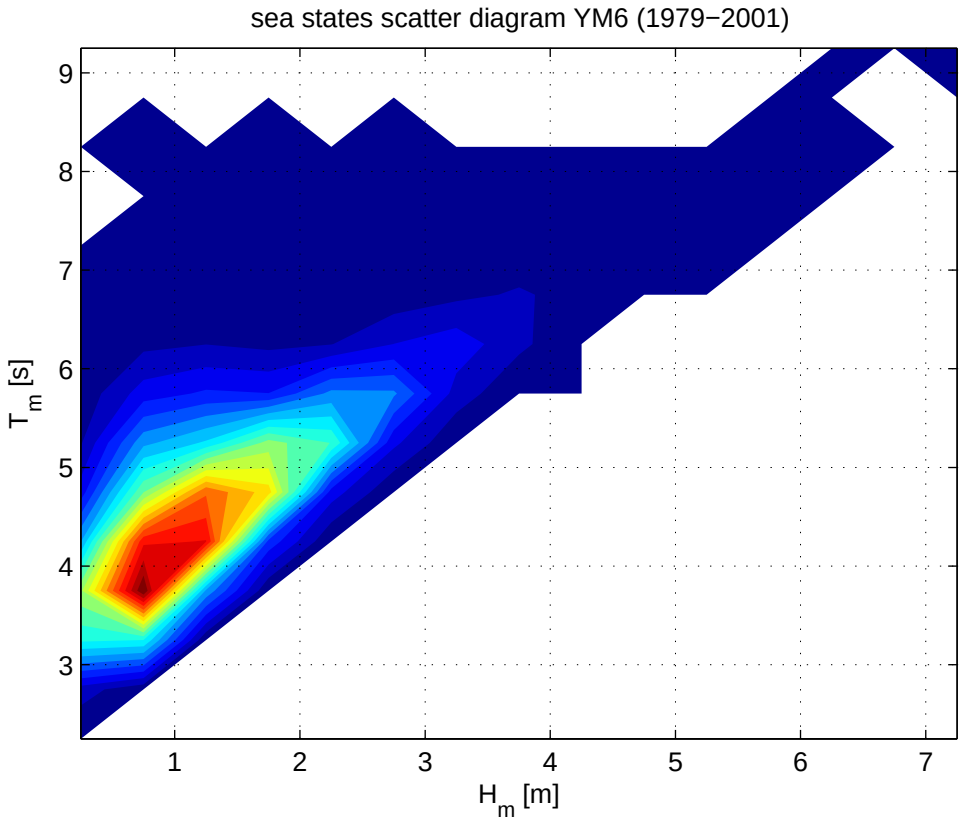

Figure 44: Number of occurrences (colored; b:low - r:high) of each combination of wave height and period.

E Optimization strategy for TURBU load set calculation

Although TURBU is a very fast tool, the following strategy (section E.3) is used to speed up the calculation of the full 5D scatter diagram. This involves both clever arrangement of the load set, as some special features of the program itself.

E.1 Load set arrangement

Rearranging the load set can speed up the process as described below.

1 sort on wind speed
Wind speed defines the working point of the wind turbine model. Changing the wind speed thus requires a new model to be computed. The load set should be sorted for wind speed to minimize these recalculations.

2 rotate for wind direction
Different wind direction also requires a model update. For a symmetric support structure (like a monopile) wind direction only has influence on the support structure loading (which does not rotate along with the wind). The number of load cases can easily be reduced by reusing the simulation result at a specific wind speed and direction for all other wind directions with equal sea state (H_s, T_p and $\phi_{w\&w}$) and performing the rotation of the loading by hand. The support structure fatigue in the fixed base coordinate system is determined from the resulting time series.

The transformation of the tower base moments from wind to foundation coordinate system over wind direction angle ϕ_{wind} is shown in (73).

$$\begin{bmatrix} M_{fa} \\ M_{sts} \\ M_{tors} \end{bmatrix} = \begin{bmatrix} \cos(\phi_{wind}) & -\sin(\phi_{wind}) & 0 \\ \sin(\phi_{wind}) & \cos(\phi_{wind}) & 0 \\ 0 & 0 & 1 \end{bmatrix} \cdot \begin{bmatrix} tlS_2 \\ tlS_1 \\ tlS_3 \end{bmatrix} \tag{73}$$

3 wave direction
In theory, wave direction has no impact on the equilibrium state, but it does have impact on the model (through input transformation matrices). A change in wave direction therefore requires a new model to be generated and the load set should be sorted for this variation.

E.2 TURBU for 'LOAD' application

TURBU can be used in different modes, which provide specific features. In this research the application 'LOAD' is used. The following steps are performed to speed up the calculation.
- calculate (equilibrium) working points beforehand
- output selection to reduce the data handling to a minimum
- reuse model and load excitation whenever possible

E.3 Strategy

This results in the following strategy:

1 load sea state scatter

2 calculate working points (V_{wind}, Ω, θ, η)
```
for loop = 1:N_oc;
```

3 define load set jobfile with working point and variation data

4 calculate time series

5 search for load cases with same sea state, but different wind direction
```
index = find(H_s == H_s(loop) & T_p == T_p(loop) & WWd == WWd(loop));
for subloop = index;
```

6 transfer time series for wind direction

7 calculate eq1Hz fatigue load
```
end; %subloop
end; %loop
```